Graduate School Form 30
Updated 1/15/2015

PURDUE UNIVERSITY
GRADUATE SCHOOL
Thesis/Dissertation Acceptance

This is to certify that the thesis/dissertation prepared

By Md Nazmuzzaman Khan

Entitled

THREE-DIMENSIONAL TRANSIENT NUMERICAL STUDY OF HOT-JET IGNITION OF METHANE-HYDROGEN BLENDS IN A CONSTANT-VOLUME COMBUSTOR

For the degree of Master of Science in Mechanical Engineering

Is approved by the final examining committee:

M Razi Nalim
Chair

Whitney Yu

Likun Zhu

To the best of my knowledge and as understood by the student in the Thesis/Dissertation Agreement, Publication Delay, and Certification Disclaimer (Graduate School Form 32), this thesis/dissertation adheres to the provisions of Purdue University's "Policy of Integrity in Research" and the use of copyright material.

Approved by Major Professor(s): M Razi Nalim

Approved by: Sohel Anwar 7/2/2015

Head of the Departmental Graduate Program Date

THREE-DIMENSIONAL TRANSIENT NUMERICAL STUDY OF HOT-JET IGNITION OF METHANE-HYDROGEN BLENDS IN A CONSTANT-VOLUME COMBUSTOR

A Thesis

Submitted to the Faculty

of

Purdue University

by

Md Nazmuzzaman Khan

In Partial Fulfillment of the

Requirements for the Degree

of

Master of Science in Mechanical Engineering

August 2015

Purdue University

Indianapolis, Indiana

To God, my family and my friends.

ACKNOWLEDGMENTS

Firstly I would like to express my gratitude to my advisor, Dr. Razi Nalim, for all the support and guidance throughout my Master's degree. His unprecedented knowledge in numerical turbulent combustion guided me to achieve my research goals. I would also like to thank Dr. Whitney Yu and Dr. Likun Zhu for their time. Dr. Yu's Turbulence class was the best one I had during this program. Appreciation and thanks is also given to Ms. Valerie Lim Diemer and Ms. Vitanemi Sara for their help to prepare this thesis.

I am grateful to my wife, Suchana, for loving me and tolerating all the troubles that I have created during the past two years. I am also grateful to my mother for always supporting me and making the silent sacrifices from the background. I have also enjoyed my time in CPRL with my friends and lab-mates Yup, Arash, Moh and Ali. A special thanks goes to David Briel for all the Linux and Windows related help. I also want to thank the people from CONVERGE and EnSight who helped me a lot to setup my simulation cases and post-process.

The work was partially supported by the National Science Foundation, under grant NSF/CBET-1235696, and by a graduate student fellowship award from Indiana University - Purdue University Indianapolis. Financial and computational support from the Purdue School of Engineering and Technology at IUPUI is also acknowledged.

TABLE OF CONTENTS

Page

LIST OF TABLES

LIST OF FIGURES

Figure Page

Figure Page

Figure Page

Figure Page

Figure Page

ABBREVIATIONS

HRR	Heat release rate
CVC	Constant volume combustor
SFI	Shock flame interaction
AMR	Adaptive mesh refinement
RANS	Reynolds-averaged Navier-Stokes
LES	Large eddy simulation
DNS	Direct numerical simulation

ABSTRACT

Khan, Md Nazmuzzaman. M.S.M.E., Purdue University, August 2015. Three-Dimensional Transient Numerical Study of Hot-Jet Ignition of Methane-Hydrogen Blends In A Constant-Volume Combustor. Major Professor: M. Razi Nalim.

Ignition by a jet of hot combustion product gas injected into a premixed combustible mixture from a separate pre-chamber is a complex phenomenon with jet penetration, vortex generation, flame and shock propagation and interaction. It has been considered a useful approach for lean, low-NO_x combustion for automotive engines, pulsed detonation engines and wave rotor combustors. The hot-jet ignition constant-volume combustor (CVC) rig established at the Combustion and Propulsion Research Laboratory (CPRL) of the Purdue School of Engineering and Technology at Indiana University-Purdue University Indianapolis (IUPUI) is considered for numerical study. The CVC chamber contains stoichiometric methane-hydrogen blends, with pre-chamber being operated with slightly rich blends. Five operating and design parameters were investigated with respect to their effects on ignition timing. Different pre-chamber pressure (2, 4 and 6 bar), CVC chamber fuel blends (Fuel-A: 30% methane + 70% hydrogen and Fuel-B: 50% methane + 50% hydrogen by volume), active radicals in pre-chamber combusted products (H, OH, O and NO), CVC chamber temperature (298 K and 514 K) and pre-chamber traverse speed (0.983 m/s, 4.917 m/s and 13.112 m/s) are considered which span a range of fluid-dynamic mixing and chemical time scales. Ignition delay of the fuel-air mixture in the CVC chamber is investigated using a detailed mechanism with 21 species and 84 elementary reactions (DRM19). To speed up the kinetic process adaptive mesh refinement (AMR) based on velocity and temperature and multi-zone reaction technique is used.

With 3D numerical simulations, the present work explains the effects of pre-chamber pressure, CVC chamber initial temperature and jet traverse speed on ignition for a specific set of fuels. An innovative post processing technique is developed to predict and understand the characteristics of ignition in 3D space and time.

With the increase of pre-chamber pressure, ignition delay decreases for Fuel-A which is the relatively more reactive fuel blend. For Fuel-B which is relatively less reactive fuel blend, ignition occurs only for 2 bar pre-chamber pressure for centered stationary jet. Inclusion of active radicals in pre-chamber combusted product decreases the ignition delay when compared with only the stable species in pre-chamber combusted product. The effects of shock-flame interaction on heat release rate is observed by studying flame surface area and vorticity changes. In general, shock-flame interaction increases heat release rate by increasing mixing (increase the amount of deposited vorticity on flame surface) and flame stretching. The heat release rate is found to be maximum just after fast-slow interaction.

For Fuel-A, increasing jet traverse speed decreases the ignition delay for relatively higher pre-chamber pressures (6 and 4 bar). Only 6 bar pre-chamber pressure is considered for Fuel-B with three different pre-chamber traverse speeds. Fuel-B fails to ignite within the simulation time for all the traverse speeds.

Higher initial CVC temperature (514 K) decreases the ignition delay for both fuels when compared with relatively lower initial CVC temperature (300 K). For initial temperature of 514 K, the ignition of Fuel-B is successful for all the pre-chamber pressures with lowest ignition delay observed for the intermediate 4 bar pre-chamber pressure. Fuel-A has the lowest ignition delay for 6 bar pre-chamber pressure.

A specific range of pre-chamber combusted products mass fraction, CVC chamber fuel mass fraction and temperature are found at ignition point for Fuel-A which were liable for ignition initiation. The behavior of less reactive Fuel-B appears to me more complex at room temperature initial condition. No simple conclusions could be made about the range of pre-chamber and CVC chamber mass fractions at ignition point.

1. INTRODUCTION

1.1 Background

Increasingly worldwide interest and regulations related to fuel economy and greenhouse gas emissions have led the combustion research to develop new engines, combustors, and systems with greater thermal efficiency with minimal NO_x emission. This is possible with lean and ultra-lean combustion systems but the major limitation is the poor ignition quality of the mixture. This initiates the necessity of high energy ignition system, such as pre-chamber hot jet ignition system. Hot-jet is usually created by partial combustion of slightly rich fuel-air mixture in a separate pre-chamber with a spark or glow plug. Highly energized "torch jet" from the pre-chamber is transferred to the combustion chamber through an orifice or orifices. Chemically active radicals and fast turbulent mixing in hot jets create an explosion that is more energetic than a spark [1], allowing more rapid ignition. The presence of reactive species in the jet also aids the chemical kinetics of fuel combustion [2].

Hot jet ignition is a very complex process of turbulent mixing of burnt and unburnt gas coupled with chemical kinetics. It becomes more complex at supersonic jet flow where temperature, pressure and mach number have significant influences on ignition process. Hot jet ignition focused on safety perspective was experimentally studied by Sadanandan et al. [3].They observed that, ignition started near the jet tip; not at the lateral side for a H_2-air mixture. But that may not be an universal feature and may vary with the temperature of the hot-jet and cold air-fuel mixture. Earlier works of Meyer et al. [4] and Philips [5] shows the effects of mixing and chemistry on ignition initiation by hot jet. Larsen and Eckhoff [6] studied the critical nozzle diameter of flame transmission from the view of explosion protection for propane-air mixture. In recent years Bunce et al. [7] from MAHLE powertrain have examined the effect

of nozzle diameter on turbulent jet ignition (TJI) to increase the thermal efficiency. TJI is different than torch jet ignition. In TJI system, flame from the pre-chamber is purposefully quenched by limiting the orifice diameter. They found out that too small nozzle diameter create choked flow which places a limit on energy density and creates fewer ignition spots. On the other hand, too large nozzle diameter introduces substantial amount of flame from pre-chamber combustion. From the study they concluded that, continuous unchoked flow with maximum flame quenching should be the condition of optimum nozzle diameter.

As a potential technology for increased thermal efficiency and reduced NOx, hot jet ignition has been implemented in lean burn SI combustion engines [1,8–10], pulsed detonation engines [11, 12] and wave rotor constant volume combustors (WRCVC) [13].A WRCVC consists of an array of channels arranged around a rotating circular drum (Figure 1.1). Each channel is an individual constant volume combustor (CVC). Premixed air-fuel mixture enters the CVC through the inlet port, ignition usually starts with a mounted igniter or combusted gas from previous cycle [14].

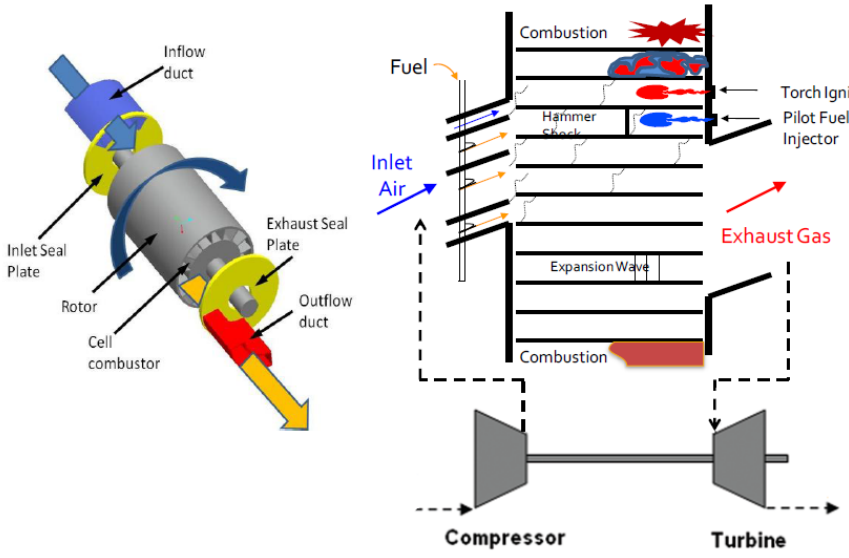

Figure 1.1. Schematic configuration of WRCVC and view of a typical cycle [14].

Combustion occurs at nearly constant volume which increases the pressure in CVC. After combustion exhaust gases are expunged through the exit port at a higher pressure which may go to a turbine. The Humphrey thermodynamic cycle is the theoretical operating cycle for constant volume combustion, which consists of upstream compressed gas and downstream expansion to another device. Figure 1.2 shows the thermodynamic difference of Humphrey cycle and Brayton cycle (gas turbine thermodynamic cycle) in a T-s diagram. Assuming air standard cycle and constant specific heat ratio of 1.33, Akbari and Nalim [13] compared the entropy generation of the two cycles and showed about 25% entropy reduction for Humphrey cycle. Pressure gain and entropy reduction which create greater turbine power and cycle efficiency for fixed energy input is the advantage of constant volume combustion over constant pressure combustion.

The Combustion and Propulsion Research Lab (CPRL) at IUPUI has been conducting research in pressure gain constant volume combustor over a decade. Pekkan and Nalim [15] developed a multi-dimensional leakage model for wave rotor combustor using a quasi-one-dimensional code. This code was originally developed for non-steady flow in wave rotors [16, 17]. Later the code has been modified to model combustion, opening time, energy losses, and mass addition at any location [18]. Nalim and Pekkan [19] numerically studied the thermal NO_x production in a constant volume combustor for propane by using a commercially available turbulent combustion code with 2D flow. They found that cases with low fuel/air ratios like conventional engines have lower emission indices compared to higher fuel/air ratio cases. They also showed that engines with 100 ppm goal can be realized. Akbari et al. [20] numerically studied the performance enhancement of a hydrogen-fueled wave rotor combustor by using the quasi-one-dimensional code. They found that with two different detonative combustion configurations which are substantially different in fuel distribution and ignition geometries, significant pressure gain can be achieved for both configurations. Khalid et al. [21] numerically studied the factors affecting the fuel distribution and did not include combustion with a 2D geometry. They stated

several challenges in obtaining the desired fuel distribution. Akbari and Nalim [22] numerically investigated the effects of instantaneous detonation and deflagration to detonation transition (DDT) in wave rotor combustor. The outflow of the DDT is found to be more uniform than instantaneous detonation and more acceptable for turbine blades. They also proposed appropriate locations of fuel injectors and the ignition initiator for backward combustion propagation of DDT [23]. The effect of rotation on overall fuel consumption is studied numerically with 2D geometry and it has been found that shock waves and gas motions has stronger impact on flame dynamics that buoyancy force [24]. Wijeyakulasuriya and Nalim [25] studied jet behavior and the mixing characteristics with 2D geometry with different jet injector orientation and pressure. They observed important flow dynamics such as, the generation of two counter-rotating vortices in traverse direction who controls the fuel-air mixing. Wijeyakulasuriya et al. [26] also studied the mixing behavior of hot inert gas injected into long combustion chambers with 2D compuations. They found that ignition delay is dependent on the momentum of the injected hot mass. They also suggested a qualitative method to determine the ignition locations. Excellent reviews of pressure gain combustion of wave rotor combustor published from CPRL group are also available in literature. [13, 27].

The hot jet ignition constant volume combustor (CVC) rig at IUPUI consists of two separate parts, a pre-chamber with attached nozzle and a long rectangular constant volume combustion chamber with square cross section. The pre-chamber can be stationary or rotated. Ignition starts in the CVC chamber when hot combusted jet burst through the nozzle into the main chamber. An aluminum diaphragm is placed between the nozzle and pre-chamber to build up the pressure in pre-chamber which is common in shock tube type experiments. To visualize the ignition process and the shock-flame interaction in a constant volume combustor, a high speed camera and a Z-type schlieren system are available which are showed in Figure 1.3. High-speed compressible transient jet from pre-chamber creates shock in a constant volume combustor which leads to vortex generation, shock flame interaction, flame front

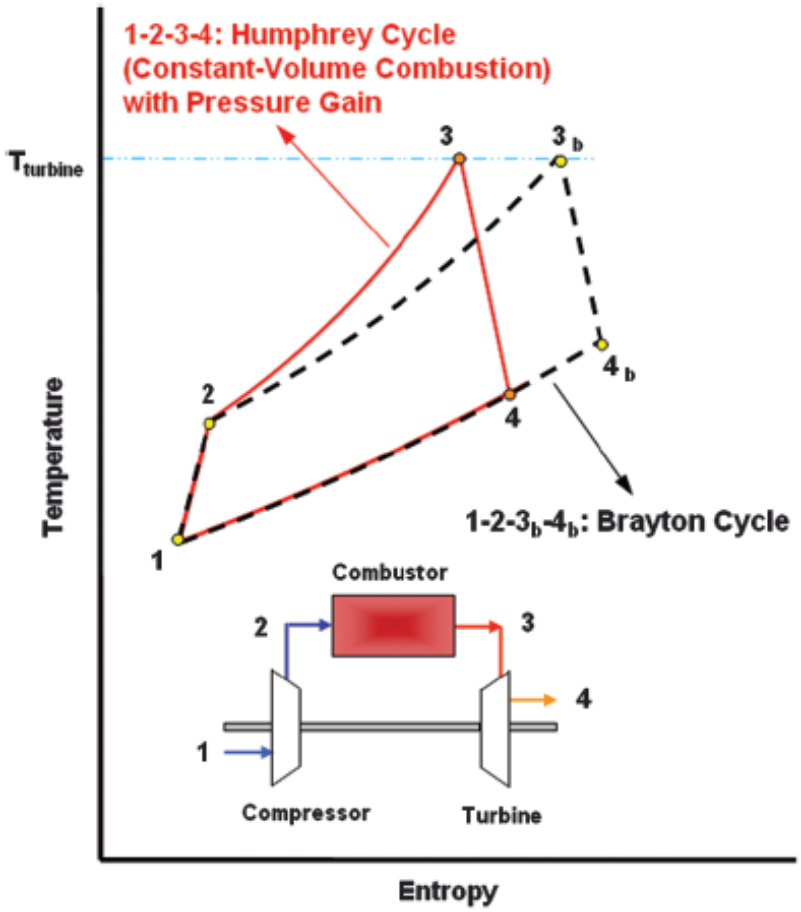

Figure 1.2. Superior performance of the Humphrey cycle (1-2-3-4) over the Brayton cycle (1-2-3b-4b) [13].

deformation type complex behaviors, which are common in wave rotor type combustor [28–30]. In addition, reflecting shock and expansion waves generated due to confined geometry also affect the ignition.

At University of Washington, a similar CVC rig was built and tested by Bilgin [31]. Similar to IUPUI rig, a separate pre-chamber was used by Bilgin to supply hot jet into the CVC chamber. He studied hot jet ignition for stationary jet and translating jet with varying equivalence ratio, jet area, jet position, traverse velocity and pre-chamber pressure. He used Damkoehler number to explain the ignition phenomena in CVC chamber. At IUPUI, Baronia [32] tried to numerically simulate Bilgin's work for

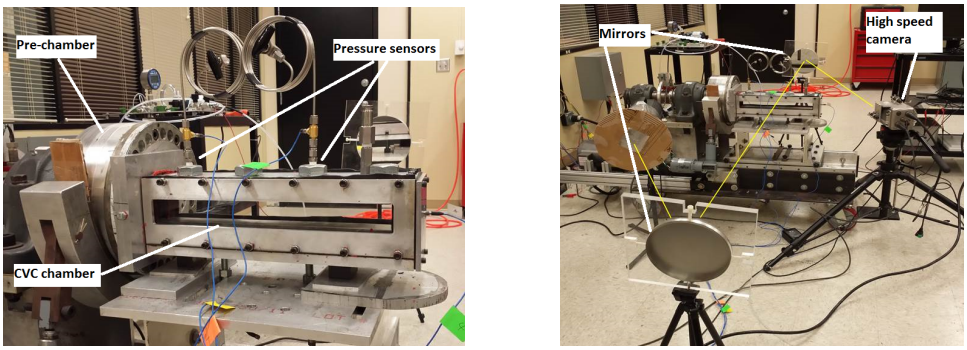

(a) Experimental rig (b) Z-type schlieren system

Figure 1.3. Experimental rig with Z-type schlieren system at IUPUI.

centered stationary jet using a temperature based hybrid four step combustion model to understand the supersonic jet mixing, turbulent flame propagation and shock flame interaction. Perera [33] experimentally studied the same test rig to gain insight about suitable fuels for wave rotor application with three different fuels- methane, propane and ethylene. By varying the equivalence ratio in pre-chamber and CVC chamber he measured the ignition delay for centered stationary jet. Methane showed the highest ignition delay and ethylene showed the lowest ignition delay. When ethylene was used as a pre-chamber fuel with equivalence ratio 1.1, ignition delay was lowest for all the tested fuels for a 5 mm diameter converging nozzle.

Karimi et al. [34] developed a 2D model of the modified hot jet CVC rig [35] to study the chemical kinetics and effects of different combustion models of the hot jet ignition process for stationary and translating jets using a commercial CFD code. In this study, turbulence was modeled by a two equation RANS model and combustion was modeled using hybrid eddy-breakup model which used finite rate chemistry. Prasanna [36] experimentally continued Perera's work with further modification for translating jets and methane-hydrogen (60% CH_4-40% H_2 by volume) mixture fuels. It is to be noted that, hydrogen addition with methane decreased the ignition delay up until 6.1 ms traverse time. When the traverse time decreased below 6.1 ms (means increased pre-chamber speed), ignition delay was increased.

Due to higher ignition energy than conventional spark ignition engine and several other advantages, hot jet ignition applications in IC engines have a long history. Pre-chamber application in engine can be divided into two fundamental categories [8]: no auxiliary pre-chamber fueling and auxiliary pre-chamber fueling. Auxiliary pre-chamber fueling can be sub-divided into two more categories: pre-chamber volume over 3% of combustion chamber volume (large pre-chamber) and pre-chamber volume below 3% of combustion chamber volume (small pre-chamber). Both designs have their own advantages and disadvantages and studied by several companies during last 70 years. The Lavinnai Aktyvatsia Gorenia (LAG) or avalanche-activated combustion was developed by Gussak, which came from the studies conducted by N.N. Semenov at around 1950 [37]. Gussak's extensive research first revealed the importance of active radicals in hot jet ignition. Honda successfully developed an engine with pre-chamber named CVCC (Compound Vortex Controlled combustion) [38, 39], which was not a completely jet ignition system. In CVCC engine the flame emerged from the pre-chamber without any quenching, where in conventional jet ignition flame is quenched inside of the nozzle and hot jet is inserted into the combustion chamber. But CVCC engine was successful in obtaining the emission standards in 1975 without any after-treatment. Ford [40], Volkswagen [41], Porsche SKS [42], GM Electronic Fuel Injection (EFI) torch ignition [43] all studied and implemented different technologies of jet ignition to extend the lean operating range of the engine around 1975. In recent times, Turbulent jet ignition system of MAHLE powertrain [1,7]and ongoing research in Melbourne University on jet ignition are also noteworthy. An excellent review of the evolution and application of jet ignition system in combustion can be found in literature by Toulsen et al. [8].

Addition of hydrogen with methane has major advantages. It increases the performance of the fuel, increases operation range and decreases hydrocarbon emission. As a result it is considered as an alternative fuel in power generation for both gas turbine [44–46] and engine [47–49] application. The effects of hydrogen addition to methane on burning velocity have been extensively studied both experimentally

and numerically for different equivalence ratios and fuel compositions [50–53]. Laminar burning velocity increases linearly with addition of hydrogen up until the mole fraction is about 0.7. The effect is less for lean mixtures. For engine application, Sierens and Rosseel [48] showed that hydrogen has very limited effect on efficiency and emission when the mole fraction is up to 0.2. But, starting from 0.2, high efficiency and low emission was found when methane was replaced by hydrogen. Yiguang and Takashi [54] numerically studied the ignition of hydrogen-methane blends in supersonic mixing layer. They found that hydrogen is an effective ignition initiator for methane because hydrogen produces H and O radicals. They also realized that, ignition enhancement is proportional to hydrogen addition. From direct numerical simulation, Hawkes et al. [51] found that hydrogen addition makes more stable, resistant to extinction flame than pure methane flame by increasing the burning rate per unit area. In more recent studies Wang et al. [55] showed that, hydrogen addition with methane can potentially reduce aldehyde emissions and soot formation. Moreover, chemical kinetics of hydrogen has little effect on NO formation from methane combustion. Hot-jet ignition is more complex than conventional laminar burning velocity studies. Hot jet ignition in CVC for methane-hydrogen blend is studied at IUPUI both experimentally and numerically and very recently at Purdue University experimentally [56].

Detailed 3D, transient, compressible, turbulent, chemically reactive flow problems for real geometries still cannot be solved numerically due to various length scales of turbulence. If greater computational power was available, turbulent combustion could be simulated directly by using Direct Numerical Simulation (DNS) to solve Navier Stokes (NS) and energy equations. DNS solve turbulence to the smallest length scales, which is Kolmogorov length scale. Turbulence enhances mixing significantly and is defined by its different length scales. If it was possible to achieve the resolution of Kolmogorov length scales, no model for combustion (ex. Eddy Breakup Model) or turbulence (ex. RANS or LES) would be needed. Unfortunately, even with the current supercomputing power available it is not reasonable for most of the engine and

combustor simulations. With Reynolds Average Navier Stokes (RANS) simulation it is possible to run combustion simulations for real geometries. The main advantage of RANS is that it solves only the large scales of turbulence as a result mesh sizes can be significantly larger than DNS because DNS has to solve the smallest scales.

SAGE detailed chemistry solver [57] is an effective way to calculate reaction rates from a reaction mechanism and eventually model combustion. SAGE reads in CHEMKIN formatted reaction mechanism [58] and at the beginning of each time step calculates reaction rates at each cell based on temperature, pressure and species mass fraction. If no additional model for turbulent chemistry interaction is not added, this type of model is relatively faster. Well stirred reactor model is often used to describe this SAGE type of model. With a well resolved computational domain, the effects of mixing is accounted for in the RANS turbulence model [59]. However, mixing will not be accurately predicted if the mesh resolution does not resolve the details of the flow at least down to the integral scale of turbulence. More important, in many regimes of combustion, the scale of wrinkled laminar flames will not be resolved. This implies that turbulence-chemistry interaction modeling is important, and there are many approaches available with different computational cost. It is acknowledged that the absence of turbulence-chemistry interaction (TCI) modeling is a possible weakness of the current model. Several models are developed to resolve TCI. The Magnussen model [60], the Direct Quadrature Moment Method (DQMOM) [61], the Assumed PDF [62], the Lagrangian PDF [63] and the Linear Eddy Model [64] are available in literature. For one-step reaction schemes, Norris [65] developed a simple algebraic equation which can be used to capture TCI more accurately by using Magnussen type simple TCI model. Karimi [66] studied the chemical activity and reaction pathways of hot jet ignition with a 2D model considering turbulence chemistry interaction. The main issue with 2D model is not turbulence, which is still modeled. The problem is with the difference in the large scale flow and vortex structures which can not be captured properly. Moreover, according to Karimi, to run 3D simulations of the igni-

tion rig present at IUPUI, it would take almost one month with a relatively reduced reaction mechanism when considering turbulence chemistry interaction.

1.2 Scope of the Present Research

The objective of present research is to understand the effects of pre-chamber pressure, CVC chamber initial temperature and jet traverse speed on ignition and also to explore the underlying reasons that initiates ignition in pre-chamber jet ignition constant volume combustor. The current work is continued from numerical studies and results established by Karimi [66] on 2D simulation of hot jet ignition in CVC which were further modified and adapted for detailed 3D simulation study. Turbulence is modeled using two equation RANS model and combustion is modeled assuming every cell as well stirred reactor with SAGE detailed chemical reaction rate calculation. Quantitative data about hot jet ignition in a CVC is gathered for methane-hydrogen fuel blends. Several design parameters (pre-chamber pressure, CVC chamber temperature and jet traverse speed) are considered for detail 3D simulation and their effects on ignition is studied. Innovative post processing is used to analyze ignition behavior as a function of pre-chamber species mass fraction, CVC chamber species mass fraction and temperature in 3D space and time. Ignition point is marked from temperature contour plot for a specific case. The same case is simulated with combustion model turned off. Mass fraction and temperature is plotted at ignition point for combustion model turned off case to find out their values at ignition delay time. For a specific fuel underlying conditions behind ignition is also identified. Detailed 3D model development and simulation for CVC and ignition behavior analysis in three-dimensional space and time are the major contributions of this study. Some of the conclusions of the present study can be used to design pre-chamber jet ignition type practical combustion device.

1.3 Chapter Contents

The introduction and scope of the present thesis is described in Chapter 1. Chapter 2 presents a discussion on experimental setup and computational methods employed in the present study. Chemical ignition delay variation with temperature for different methane-hydrogen fuel blends is also discussed in this chapter. The detailed description and comparison of different combustion models and reaction mechanisms are described in Chapter 3. The effects of active radicals inclusion in pre-chamber combusted products is investigated in Chapter 4. In Chapter 5, a detailed study of ignition and combustion for two different methane-hydrogen fuel blends is carried out. Different pre-chamber pressure, CVC chamber initial temperature and jet traverse speed effects on ignition are studied in this chapter. Effects on flame propagation, flame surface deformation and vorticity generation on combustion are also explained. Also a method to identify the underlying reasons for ignition initiation for a specific fuel is developed and explained in this chapter. The conclusions and the recommendations of the present research are described in the last chapter.

2. CASE SETUP AND NUMERICAL METHODOLOGY

2.1 Experimental Setup

At the University of Washington, Bilgin [31] built a hot- jet ignition CVC rig with financial support from National Aeronautics and Space Administration (NASA) Lewis Research Center. This rig was later installed and studied at Combustion and Propulsion Research Lab (CPRL), Indiana University Purdue University Indianapolis (IUPUI). The rig used in current study was completely redesigned and rebuilt by Murphy [35] adding several important modifications. This new rig is capable of producing higher traverse speed and visualization capabilities at the jet entrance into of the CVC chamber [36].

The cylindrical pre-chamber of the test rig is used for producing combusted product which is precisely injected in to the CVC chamber through a nozzle attached to the pre-chamber. By optional rotation of the pre-chamber it is possible to create a either stationary or traversing jet. The pre-chamber internal cavity is of cylindrical design, 166 mm (6.52 inches) in diameter and width 39.1 mm (1.54 inches), forming an internal volume of approximately $8.4\times10^4 m^3$ (51 cubic inches). The constant volume combustor (Figure 2.1) used in ignition experiments has a main CVC chamber with square cross-section of side 39.9 mm (1.57 inches) and is 406 mm (16.0 inches) long. Optically accessible windows are available on both side of the CVC chamber and pressure transducers are installed on the top wall. The exit diameter of the converging nozzle that connects the pre-chamber with the CVC chamber is 5.99 mm (0.236 inches). Modifications are made on the bottom plate to install a heater to pre-heat the CVC chamber air-fuel mixture. An aluminum diaphragm is placed between the pre-chamber and nozzle. Pressure increases in the pre-chamber because of

combustion, resulting the rupture of the diaphragm at a certain pressure. Then the combusted hot jet is injected into the CVC chamber.

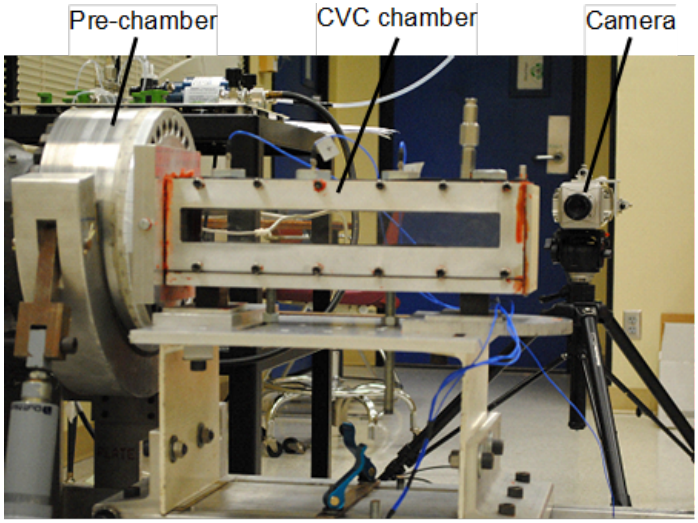

Figure 2.1. Constant-volume combustor traversing jet ignition rig.

2.2 Numerical Methodology for 2D and 3D Models

To study the effects of active radicals a two-dimensional (2D) model (Figure 2.2) of the combustor is used to simulate the transient, turbulent, reacting and compressible flow. The height, length and nozzle diameter is same as ignition rig. This approach preserve the height ratio of the confined jet. The volume ratio of pre-chamber to CVC chamber is also preserved, although small nozzle volume is neglected. "This allows the same non-dimensional volume flow rate between the experiment and 2D numerical calculations, preserving mass and energy realism and the nominal pressure history" [67]. Direct comparison with experiments is not intended for 2D model.

For the rest of the study, a detailed 3D model (Figure 2.3) of the test rig, that includes the spark plug and the bolts in the pre-chamber, is considered for simulation. From experimental study, it is concluded that the clearance gap between nozzle and CVC chamber plays vital role in later part of the combustion process, as the leakage

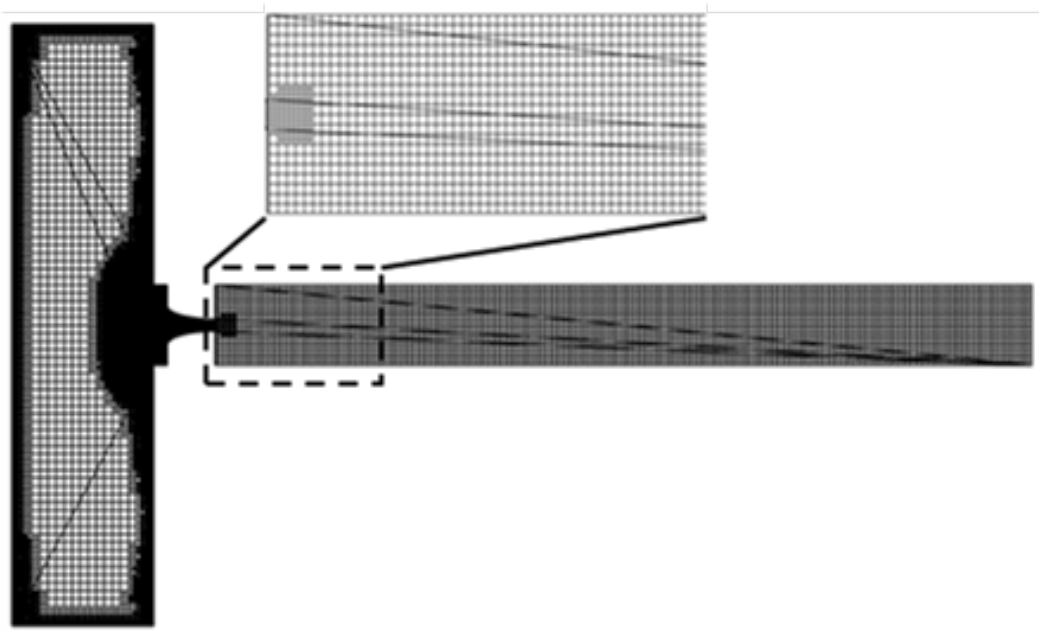

Figure 2.2. 2D Computational domain and initial mesh at the start of simulation.

tends to gradually decrease the CVC chamber pressure. For the centered stationary jet, clearance gap is negligible and has minimal effect on CVC chamber pressure. For the traversing jet, clearance gap reaches to a maximum of about 0.03 seconds and then remains around 0.5 mm for rest of the time. The maximum physical time reached during this numerical study is up to 4.0 ms (0.004 seconds). It is also observed from the experimental study that virtually no leak gap prevails upto 10.0 ms. For this reason also for detailed 3D simulations no leak gap is considered. Although all the simulations are run in 3D; for better visualization and understanding, a 2D plane is considered through the center of the nozzle (Figure 2.4) to show important variables in post-processing throughout this study.

The computational fluid dynamics (CFD) code CONVERGE [57] is used in this analysis, mainly for its automatic mesh refinement (AMR) and multi-zoning capabilities. It is a finite-volume CFD code capable of handling complex geometries with moving boundaries, modeling turbulence, transient liquid sprays, and chemical-reaction. In this study a second-order accurate spatial discretization scheme and a fully implicit

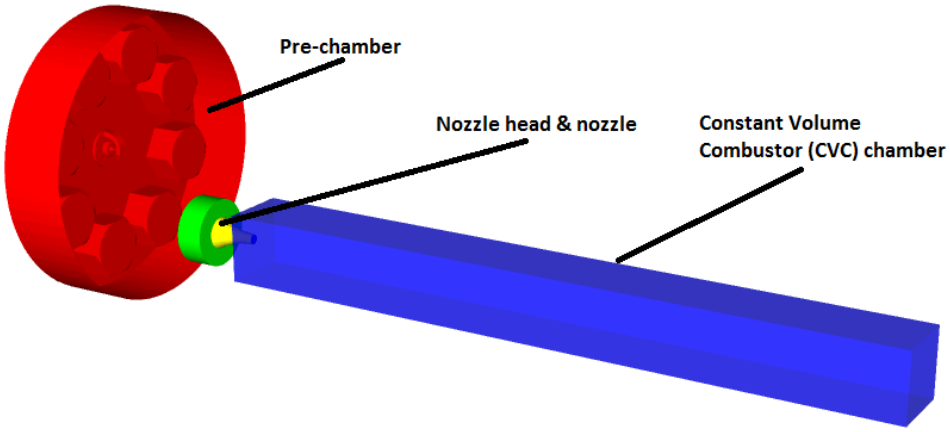

Figure 2.3. 3D computational domain considered for centered stationary and traversing jet.

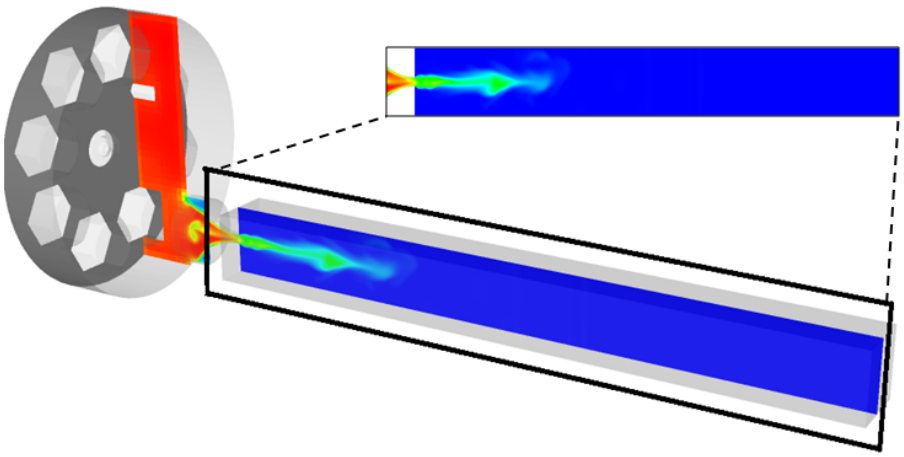

Figure 2.4. 2D plane considered in post-processing for 3D simulations.

first-order accurate time-integration scheme are used to solve the governing conservation equations. The transport equations are solved using the pressure implicit with splitting of operators (PISO) method of Issa [68]. The time-step is automatically maximized for stability in each computational cycle, based on flow velocity and local speed of sound.

The 2D computations are run on two dedicated 12-processor Intel Xeon E5645 machines (2.4 GHz processors, 24 effective processors and 48 GB RAM). For 3D computations, IU supercomputer Big Red 2 is used. Big Red 2 is a Cray XE6/XK7 supercomputer with a hybrid architecture providing a total of 1,020 compute nodes.

The number of processors used in this analysis is limited by the number of commercial licenses available. During the first half of this thesis, 24 'child' licenses and 3 'parent' licenses were available. During the second half, CONVERGE provided unlimited child licenses and 4 parent licenses. Each processor run utilizes one child license. A script file which has details on the number of processors the analysis would be run on, estimated time required for the analysis, execution commands of the software, and some other control commands; has to be submitted into the queuing system of the supercomputing cluster-Big Red 2. The job scheduler assigns the requested amount of processors and computing time, based on server availability. The script file iupui.sh contains the commands as listed in Appendix A.

Depending on the number of processors assigned to run a job, CONVERGE divides the simulation domain into several ranks. Rank is the number of processors assigned to run the job. A certain number of cells is solved by each rank and to run CONVERGE efficiently, uniform distribution of the cells among the ranks are required. When the amount of cells available at a region goes below a certain number, total number of cells assigned to a rank goes to zero, CONVERGE automatically redistribute the cells to other ranks. As a result, when excess numbers of processors are assigned to run a certain job, it may take longer time or even stop, due to the fact that the number of ranks with zero cell increases and cell distribution among the ranks is not uniform. So, for efficient run time, assigning optimum amount of processors to a certain job is required. From the personal experience of the author, it is suggested that using 16 processors for 2D model and 64 processors for 3D model is convenient.

2.3 Adaptive Mesh Refinement (AMR) and Multi-zone Reaction Modeling

Adaptive Mesh Refinement (AMR) automatically refines the grid based on fluctuating and moving conditions, such as temperature and velocity [69]. This option is useful for using a highly refined grid to accurately simulate complex phenomena such as flame propagation, high-velocity flow or shock wave interaction without unnecessarily slow down the simulation with a globally refined grid. AMR algorithm adds higher grid resolution (embedding) where the flow field is most under-resolved or where the gradient of a specified field variable is the highest [69]. In the current simulation temperature and velocity AMR is used to refine the mesh at each time step. The largest and smallest grid size used in the simulation is 4.0 mm and 0.125 mm respectively. This provides adequate resolution for turbulent flame fronts and reasonably sharp representation for shock waves to model shock wave interactions. Every cell is assumed to be a well stirred reactor, as a result reaction rate is based on detailed chemical kinetic model. The maximum cell count reaches around 10 million for 3D simulations. If the entire computational domain was to be refined to the smallest (0.125 mm) cell size without any AMR or fixed embedding, the total cell count would be 70 million, which shows the importance of AMR. Figure 2.5 shows the typical cell counts in 2D and 3D simulations. Local mesh refinement used throughout this study for high velocity flow and turbulent flame using AMR is showed in Figure 2.6.

At each discrete time, each computational cell is at a distinct thermodynamic state. CONVERGE groups the computational cells with similar pressure, temperature and equivalence ratio into separate zones, with pre-specified ranges of the mentioned variables. The zone averaged values of species concentration, temperature and pressure are used to calculate the reaction rates once at that zone. As reaction rates are calculated by zones rather than individual cells, this process speeds up the run time considerably. The zonal values of temperature, pressure and species concentra-

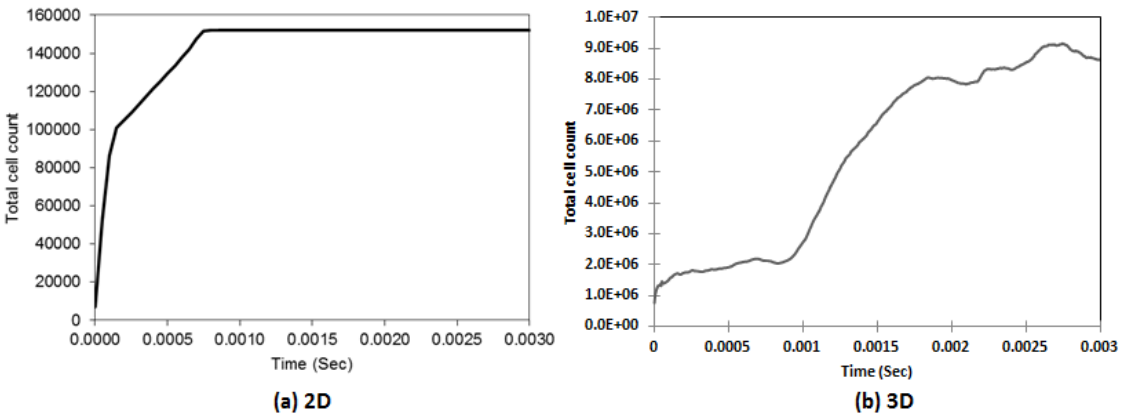

Figure 2.5. Total cell count variation for a typical (a) 2D and (b) 3D case with time.

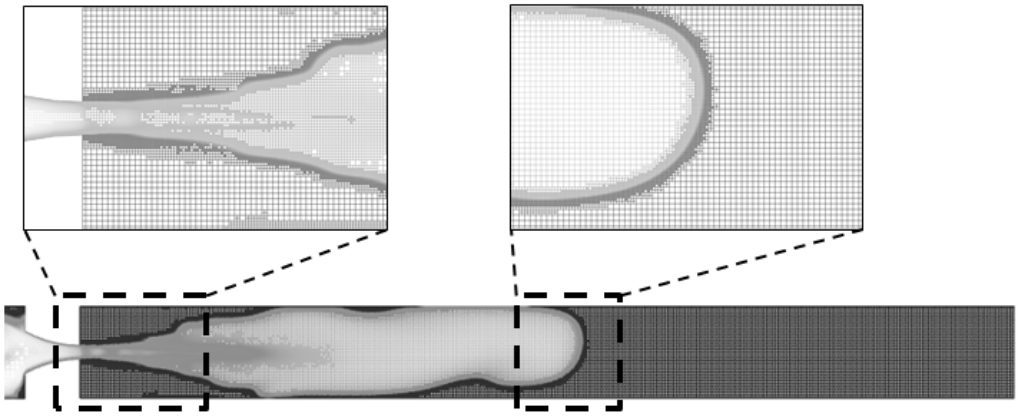

Figure 2.6. Local mesh refinement for high velocity flow and turbulent flame using AMR.

tion are then remapped onto individual cells to calculate reaction rate for next time step. Multi-zone modeling was first introduced by Aceves et al. [70]. CONVERGE uses similar technique outlined by Babajimopoulos et al. [71] with some differences. Cell temperature, equivalence ratio and fuel species mass fraction are used throughout the study as multi-zone binning parameters.

2.4 Chemical Ignition Delay

The ignition delay in a jet ignited CVC is defined as the time interval from the start of pre-chamber hot jet flow into CVC to the start of combustion. This delay period consists of physical delay, where mixing of relatively cold air fuel with hot jet occurs and chemical delay attributed to pre-combustion reactions of hot jet and fuel air species. The physical mixing process is complex. Detailed 3D CFD calculations are required to predict ignition. Purely chemical delay depends on temperature, pressure and species mass or mole fractions. To calculate chemical ignition delay for a specific fuel, a large reaction mechanism (containing a set of stiff equations in CHEMKIN format) developed for that fuel has to be solved. A open source chemistry package named Cantera [72] is used throughout this study to set up the CHEMKIN formatted equations for solving. Cantera is a function library with object-oriented features that can be use in C++, Fortran, MatLab, and Python applications. The distinctive feature of Cantera is the open structure that allows researchers to help each other improve kinetic mechanisms and data for combustion calculation. Cantera can be used for chemical equilibrium, chemical kinetic, reactor network, 1D flame, reaction path diagram and stirred reactor calculations by providing reaction mechanism in CHEMKIN format. To calculate the chemical ignition delay, the reaction mechanism, pressure, temperature and species mole or mass fraction are used as input parameters. Temperature profile or other species profiles can be studied to determine chemical ignition delay. The typical Cantera code used in Matlab to calculate chemical ignition delay contains the commands listed in Appendix B.

In the wave rotor constant volume combustor, the pre-chamber combusted hot jet bursts through the nozzle into CVC chamber, mixes with the relatively quiescent fuel-air mixture and starts the ignition process. Ignition depends on the temperature, fraction of hot jet and fuel present at ignition point and chemical reactivity of fuel. If the fuel is chemically less reactive, like methane, it will take relatively longer amount of time to ignite compared to more reactive fuel like hydrogen. Therefore, it is useful

to examine the chemical ignition delay time of a spatially uniform mixture before investigating the interaction of mixing and chemical processes. The chemical ignition delay can provide valuable information about how much time the fuel and hot jet mixture needs to ignite chemically. The characteristic chemical time scale can be varied over a wide range by the use of mixture of hydrogen and methane in various proportions. This mimics the behavior of any single fuel over a wide temperature range. Different fuel mixtures of methane-hydrogen starting from 100% methane to 20%, 40%, 60%, 80% and 100% of hydrogen by volume are considered. Three different equivalence ratio 0.6, 0.8 and 1.0 are used. The ignition delay time of each fuel-air mixture is computed for a spatially uniform mixture. GRI Mech 3.0 [73], a well-known optimized reaction mechanism with 53 species and 325 reactions is used for this calculation. Initial pressure is 1 atmosphere for all the cases.

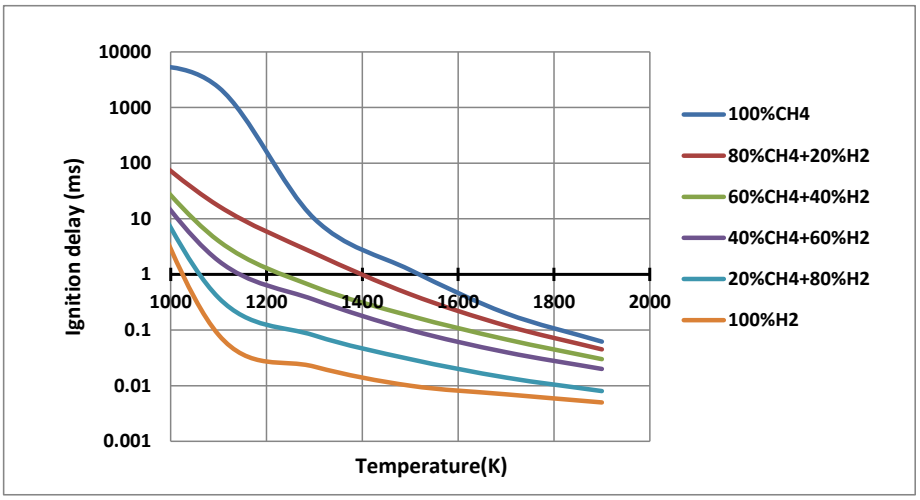

Figure 2.7. Chemical ignition delay with temperature for methane-hydrogen fuel blends with equivalence ratio 1.0

The variation of ignition delay with temperature is plotted in Figures 2.7-2.9. As expected, with the increase of temperature, ignition delay decreases for all the cases while pressure is kept constant. Pure methane has the highest ignition delay, of approximately 8 seconds for $\phi = 1.0$ at 1000 K. For the other two cases with leaner mixtures (Figure 2.8 and 2.9), the solution did not converge and Cantera is unable

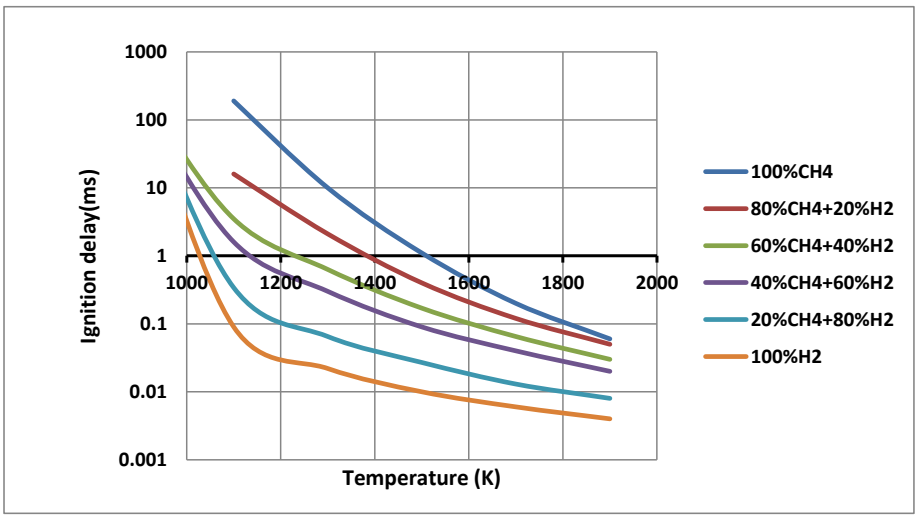

Figure 2.8. Chemical ignition delay with temperature for methane-hydrogen fuel blends with equivalence ratio 0.8

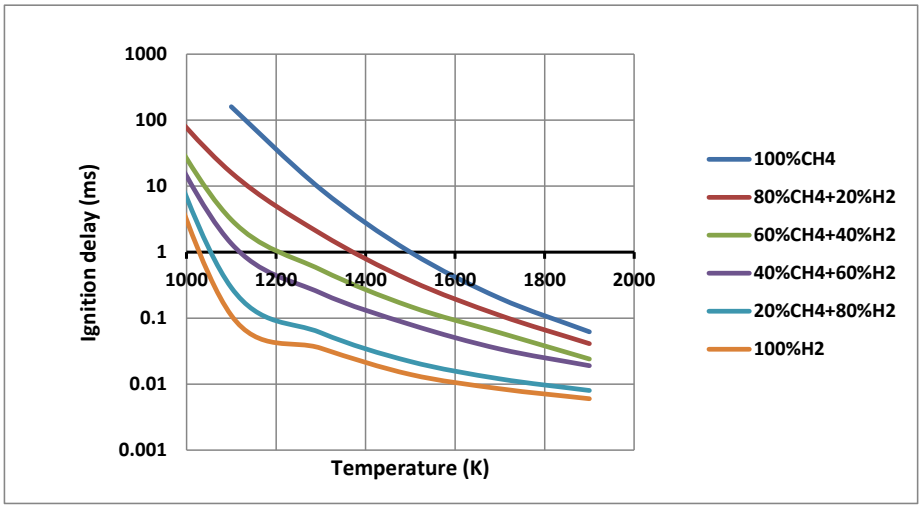

Figure 2.9. Chemical ignition delay with temperature for methane-hydrogen fuel blends with equivalence ratio 0.6

to compute the the very large ignition delay at below 1000 K for pure methane. Analyzing the Figures from 2.7 through 2.9, it is evident that equivalence ratio has a relatively weak effect on ignition delay. From stoichiometric ($\phi = 1.0$) to very lean mixture ($\phi = 0.6$), the ignition delay time and trend is comparable for the same

fuel blends at different temperature. Replacing methane with hydrogen decreases the ignition delay dramatically, especially with lower initial temperature. From 1000 K to 1200 K ignition delay decreases rapidly for all the cases but for higher temperatures, the drop in ignition delay is not as dramatic. Pure hydrogen has the most rapid drop of ignition delay. For stoichiometric mixtures at 1000 K, the blend with a small amount of hydrogen and mostly has nearly the same time delay as pure hydrogen, where pure methane is much less reactive. For high temperature, there is a more gradual variation in blend fuel ignition delay from pure methane to pure hydrogen.

To understand how the pre-chamber hot gas affects the chemical ignition delay, two mixtures are considered that contains both pre-chamber hot exhaust gas and CVC chamber fuel. One mixture contains 33% of combusted products of pre-chamber hot gas and 67% of CVC chamber fuel (by volume); the other one contains 50% of both hot exhaust gas and fuel. This study of the role on active radicals and the amount of exhaust products is conducted with only methane as the fuel. The exhaust gas re-injected consists of products of combustion of a rich methane-air mixture of equivalence ratio 1.1. The combusted products of pre-chamber hot gas contained active radicals like H, OH, O and NO. For each mixture, two cases are considered: one contains active radicals from hot gas and the other with no active radicals so that the mixture contains stable species only. Chemical ignition delay with temperature for both cases is plotted in Figure 2.10 where, HG stands for hot gas and AR means active radicals.

Chemical ignition delay decreases with increasing temperature for all the cases. Active radicals have significant effect on chemical ignition delay. Both 33% hot gas (HG) and 50% hot gas without active radicals cases have almost identical ignition delay for different temperatures. This means that if HG contains only stable species, increased amount of HG in unburned air-fuel mixture has minimal effect on ignition delay. For both 33% and 50% hot gas cases, active radicals decrease the ignition delay by a factor of about three compared to cases without radicals. The 50% hot gas case has slightly lower ignition delay compared to the 33% hot gas case because 50% hot

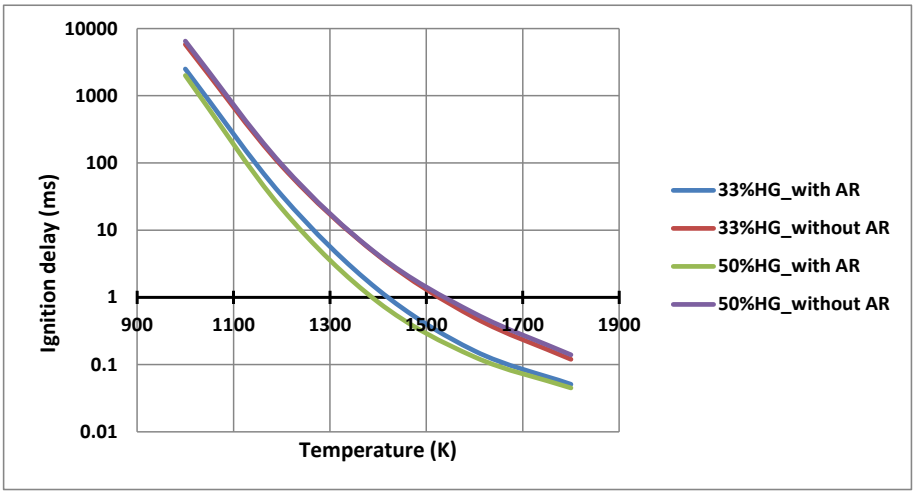

Figure 2.10. Chemical ignition delay with temperature for different hot gas-fuel mixture with and without active radicals.

gas contains slightly higher amount of active radicals. The rate at which the chemical ignition delay reduced with temperature was same for all the cases.

3. TURBULENT COMBUSTION MODELING

3.1 Introduction

Turbulent combustion is a common phenomenon in most of the practical combustion systems such as rockets, internal combustion engines, industrial burners and furnaces. Numerical combustion has been used widely to predict this complex phenomenon and validate it with experiments. But numerical simulations of turbulent reacting flows still remain challenging according to Poinsot [74]:

1)Even without turbulence, combustion is a complex process with a large range of chemical time and length scales. Some controlling phenomena of combustion take place within a very short time over thin layers and are also associated with large gradients of mass fractions, temperature and density. A complete description of the chemical kinetics inside a laminar flame may include hundreds of species and thousands of reactions, which will lead to considerable numerical difficulties and errors.

2)The difficulties to find the exact solutions of Navier-Stokes equation which will predict turbulence are well known. As various length and time scales are involved, numerical solution of the structure of turbulence are still hard to predict. British physicist, Sir Horace Lamb, described the uncertainties with his trite remark, "I am an old man now, and when I die and go to heaven there are two matters on which I hope for enlightenment. One is quantum electrodynamics, and the other is the turbulent motion of fluids. And about the former I am rather optimistic." [75]

3)Turbulent combustion involves two-way interaction between chemistry and turbulence. A flame front releases heat and change kinematic viscosity related to temperature. When a flame interacts with a turbulent flow, this mechanism may generate turbulence or damp it. On the other hand, turbulence increases flame stretch which

may increase chemical reaction because of a larger flame surface area or extreme flame stretch may lead to flame quenching.

Reynolds Averaged Navier Stokes (RANS) equations are used widely in numerical simulation of combustion because the computation of instantaneous flow field in a turbulent flame is not possible. RANS equations require closure rules: turbulent transport closure model to describe the flow dynamics and a turbulent combustion model to describe chemical species conversion and heat release . Solving these equations provide an averaged solution over time for stationary flows or averaged over different cycles for periodic flows.

Direct numerical simulations (DNS) solves the full instantaneous Navier-Stokes equation without any turbulence model; they resolve all the flow scales but computational cost is not practical for engine research [76]. DNS determines the inner instantaneous structure of flame front and also solve the smallest flow field which will require a mesh size of 10 to 50 microns. On the other hand, RANS solves for mean and average characteristics of the field and statistical position of flow features including flames. The chemistry for the flame front is not solved but chemistry is solved only for a mean flame brush. As combustion in practical scale engines [77, 78] have a flame brush thickness of 1 to 2 cm, easily solved with a 1 to 2 mm mesh. Codes using RANS techniques never resolve the inner structure of flame which will result in their difference from experiments as shown in Figure 3.1. RANS solutions provide average flow fields with larger scales which cannot capture the local scale unsteadiness.

Several groups are currently studying RANS based approach for engine research [80–82]. Global flow properties like spray and vapor penetration, ignition delay, flame lift-off length, heat release rate, pressure traces can be fairly well predicted by a RANS approach. These global experimental properties are captured in an ensemble averaged fashion, as a result, RANS based models perform well to predict them [83, 84].

The Reynolds Averaged Navier-Stokes (RANS) turbulence models available in CONVERGE are the Standard k-ε [85] , the RNG (Renormalization Group) k-ε [86], and the Rapid Distortion RNG k-ε models [87]. The original k-ε model has been

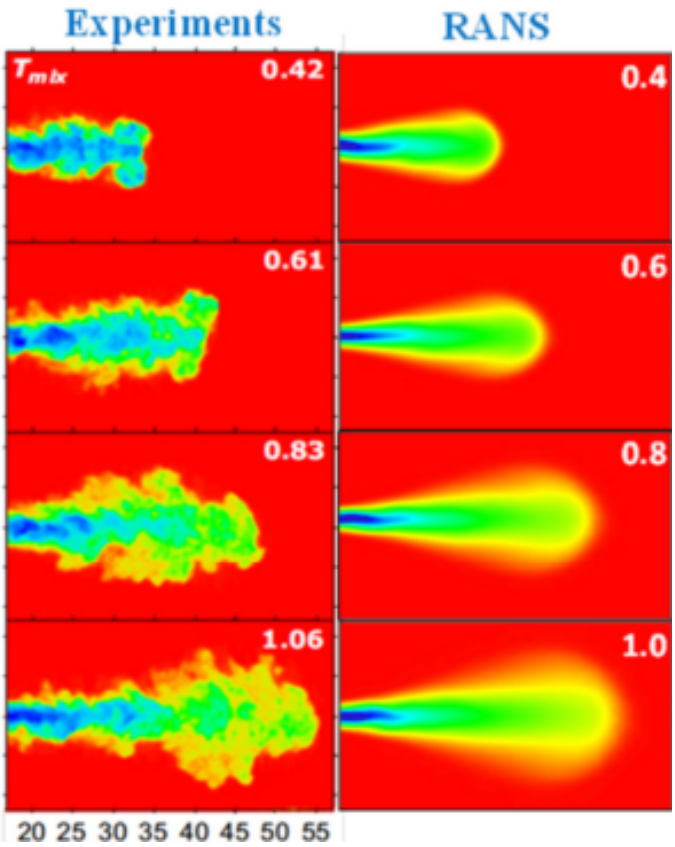

Figure 3.1. Images comparing the calculated temperature contours using RANS model against the experimental data in a constant volume non-premixed transient combustion process of injected diesel fuel. [79]

developed for incompressible thin shear flows [69]. It has been widely used because it is relatively simple and requires moderate computing time [88]. It is used in cylinder flows of internal combustion engines, which are highly turbulent and are subject to density variation, separation, recirculation and stagnation [87]. The renormalization group k-ε model proposed by Yakhot et al. [89] follows the two equation model for k and ε and is derived using the Renormalization Group Theory (RNG) for fundamental equations of fluid flow. In the high Reynolds number limit RNG k-ε [89] is almost equivalent to standard k-ε model. The latest version of RNG k-ε model proposed by Yakhot et al. [86] includes an additional term for ε-equation. This extra

term, η=S*k/ε, which is the ratio of turbulent to mean strain time scale, changes dynamically with turbulence strain rate which provides more accurate predictions for flows with rapid distortion and anisotropic large scale eddies [86, 87]. Application of the RNG k-ε model in modeling of homogeneous shear flows and separated flows [90] yielded excellent results where standard k-ε model predictions were not very successful. For all the simulations throughout this current study RNG k-ε model is considered.

3.2 SAGE Chemical Kinetics Solver

SAGE [57, 91] is a detailed chemical kinetics solver which is incorporated into the commercial CFD package CONVERGE. SAGE model uses CHEMKIN formatted input files for kinetic calculations. An overall chemical reaction can be described by a set of elementary reactions. SAGE calculates the reaction rate for every elementary reaction and CFD solves the transport equations. A reaction mechanism can be written as:

$$\sum_{m=1}^{M} \nu'_{m,r}\chi_m \Longleftrightarrow \sum_{m=1}^{M} \nu''_{m,r}\chi_m \qquad for\ r = 1, 2, ...R \tag{3.1}$$

Here R is the total number of reactions and χ_m is the chemical symbol of species m. $\nu'_{m,r}$ and $\nu''_{m,r}$ are the stoichiometric coefficients of reactants and products respectively for species m and reaction r. The net production rate can be calculated from:

$$\dot{\omega}_m = \sum_{r=1}^{R} \nu_{m,r}\zeta_r \qquad for\ m = 1, 2, ...M \tag{3.2}$$

Where M is total number of species, ζ_r is rate-of-progress variable and

$$\nu_{m,r} = \nu''_{m,r} - \nu'_{m,r} \tag{3.3}$$

ζ_r can be calculated from

$$\zeta_r = k_{fr} \prod_{m=1}^{M} [X_m]^{\nu'_{m,r}} - k_{br} \prod_{m=1}^{M} [X_m]^{\nu''_{m,r}} \tag{3.4}$$

Here k_{fr} and k_{br} are forward rate coefficient and backward rate coefficients respectively for reaction r. $[X_m]$ is the molar concentration of species m. The forward and backward rate coefficients can be written in Arrhenius form:

$$k_{fr} = AT^b exp^{(-E_A/R_u T)} \tag{3.5}$$

Here A is a constant named pre-exponential factor, b is temperature constant, E_A is activation energy and R_u is universal gas constant. The backward rate coefficient can also be calculated from equilibrium coefficient calculations. A, b and E_A are given in a reaction mechanism for each elementary reaction.

3.3 Low Damkohler Number (LDN) Combustion Model

Damkohler number is a dimensionless number which is the ratio of flow time scale and chemical time scale. If in a region flow time scale is reasonably low compared to chemical time scale (means everything is fully mixed), that is called low Damkohler number region. Well stirred reactor is a good example of low Damkohler number region.

In CONVERGE, a LDN combustion model is present which is named "SAGE". With the assumption of well stirred reactor, reaction rates are calculated using the mean values of the species present in the computational cells. This LDN combustion model can be used for premixed, non-premixed or mixing controlled combustion regime [69] with a suitable reaction mechanism for fuels. Turbulent fluctuations are neglected after a certain limit. Before ignition, chemical timescale is larger than turbulent mixing timescale. As a result, it is assumed that ignition is controlled by chemical kinetics and mainly depends on oxidation of fuel. Laminar flames, even when wrinkled by turbulence, are very thin, typically of the order of 1 mm. The grid resolution used in RANS models with LDN model are not fine enough to solve

at the flame front. Mesh size also has to be under 1 mm to resolve the flame thickness. Thus artificial diffusion coefficient is added to numerically thicken the flame. This diffusion term is also added to the turbulent burning velocity which results into increasing the value of the burning velocity and over-predicting the reaction rate. With these assumptions LDN model is found to be faster compared to turbulence chemistry interaction combustion (example: hybrid eddy breakup) models. Also reasonably good prediction is found when compared with pressure history inside the combustion chamber for diesel combustion [79, 91] and constant volume jet ignition and combustion [92]. But LDN model is not suitable for high Damkohler number regions where combustion is chemistry controlled.

3.4 G-equation Combustion Model

G-equation is a widely used model for pre-mixed combustion. In any kind of flame, chemical reactions occur in a relatively thin reactive layer. In a turbulent flow the local laminar flame that is thinner than turbulent scales called a flamelet. Turbulent flame can be seen as a group of laminar flamelet in a non-reacting turbulent flow [93] and can be separated from turbulent flow. G-equation model [94] is developed with this assumption. The flame front is described by a non-reactive scalar G = 0. The flame front divides the flow field into two regions, unburnt where G < 0.0 and burnt G > 0.0 (showed in Figure 3.2). Now, the turbulent flame front can be tracked by solving G for mean and variance.

For G-equation model the turbulent flame speed is solved from:

$$s_t = s_l + u^{'}[-a_4 b_3^2 l^* D_a/2b_1 + [(a_4 b_3^2 l^* D_a/2b_1)^2 + a_4 b_3^2 l^* D_a]^{1/2}] \tag{3.6}$$

where u' is the root mean square of the turbulent fluctuating velocity, s_l is the laminar flame speed, a_4, b_1, and b_3 are modeling constants derived from turbulence model and Da is the Damkohler number. To solve the laminar burning velocity s_l, several correlations are available in CONVERGE for methane, propane, methanol, ethanol and iso-octane.

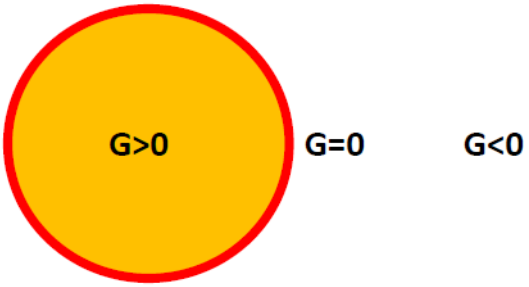

Figure 3.2. Value of non-reactive scalar G at: burnt region (G > 0), flame front (G = 0) and unburnt region (G < 0).

The G-equation is a flame propagation type model which was developed and used specifically for turbulent premixed flames. Turbulent burning velocity in G-equation model is dependent on laminar burning velocity and determined from the coefficients. These coefficients are calculated from experimental data provided for laminar burning velocity. Turbulent burning velocity is an input in G-equation model and not derived from reaction rate calculations. Typically, the grid size used in simulations is not adequate enough to solve the flame thickness. This G-equation approach overcomes this difficulty. But this model does not include detailed reaction mechanism, which may produce simplified results.

3.5 LDN and G-equation Combustion Model for Jet Ignition in a CVC

Hot jet ignition in constant volume combustor can be described as a premixed type combustion. Detailed 3D simulations for G-equation and LDN model are conducted for two different conditions. CFD software CONVERGE provides several options with G-equation model to predict soot, knocking and NO_x. From them, 'G-equation with SAGE inside and outside of the flame' is selected. In this model turbulent burning velocity is solved with G-equation but detailed chemistry is used inside (burnt region) and outside (unburnt region) of the flame to predict knocking with a suitable reaction mechanism. The burnt and unburnt region is determined from the G values. Two cases which are considered for simulation study are:

Case 3.1: The pre-chamber gas composition is that of combusted product of methane-air combustion for $\phi = 1.1$, and the pre-chamber temperature is 2600 K. The pre-chamber temperature is calculated from equilibrium calculation of constant volume methane-air combustion. CVC chamber has uniformly mixed air and pure methane fuel with $\phi = 1.0$ at temperature 300 K and pressure 101325 Pa.

Case 3.2: The pre-chamber gas composition is that of the combusted product of hydrogen-air combustion for $\phi = 1.1$, and the pre-chamber temperature is 2770 K. The pre-chamber temperature is calculated from equilibrium calculation of constant volume methane-air combustion. CVC chamber has uniformly mixed air and 60% methane + 40% hydrogen (by volume) fuel with $\phi = 1.0$ at temperature 300 K and pressure 101325 Pa.

Pre-chamber temperature and species are calculated using the equilibrium calculation which assumes complete combustion. In experiments, it is possible that incomplete combustion happens and products from the incomplete combustion (hot-jet) bursts through the nozzle into the CVC chamber. This hot-jet from incomplete combustion can have lower temperature compared to the value from equilibrium calculation. Also it may contain higher amount of radicals and unburnt fuel which may affect the ignition chemistry. This is one of the limitations of this study.

It is to be noted that for Case 3.2, both pre-chamber and CVC chamber gas are more reactive than Case 3.1 because of inclusion of H_2. The main objective of this part of the study is to compare two different assumptions for turbulent burning velocity calculation. As Case 3.1 fails to ignite within the simulation time, with trial and error, conditions of Case 3.2 is carefully chosen so that clear indication of ignition, flame propagation, and combustion can be established within the simulation time frame (1.6 ms).

As combustion of pure methane at room temperature is very slow, a blend of methane and hydrogen is considered. Such mixtures allow laboratory experiments to simulate faster reaction rate conditions that are of interest in actual applications with initial mixtures at high temperature, while using room temperature or moderate

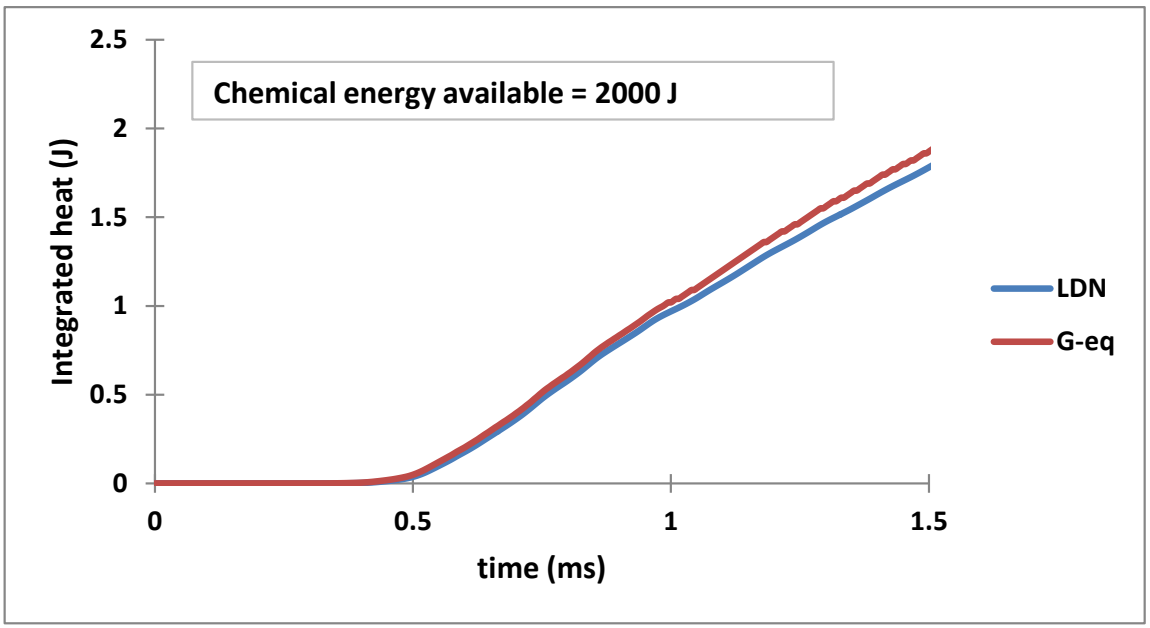

Figure 3.3. Integrated heat release in CVC chamber for Case 3.1.

temperature. Also pure hydrogen is considered as pre-chamber gas which increases the amount of H radicals in pre-chamber combusted gas. H radicals attack the CH_4 molecules and creates CH_3 radicals, as a result increase reaction rate and decrease ignition delay. For both cases, pre-chamber pressure is 649 kPa and DRM-19 (reaction mechanism is explained later) used as a detailed reaction mechanism.

For Case 3.1, after 1.6 ms the total heat released is only 2 J which indicates that there is no indication of ignition inside the CVC chamber for pure methane (Figure 3.3). Total amount of chemical energy available in CVC is 2000 J. In Figure 3.4, CH_4 mass inside the CVC chamber supports this statement by showing no disintegration. Although without ignition, both models show similar trends in heat release.

Integrated heat release inside the CVC chamber refers to the total amount of thermal energy produced from chemical reaction from burning the fuel in the CVC chamber. This is plotted in Figure 3.5. SAGE and G-equation, both combustion models predict the ignition delay around 0.7 ms and show a similar trend. The

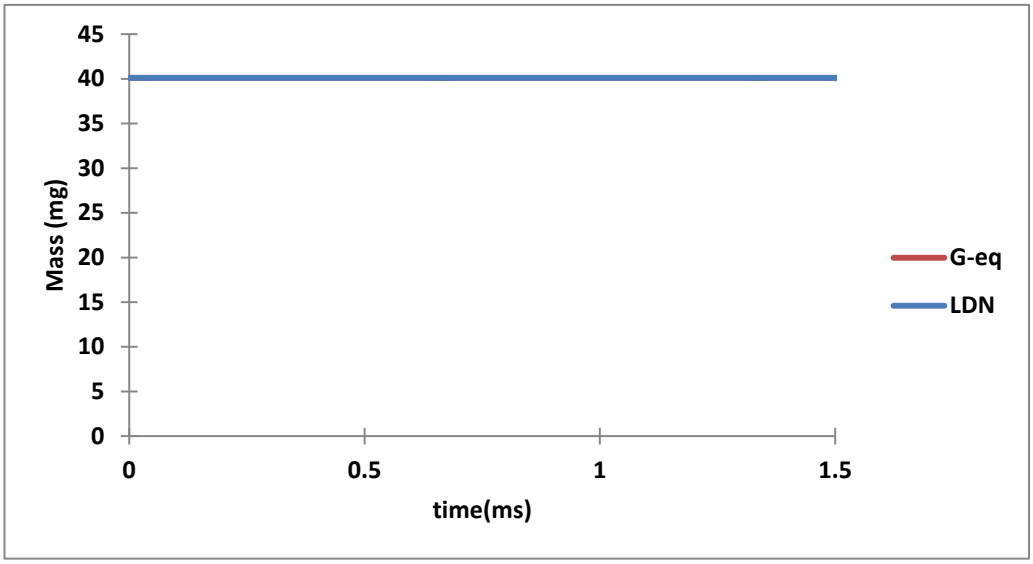

Figure 3.4. CH_4 mass in CVC chamber for Case 3.1.

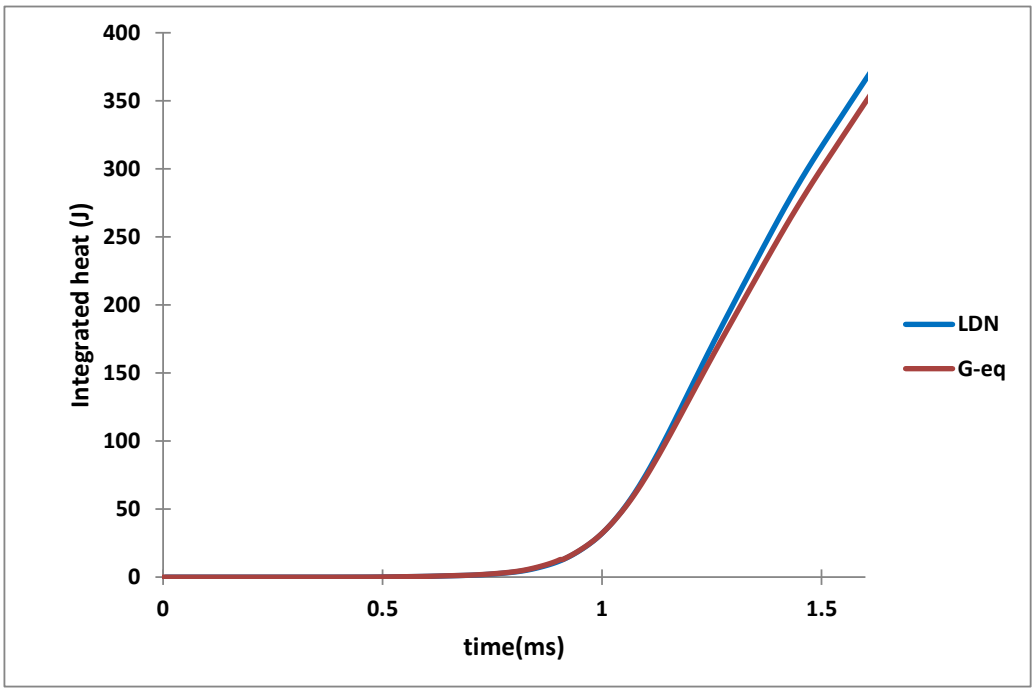

Figure 3.5. Integrated heat release in CVC chamber for Case 3.2

heat release rate (HRR) plot in Figure 3.6 shows more insight into the combustion process. Significant chemical reaction or fuel burning starts around 0.7 ms. Then

highest HRR occurs at about 1.2 ms because of flame propagation and increase in flame front area. The ignition delay, trend of the HRR curve, sudden rise and decline are similar for the two combustion models. Although the simulations are in 3D, for better representation temperature is plotted in 2D (a plane through the center of the nozzle) for both combustion models in Figure 3.7. Ignition and combustion start at the center, flame propagates suddenly and after 1.2 ms flame propagates smoothly. Both models show same type of phenomena within the simulation time range.

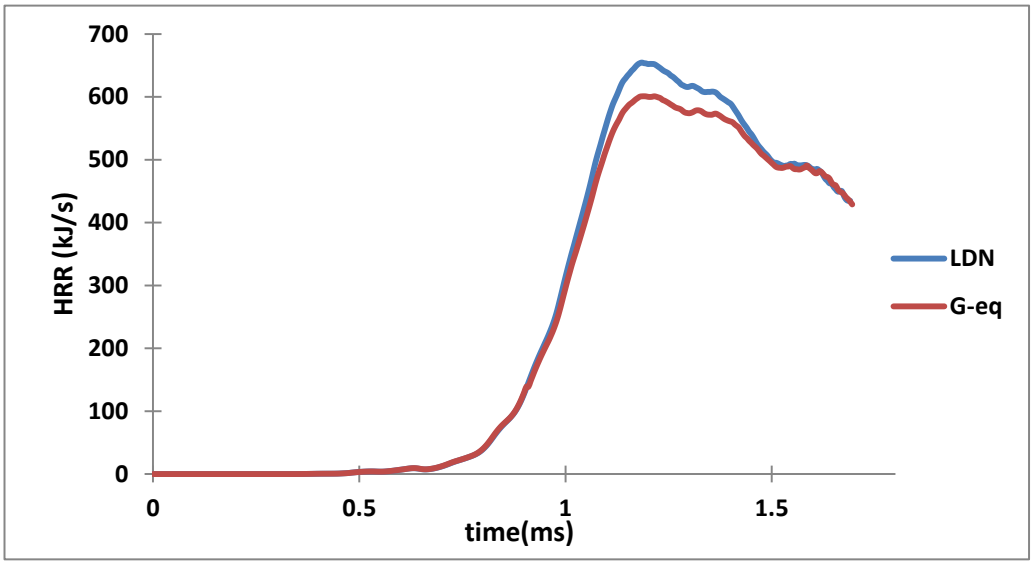

Figure 3.6. Heat release rate in CVC chamber for Case 3.2

LDN model artificially increases the flame thickness to solve with reasonably coarse grid by artificially increasing the turbulent burning velocity. G-equation model uses turbulent burning velocity as an input and overcomes the limitation of LDN model regarding artificial flame thickness. But inherently calculating turbulent burning velocity from laminar burning velocity by semi-empirical equation (equation 3.8). These are the fundamental differences between these two models. Jet ignition in CVC is probably mixing controlled which can be predicted by LDN model with reasonable well refined grid size provided by AMR. The fundamental difference between these two models is in flame speed calculation which is also found to be almost identi-

cal. Very fast deflagrative type turbulent flame in jet ignited CVC has a very high observed flame speed, which is due to combusted gas flow velocity due to pressure difference between pre-chamber and CVC chamber (explained in detail later). Freely propagating turbulent flame has maximum velocity around 5 m/s. Turbulent burning velocity is not well-defined. Hence the better measure of combustion rate is the heat release rate. Heat release and flame propagation which is dominated by the fluid dynamics and can be solved with LDN model with AMR.

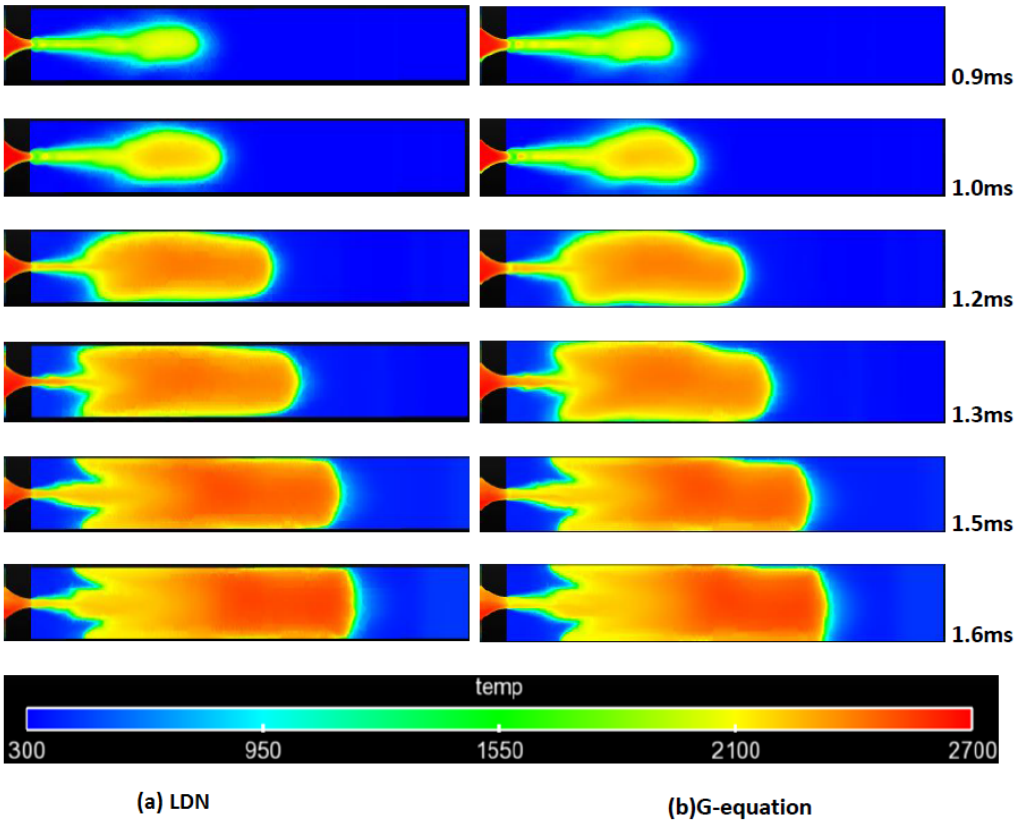

Figure 3.7. Temperature plot in CVC chamber for (a) LDN and (b) G-equation model for Case 3.2

Wave rotor combustion with pre-chamber jet ignition system can be compared with premixed type combustion but in reality it is a very complex process. Hot jet mixing with stationary fuel-air in CVC chamber, fuel entrainment and active radicals in the hot jet play vital role in the combustion process. Detailed chemical kinetics

model- LDN combustion model (SAGE) is chosen throughout this study for the combustion reaction rate calculations. SAGE detailed reaction rate calculation model can be successfully used in premixed, non-premixed, partially premixed combustion regime. This detailed chemical kinetics model- SAGE with adaptive mesh refinement and multi-zone reaction modeling has been widely used for internal combustion engines [57, 91], constant volume diesel experiment [79] and recently for pre-chamber constant volume combustor [30, 92].

3.6 Reaction Mechanism

SAGE detailed chemical kinetics calculate the reaction rates solely based on the detailed reaction mechanism provided for the fuel because turbulence chemistry interaction is not considered. As a result, reaction mechanism chosen for the fuel supplied has huge effect on predicting the ignition delay. Throughout this study, mainly two fuel mixtures of equivalence ratio 1.0 are considered. First one is a blend of 50%CH_4 + 50%H_2 (by volume), second one is a blend of 30%CH_4 + 70%H_2 (by volume). To the knowledge of the author, no reaction mechanism is exclusively created for methane-hydrogen blends. Several detailed reaction mechanisms are available for methane which also includes detailed oxidation mechanism for hydrogen.

The detailed reaction mechanism GRI-Mech 3.0 [73] for natural gas which contains 53 species and 325 elementary reactions might be one of the most used ones because it is very well known and experimentally tested. A reduced reaction mechanism DRM19 [95] is also available which consists of 84 elementary chemical reactions with associated rate coefficient expressions and thermochemical parameters for 21 species. DRM19 is derived from GRI Mech 1.2 [96]. DRM19 is tested within a wide range of conditions (equivalence ratio = 0.2-2.0, initial pressure = 0.1-50 atm, and initial temperature = 1300-2500 K). DRM19 performs well and deviations are within 6-8 % when compared with GRI-Mech 3.0. The deviations start to increase at lower temperature and higher pressure [97]. As an example, at T_o = 1100 K,

P_o = 10 atm and PHI = 0.2, the ignition delay calculated with DRM19 has 37% error when compared to GRI-Mech 3.0. [97]. However the authors did not carry out any extensive research because GRI-Mech 3.0 is also not validated at very high pressure. Several other reaction mechanisms are available for methane combustion. The RAMEC mechanism [98] consists of 38 species and 190 elementary reactions based on GRI Mech 1.2 mechanism. The RAMEC mechanism includes important reactions for methane oxidation at lower temperature or higher pressure. The detailed mechanism for methane oxidation developed at the University of Leeds [99] consists of 351 elementary reactions and 38 species and based on the same experiments as GRI Mech 3.0. The computational time increases proportionally with number of reactions and roughly as the square or cube of the number of species [100]. So, it is necessary to choose a reaction mechanism which will cover the range of the thermodynamic properties such as temperature or pressure, predict well the characteristics of ignition and combustion, and also keep the computational time within a realistic limit. As studying ignition process is one of the major goals of this study, relatively reduced reaction mechanism DRM19 and detailed mechanism GRI Mech 3.0 are chosen to study their effects on ignition and combustion.

3.6.1 Reaction Mechanism Effects on Ignition and Combustion

Detailed 3D simulations are conducted for centered stationary jet. Two different cases are considered with different pre-chamber and CVC chamber fuel. DRM19 and GRI Mech 3.0 are considered as reaction mechanism for both cases.

Case 3.3: Pre-chamber fuel is the combusted products of slightly rich pure hydrogen gas. CVC chamber contains 50%CH_4 + 50%H_2 (by volume) with equivalence ratio 1.0. Pre-chamber temperature is calculated from constant volume equilibrium calculation. Pre-chamber pressure is 649000 Pa. CVC chamber has temperature 300 K and pressure 101325 Pa.

Case 3.4: Pre-chamber fuel is the combusted products of slightly rich blend of 50%CH_4 + 50%H_2 (by volume) and air mixture. CVC chamber contains 50%CH_4 + 50%H_2 (by volume) with equivalence ratio 1.0. Pre-chamber temperature is calculated from constant volume equilibrium calculation. Pre-chamber pressure is 649000 Pa. CVC chamber has temperature 300 K and pressure 101325 Pa.

It should be noted that, Case 3.3 contains a higher reactive fuel than Case 3.4. From several trial and error these fuel combinations are selected. Case 3.3 contains higher amount of H and OH radicals and expected to start the ignition in CVC chamber within the simulation time. Case 3.4 has lower amount of active radicals in hot-jet. As a result it may not start the ignition in CVC chamber within the simulation time and labeled as chemically inert jet.

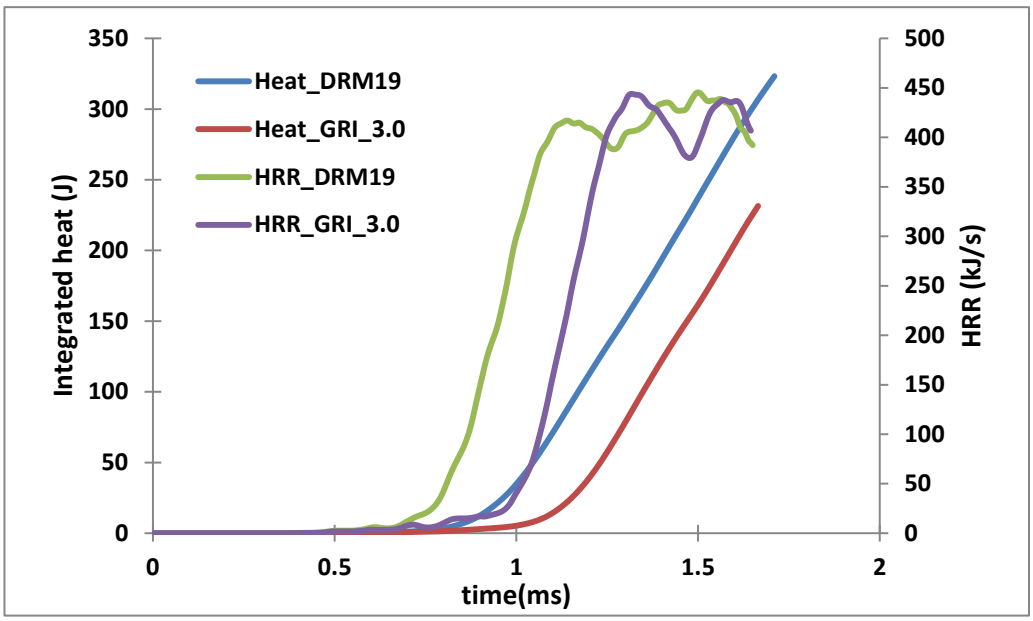

Figure 3.8. Integrated heat release and heat release rate in CVC chamber for Case 3.3.

For Case 3.3, when combusted products of pure hydrogen are used as pre-chamber jet, there is a clear indication of ignition and combustion. The total amount of heat release from Figure 3.8 and amount of methane mass in CVC from Figure 3.9 indicates that ignition starts and combustion occurs in CVC chamber. A point to be noted

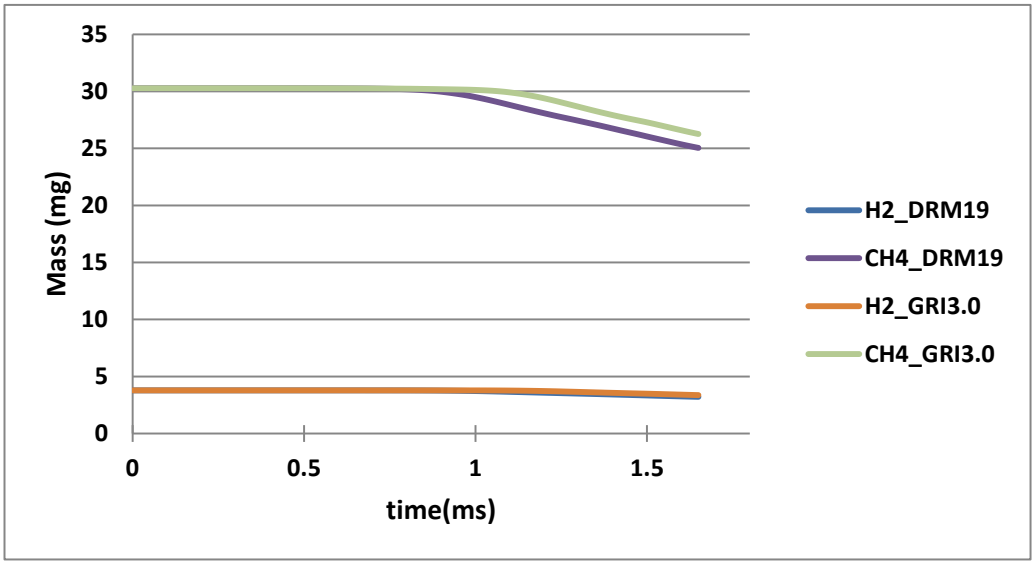

Figure 3.9. Fuel mass (hydrogen and methane) in CVC chamber for Case 3.3.

is, relatively reduced mechanism DRM19 predicts the ignition about 0.25 ms earlier than the detailed GRI 3.0 mechanism. But both the integrated heat release and heat release rate shows similar patterns. At high temperature ignition delay is mainly controlled by the chain branching reaction H + $O_2 \Leftrightarrow OH + O$, and at middle-low temperature by the chemistry of HO_2 and H_2O_2 radicals for methane/hydrogen mixtures [101]. OH mass in CVC chamber from Figure 3.10 shows about 0.25ms delay in producing for GRI 3.0. But after OH starts to generate, the rate of production is same for both mechanisms. It is expected that the ignition delay will be sensitive to the kinetic mechanism. The subsequent flame propagation rate appears to be not so sensitive. Minor species like CH_3 and HO_2 mass has been plotted in Figure 3.11. Both CH_3 and HO_2 shows that the production starts around 0.4ms for both reaction mechanisms but there is a delay to reach the peak value, meaning production rate of CH_3 and HO_2 is slower for GRI 3.0.

For Case 3.4, when combusted products of methane-hydrogen blends are used as pre-chamber jet; no clear indication of ignition and combustion is found. Figure 3.12 shows that integrated heat release within the simulation time period is only 2.0 J.

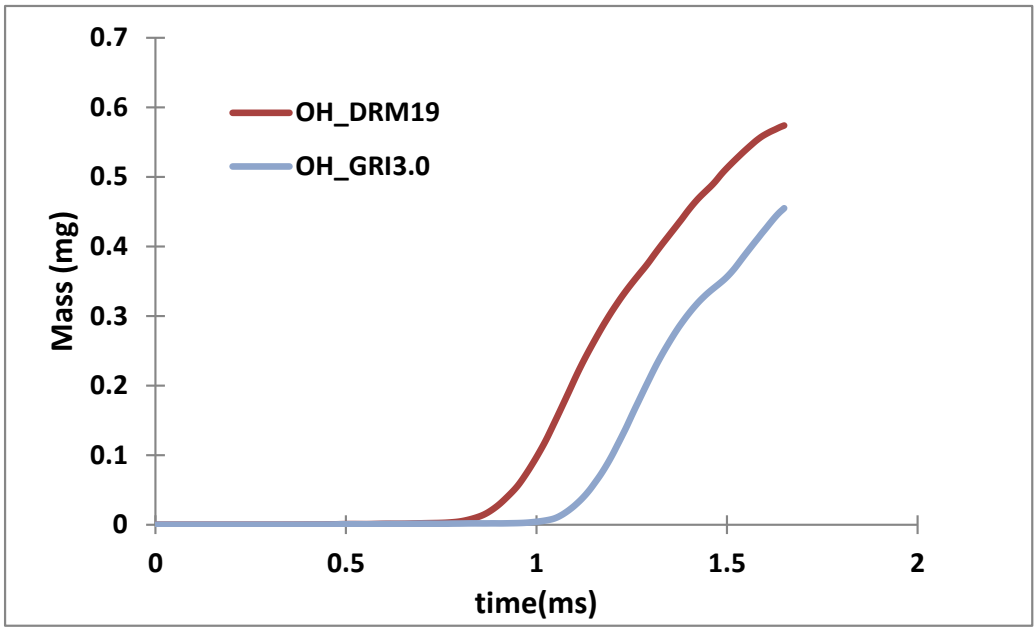

Figure 3.10. OH mass in CVC chamber for Case 3.3.

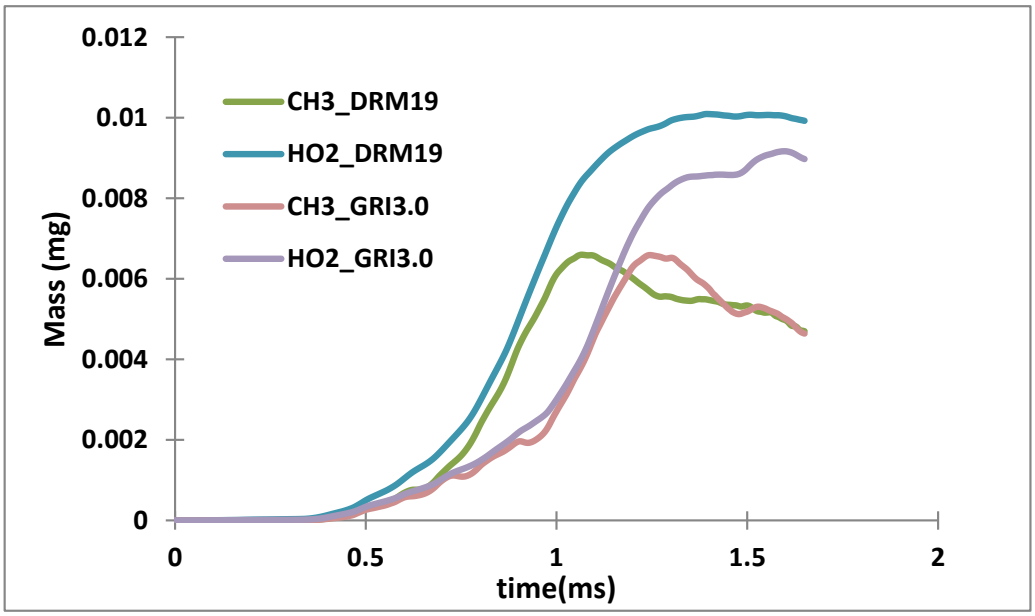

Figure 3.11. Minor species in CVC chamber for Case 3.3.

Mixing of hot jet with the quiescent fuel blend of CVC chamber starts the chemical reactions which start producing heat around 0.5ms but they are not producing enough

heat to start the ignition. Both integrated heat and heat release rate show same patterns although DRM19 slightly over-predicts the amount of heat released.

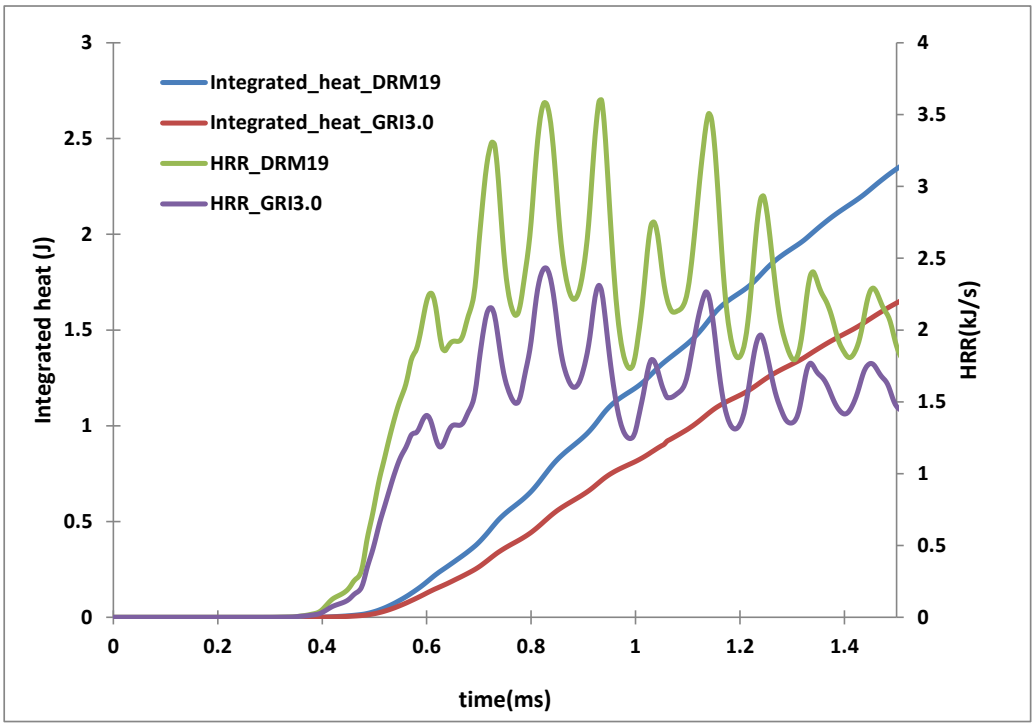

Figure 3.12. Integrated heat release and HRR in CVC for Case 3.4

For both chemically-reacting (Case 3.3) and chemically-inert (Case 3.4), DRM19 and GRI 3.0 show same patterns but DRM19 predicts the ignition earlier for Case 3.3. It might be stated that, species which are important in predicting ignition delays at low temperature like H_2O_2 are unavailable in DRM19 is one of the reasons. But DRM19 is able to predict the patterns of heat release and species production well when compared with GRI 3.0 for both low and high temperature. As one of the main goals of this study is to understand the physics behind this very complex jet ignition system and keeping in mind the savings in computational cost, predictions using DRM19 are deemed adequate and are the basis of discussion henceforth.

4. EFFECTS OF ACTIVE RADICALS ON JET IGNITION

4.1 Reactive and Chemically Inert Jet

In this section of the study, combusted products of slightly rich mixture of methane is used as a pre-chamber fuel. In CVC chamber, methane with an equivalence ratio of 1.0 is used. It is assumed that, combusted products in the pre-chamber include active radicals to initiate ignition in main chamber. Detailed 2D simulation of compressible, transient, turbulent, chemically reactive flow is studied. Jet with active radicals is compared with relatively inert species jets which are thermally comparable with active radical jet but chemically different. Temperature, heat release rate and mass of different species are compared to understand the effects of active radicals on ignition and combustion.

To separate the effect of chemical and thermal aspects of hot jet, the ignition following steps were considered:

1) From constant volume equilibrium calculations, reactive hot jet calculation of equilibrium composition is done for the pre-chamber mixture for all the species to be used in the kinetic calculation.

2) ΔH and ΔU of this reactive mixture (enthalpy and internal energy) is calculated for the temperature difference between pre-chamber and CVC chamber. Pre-chamber temperature is calculated from simple constant volume equilibrium calculation and CVC chamber temperature is 300 K.

3) A mixture of three inert gases: N_2, Ar and He is considered.

4) The three free variables are adjusted so that mass, energy and densities of the inert jets are exactly the same as the chemically reactive jet. This is still ambiguous because the mass of gas injected exchanges work with the surroundings, and the process is neither constant-volume nor constant-pressure. Therefore, two forms of

energy balance are considered, constant enthalpy (H) and constant internal energy (U). This is done by solving three simultaneous algebraic equations, and is elaborated in Appendix C.

4a) Three free variables(mass fraction of N_2, Ar and He) are calculated so that the inert mixture average molecular mass (i.e. density) and the total ΔH is the same as for the reactive mixture in the pre-chamber.

4b) Three free variables(mass fraction of N_2, Ar and He) are calculated so that the inert mixture average molecular mass (i.e. density) and the total ΔU is the same as for the reactive mixture in the pre-chamber.

After solving the algebraic equations results and conditions of the pre-chamber and the CVC chamber are shown in Table 4.1:

In Table 4.1, second column (Case 4.1 Reactive) is showing the mass fractions and temperature of the reactive species which is calculated from equilibrium calculation. Third column (Case 4.2 Inert-Matched ΔH) is showing the mass fractions of the inert species which calculated by solving a set of algebraic equations for matched enthalpy (explained in Appendix 3). Fourth column (Case 4.3 Inert-Matched ΔU) is showing the mass fractions of the inert species which calculated by solving a set of algebraic equations for matched internal energy (explained in Appendix 3). In Table 4.1, The composition for Case 4.1 is the mass fraction of reactive species in pre-chamber. For Cases 4.2 and 4.3, the composition is the mass fraction of the inert species for matched enthalpy and matched internal energy, respectively, with the Case 4.1 composition. Case 4.2 and 4.3 have the exact same amount of enthalpy and internal energy respectively as the reactive mixture, so the differences they will make with respect to ignition delay will be only due to chemistry but not due to the amount of energy and mass injected.

Table 4.1. Initial conditions considered for simulation. Case 4.1: Mixture with Active Radicals Case 4.2: Matched Enthalpy (ΔH), Case 4.3: Matched Internal Energy (ΔU)

Mass fraction, Y	Pre-chamber			CVC chamber
	Case 4.1 Reactive	Case 4.2 Inert-Matched ΔH	Case 4.3 Inert-Matched ΔU	
He	0	0.0905	0.2152	0
CH_4	0	0	0	0.0552
Ar	1.21×10^{-2}	0.2248	0.4755	0
CO	3.40×10^{-2}	0	0	0
CO_2	1.11×10^{-1}	0	0	0
H	6.08×10^{-5}	0	0	0
H_2	1.01×10^{-3}	0	0	0
H_2O	1.23×10^{-1}	0	0	0
NO	3.31×10^{-3}	0	0	0
N_2	7.08×10^{-1}	0.6847	0.3092	0.7247
O	2.41×10^{-4}	0	0	0
OH	3.64×10^{-3}	0	0	0
O_2	2.65×10^{-3}	0	0	0.2201
Temperature(K)	2670	2670	2670	300
Pressure(bar)	6	6	6	1

4.1.1 Ignition and Combustion Characteristics

Ignition delay time had been variously defined in the literature on spark-ignited and compression-ignited engines, and on shock tubes. Ignition can be identified by

tracing sudden rise of heat release rate, pressure or certain species concentration (such as [OH]). For this specific case, the complexity to define ignition delay time is more because chemically active hot jet from pre-chamber mixes with cold air fuel mixture in main chamber. This mixing process is dependent on entrainment ratio or mixing rate. Ignition delay time for present work is determined by several parameters, such as heat release rate and different intermediate species mass.

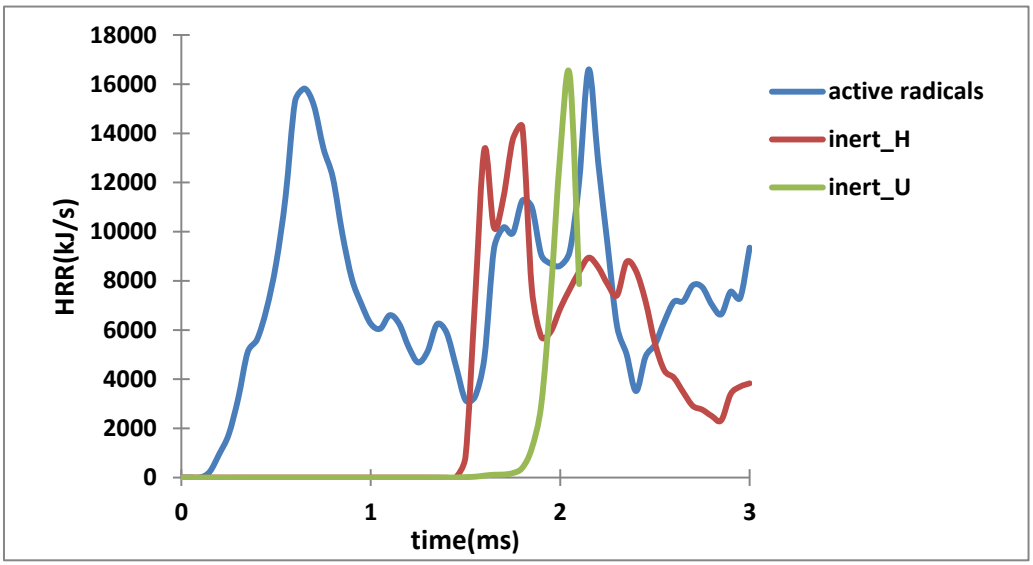

Figure 4.1. Heat release rate variation for stoichiometric methane mixture for active radicals (Case 4.1), inert H (Case 4.2) and inert U (Case 4.3)

Figures 4.1 through 4.6 will be analyzed carefully to understand the effects of active radicals (H,O,OH and NO) on ignition and combustion in a the constant volume combustor (main chamber). Heat release rate is a good indicator of ignition delay time. From Figure 4.1, it is concluded that for active radicals ignition starts at 0.6 ms whereas for inert species ignition starts at 1.5 ms (Case 4.2) and 2.0 ms (Case 4.3). Total simulation time was 2.5 ms which was not enough to complete the combustion process. For this reason, the heat release curve (Figure 4.1) and also the amount of fuel consumption (Figure 4.3) is do not become zero. Figure 4.3 shows the amount of fuel (methane) consumption with time in the main chamber. It is observed that for

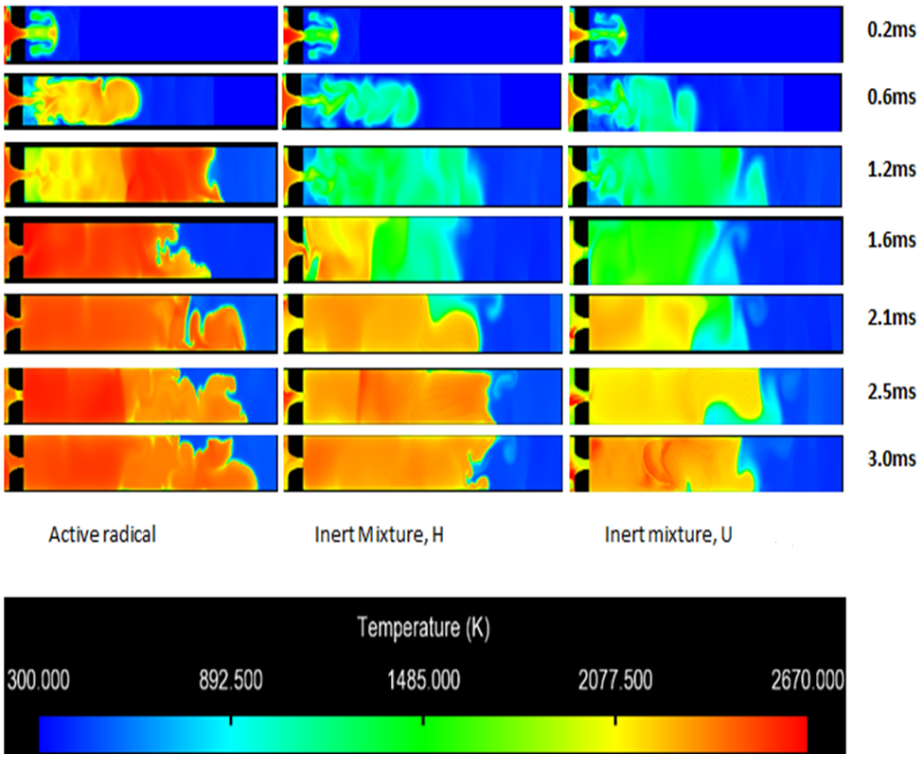

Figure 4.2. Temperature level of stoichiometric methane combustion in CVC chamber for active radicals (Case 4.1), inert H (Case 4.2) and inert U (Case 4.3)

the jet containing active radicals, the consumption starts earlier than inert species cases. The only difference between the cases with active radicals (Case 4.1) and inert species (Case 4.2 4.3) is the chemical activity as enthalpy is same for Case 4.2 and internal energy is same for Case 4.3. Active radicals start the reaction around 12.0 ms earlier than Case 4.2.

To analyze the combustion characteristics, temperature levels for three different cases are presented in Figure 4.2. Shock wave interaction with flame front plays a vital role in ignition and combustion. At 1.2 ms the flame front retracts back is observed to regress for all the three cases which indicate the collision of shock wave with the flame front. This collision immediately increases the temperature for active radicals (Case 4.1) but the temperature rise is late for Case 4.2 and 4.3. Figure 4.1 shows that there is a second peak at 2.1 ms for active radicals (Case 4.1) which can be

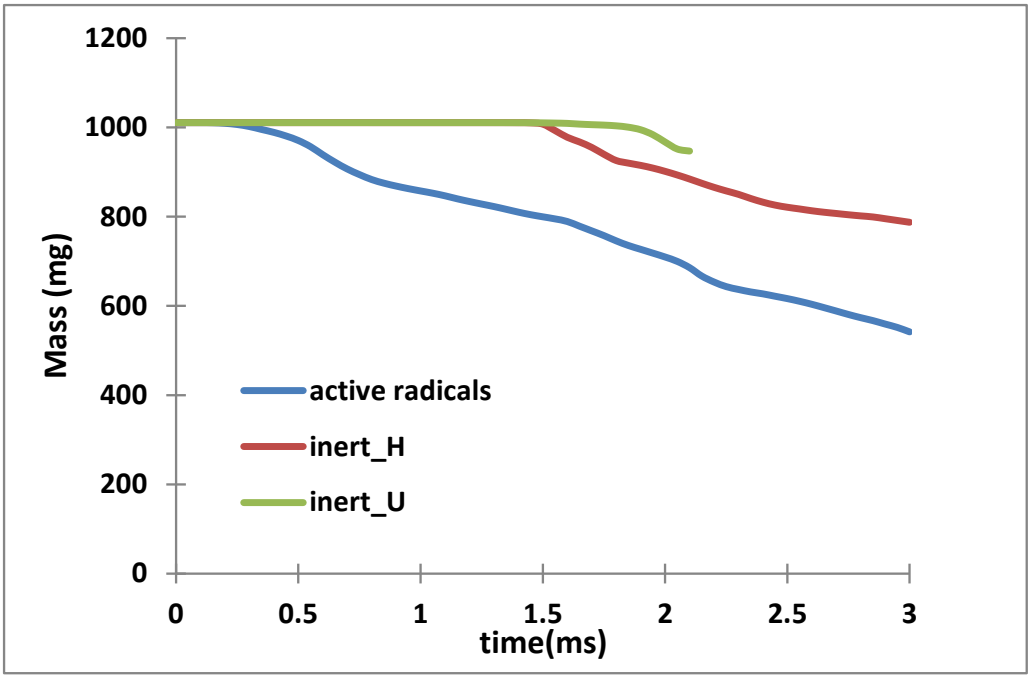

Figure 4.3. CH_4 mass of stoichiometric methane combustion in CVC chamber for active radicals (Case 4.1), inert H (Case 4.2) and inert U (Case 4.3)

explained from Figure 4.2. At 2.1 ms the flame front suddenly drives forward (Figure 4.2), which increases flame area and entrapped unburned fuel reacts which suddenly increases the heat release rate.

To understand the combustion phenomena more clearly, important intermediate single carbon C1 species (CH_3) and double carbon C2 species (C_2H_4) mass is plotted in Figures 4.4 and 4.5 over time for CVC chamber.

Ignition jet from pre-chamber entrains unburnt fuel and creates vortices which can be treated as well stirred reactor. In well-stirred reactors at high temperatures (>2000 K), the main pathway for CH_4 combustion is [102]:

$$CH_4 \rightarrow CH_3 \rightarrow CH_2O \rightarrow HCO \rightarrow CO \rightarrow CO_2 \tag{4.1}$$

At low temperatures (<1500 K), the reaction pathway of methane combustion in a well-stirred reactor is the following [102]:

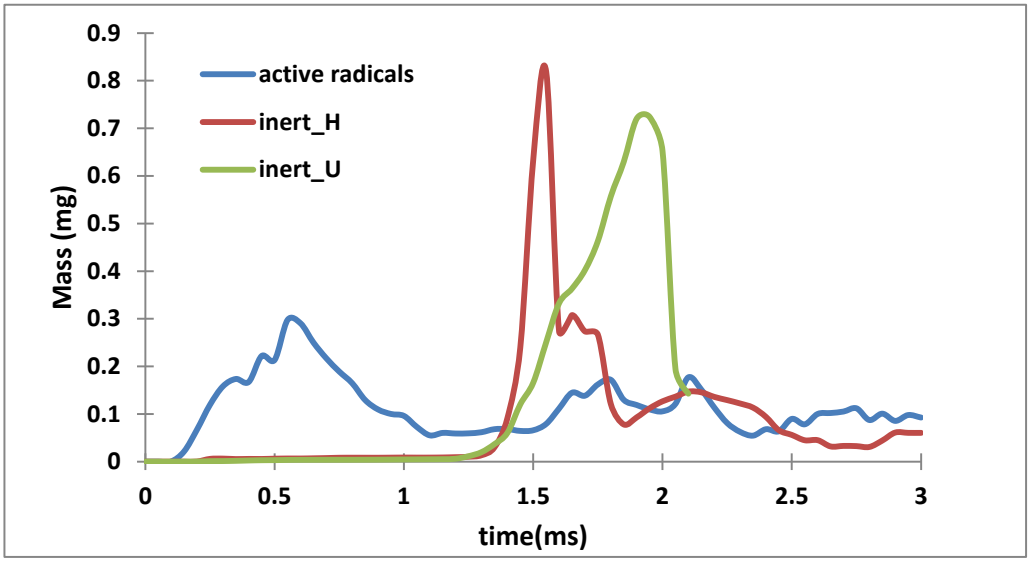

Figure 4.4. CH_3 mass of stoichiometric methane combustion in CVC chamber for active radicals (Case 4.1), inert H (Case 4.2) and inert U (Case 4.3)

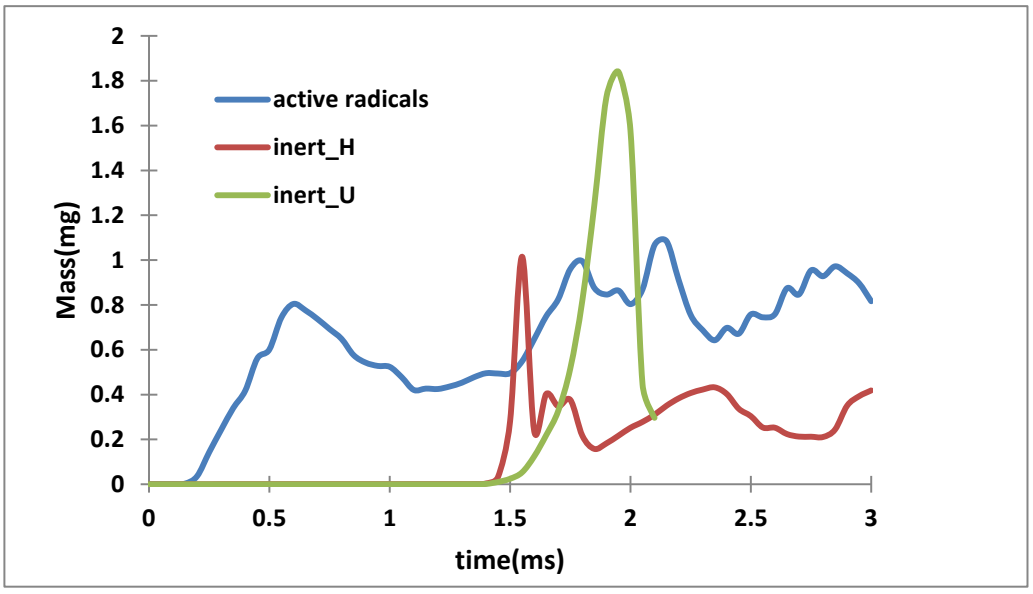

Figure 4.5. C_2H_4 mass of stoichiometric methane combustion in CVC chamber for active radicals (Case 4.1), inert H (Case 4.2) and inert U (Case 4.3)

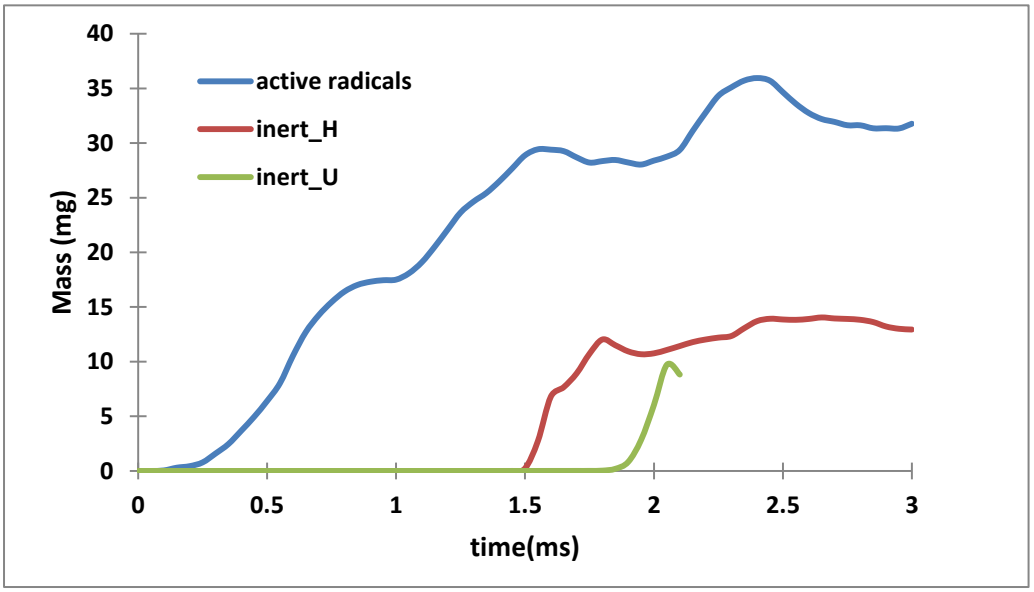

Figure 4.6. OH mass of stoichiometric methane combustion in CVC chamber for active radicals (Case 4.1), inert H (Case 4.2) and inert U (Case 4.3)

$$C_2H_6 \rightarrow C_2H_5 \rightarrow C_2H_4 \rightarrow C_2H_3 \rightarrow C_2H_2 \rightarrow CO, CH_2 \tag{4.2}$$

The appearance of hydrocarbon molecules larger than the initial reactant hydrocarbon is a feature of low-temperature oxidation processes [102]. Production of CH_3 and C_2H_4 for active radicals (Case 4.1) show that maybe both the pathways described above is important in the combustion process. For Case 4.2 and 4.3, delayed but sudden rise of CH_3 and C_2H_4 mass is observed. As for these two cases (4.2 and 4.3), ignition starts later, hot jet mixing with unburnt fuel is better because they had more time which results to stronger combustion. The sudden start of ignition had access to higher amount of unburnt fuel which explains the sudden peak. But for Case 4.3 higher amount of C_2H_4 indicates maybe domination of low temperature combustion. Mass of OH over time is plotted in Figure 4.6 as many reactions start by OH attack. Figure 4.6 indicates significant higher production of OH for Case 4.1 which reinforces

all of the prior plots showing earlier and faster combustion progress for jet containing active radicals.

Case 4.2 starts ignition earlier than Case 4.3. The main reason behind this could be the energy content. Enthalpy can be written as, $h = u + Pv$, where P is pressure and v is specific volume and u is internal energy. As a result the energy content of the hot jet in Case 4.2 is higher than Case 4.3. This implies that the jet of Case 4.2 cools down earlier which results to larger ignition delay. But the main focus of this section of the study is to compare the hot active radical jet with hot inert jets. The presence of hot active radical jet shows significant reduction in ignition delay compared to other two cases.

4.2 Effects of CVC Chamber Initial Temperature Combined with Presence of Active Radicals

Simulations in this section of study are performed for a higher initial temperature (514 K) of the methane mixture in the CVC chamber, only for the case of a stationary jet issuing from the pre-chamber. The elevated temperature corresponds approximately to the combustor inlet temperature for a gas turbine with a compressor pressure ratio of about 10. Two different sets of pre-chamber species were considered for slightly rich combusted product of ethylene. One contains only major species (Table 4.2) another contains active radicals with major species (Table 4.3). Pressure and temperature in the pre-chamber were same for both cases. For a fixed chamber volume and pressure, the density of the high-temperature mixture will be lower and the total mass of the mixture inside CVC chamber is lower. To make appropriate comparisons, the predicted heat release rate is normalized using its corresponding mixture mass in the CVC chamber.

The heat release rate per unit mass of the CVC mixture (Figure 4.7) is initially similar for the colder and hotter mixtures, with virtually no effect from the first shock-flame interaction. Shock-flame interaction occurs earlier for higher tempera-

Table 4.2. Initial conditions considered for the simulations for major species

Thermodynamic Properties and Mass Fractions	Pre-chamber and Nozzle	CVC Chamber
Pressure (kPa)	649.0	101.325
Temperature (K)	2770	298
N_2	0.7194	0.7258
O_2	0.00691	0.2192
CO_2	0.1420	0
H_2O	0.0804	0
CO	0.0504	0
H_2	0.00074	0
CH_4	0	0.0549

ture mixture as expected due to faster wave travel, with the first interaction at 0.9 ms and 1.06 ms for high and low temperature mixtures, respectively. The second interaction occurs at about 1.4 ms and 1.55 ms for high and low temperature mixtures, respectively. The second shock-flame interaction significantly increases heat release for both temperatures, with the heat release rate faster for the high temperature mixture. The integrated heat release data shown in Figure 4.8 indicates significantly faster rates for the higher temperature mixture only after about 1.5 ms.

At this point in the study, it was surmised that the delayed impact of the initial elevated temperature may be due to the fact that significant differences in chemical reaction rates occur only in a higher temperature range that is reached after initial shock compression of the mixtures that burn later in the process. The initial reaction progress may be primarily controlled by mixing processes rather than chemical kinetics. As a possible test of the impact of chemical kinetics on reaction rate in the initial

Table 4.3. Initial conditions considered for simulation for detailed species

Thermodynamic Properties and Mass Fractions	Pre-chamber and Nozzle	CVC Chamber
Pressure (kPa)	649.0	101.325
Temperature (K)	2770	298
N_2	0.6997	0.7246
Ar	0.01202	0
O_2	0.00829	0.22015
CO_2	0.1347	0
H_2O	0.0778	0
CO	0.0528	0
H_2	0.000778	0
H	0.000109	0
NO	0.00662	0
O	0.000923	0
OH	0.00611	0
CH_4	0	0.05518

jet mixing region, it was thought to increase reactivity by including active radicals in the jet.

To understand the chemical activity of the jet, simulations were conducted for the case of a centered stationary jet with the inclusion of active radicals H, O, OH, and NO, as well as normal atmospheric argon in the pre-chamber combusted mixture (Table 4.3) for the two different initial temperatures, 298 K and 514 K. It is not known whether in reality any active species that are formed during combustion in the pre-chamber would remain active as the jet emerges into the main chamber. The purpose of the additional simulations is to assess the sensitivity of the jet ignition

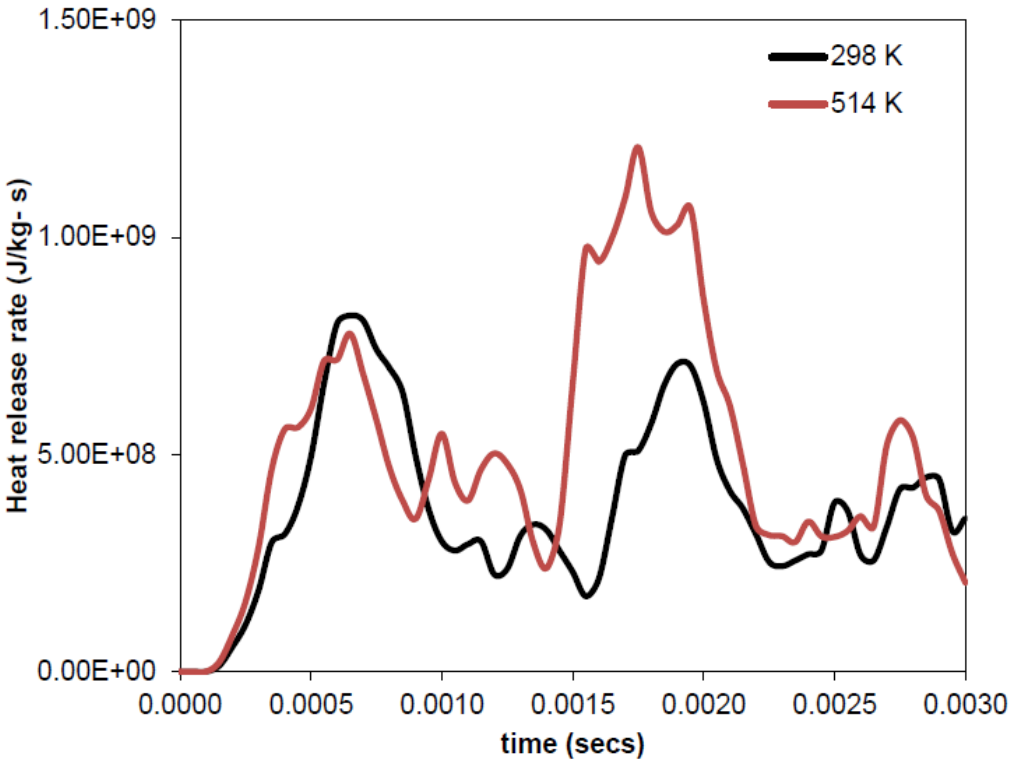

Figure 4.7. Heat release rate variation for stoichiometric methane mixture at different temperatures for only major species [2]

process to yet another chemical modulation, the first modulation being the initial temperature setting. To better understand the longer term behavior, these simulations were extended to 6 ms after initiation of jet flow into the main CVC chamber. Heat release rate and integrated heat release in the CVC chamber were normalized by the total mass for comparison between two different initial temperature cases.

The heat release rate per unit mass (Figure 4.9) has a first peak around 0.4 ms which is well before the first shock wave returns to the combustion region. This initial combustion is controlled by hot jet penetration and mixing, before any shock flame interaction. In comparison with the case without initial inclusion of radical species (Figure 4.7), this initial heat release rise is more rapid, and reaches a significantly higher peak for the higher initial temperature (514 K). By about 1.5 ms, the heat release rates for both temperatures have fallen back to a low level that is comparable

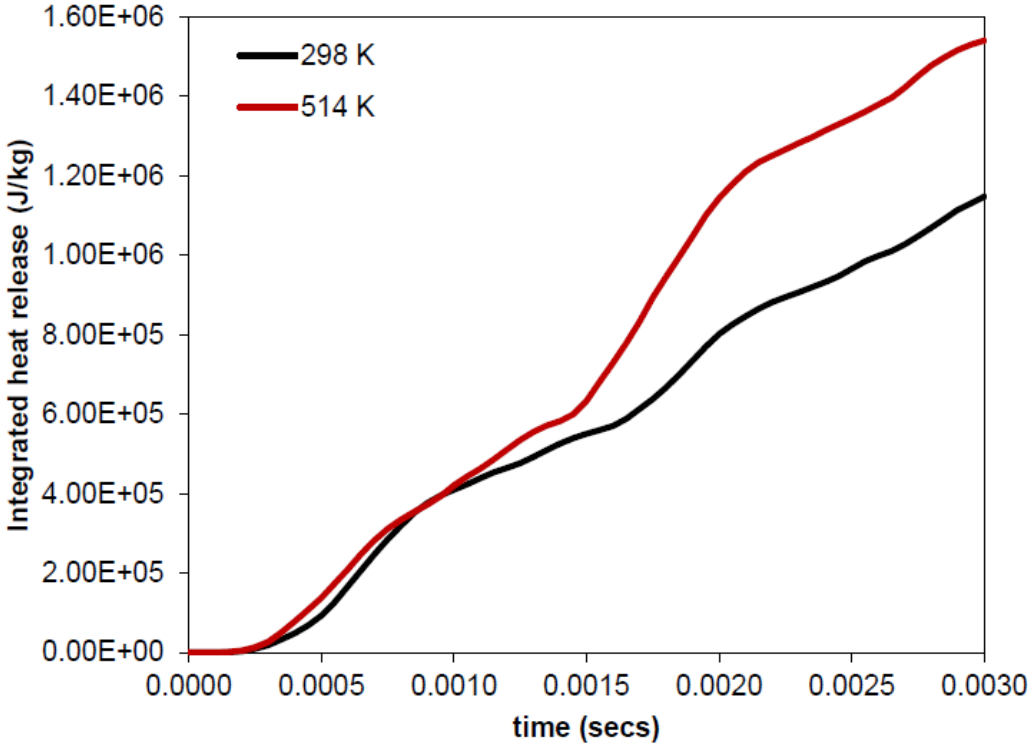

Figure 4.8. Integrated heat release for stoichiometric methane mixture at different temperatures for only major species [2]

to what was seen in the absence of initial radicals. This appears to indicate that the direct effect of initial radical species is limited to the immediate ignition process and has a multiplying effect for the higher initial temperature. However, as seen below, a small initial effect can have indirect later effects, as the pattern of pressure wave generated by the faster ignition can be different.

The first shock-flame interaction occurs at 0.9 ms and 1.05 ms for high and low initial temperature mixtures respectively, which showed very little effect on heat release rate. The second interaction occurs around 1.35 ms and 1.5 ms for high and low temperature mixtures, respectively, which significantly increases the heat release rate but rate is similar for both mixtures. To better distinguish the two temperature cases, the cumulative integrated heat release per unit mass (Figure 4.10) showed relatively faster rate for high temperature case initially but after 2.0 ms lower temperature case

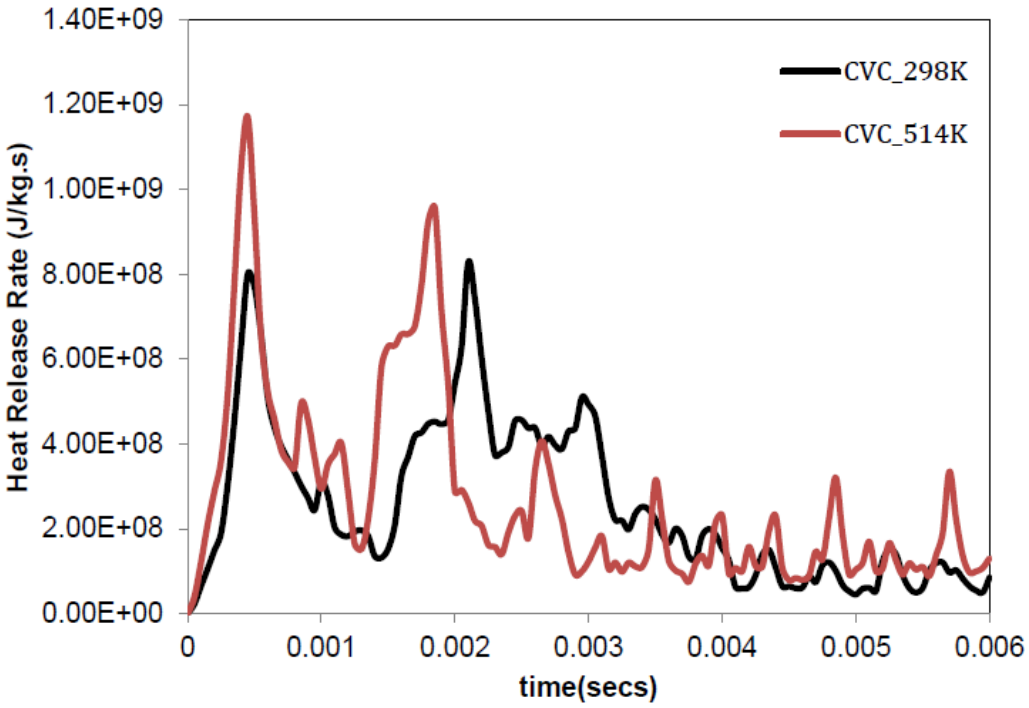

Figure 4.9. Heat release rate variation in main chamber with inclusion of jet radical species [2]

showed faster rate, crossed the high temperature case around 3.1 ms. It is expected that eventually both cases release the same amount of energy after a long period of time, as the amount specific energy is the same. The fact that the cumulative heat release for the lower temperature start actually surpasses that for the higher temperature start is not easy to explain, but may be related to the spatially density variation (Figure 4.11). There it appears that from 2.0 ms to 3.0 ms the lower temperature case has higher flame front area. With a higher density ratio between the burned and unburned regions, the lower initial temperature may also result in strong vorticity deposition. This could cause faster heat release rate for the low temperature case from 2.3 ms to 3.2 ms in Figure 4.10.

Examination of vorticity distribution for the two temperature cases (Figure 4.14) did not quantitatively support or disprove this hypothesis, as the picture is very complex. However, it does reveal that the high vorticity region due to the jet shear is

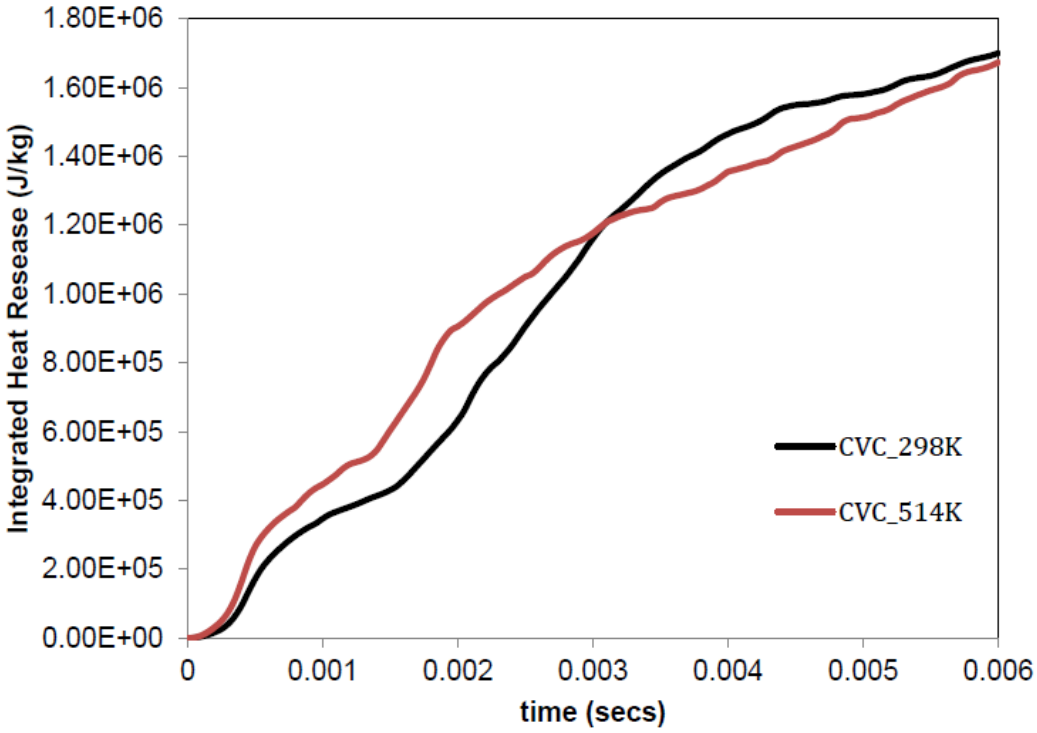

Figure 4.10. Integrated heat release in main chamber with inclusion of jet radical species [2]

distinct from that due to shock-flame interaction, highlighting the need to understand the fluid dynamics of these processes as separate but interlinked phenomena. The effects of cumulative vorticity deposited on flame surface on flame surface area are explained later from detailed 3D simulations.

Overall, the inclusion of active radicals in the pre-chamber jet increases the reaction rate in the chemical kinetics. Simulation with stable species (Figure 4.7 and Figure 4.8) reveals a definite initial lag before heat release in the CVC chamber. Active radicals (Figure 4.9 and Figure 4.10) started the heat release without much delay for chemical kinetics. Further, with only stable jet species, the cumulative heat release (Figure 4.8) is more dependent on initial mixture temperature. With active radicals (Figure 4.10), the cumulative heat release is initially greater for high temperature up to 3.1 ms, but overall, the heat release is not as dependent on initial temperature.

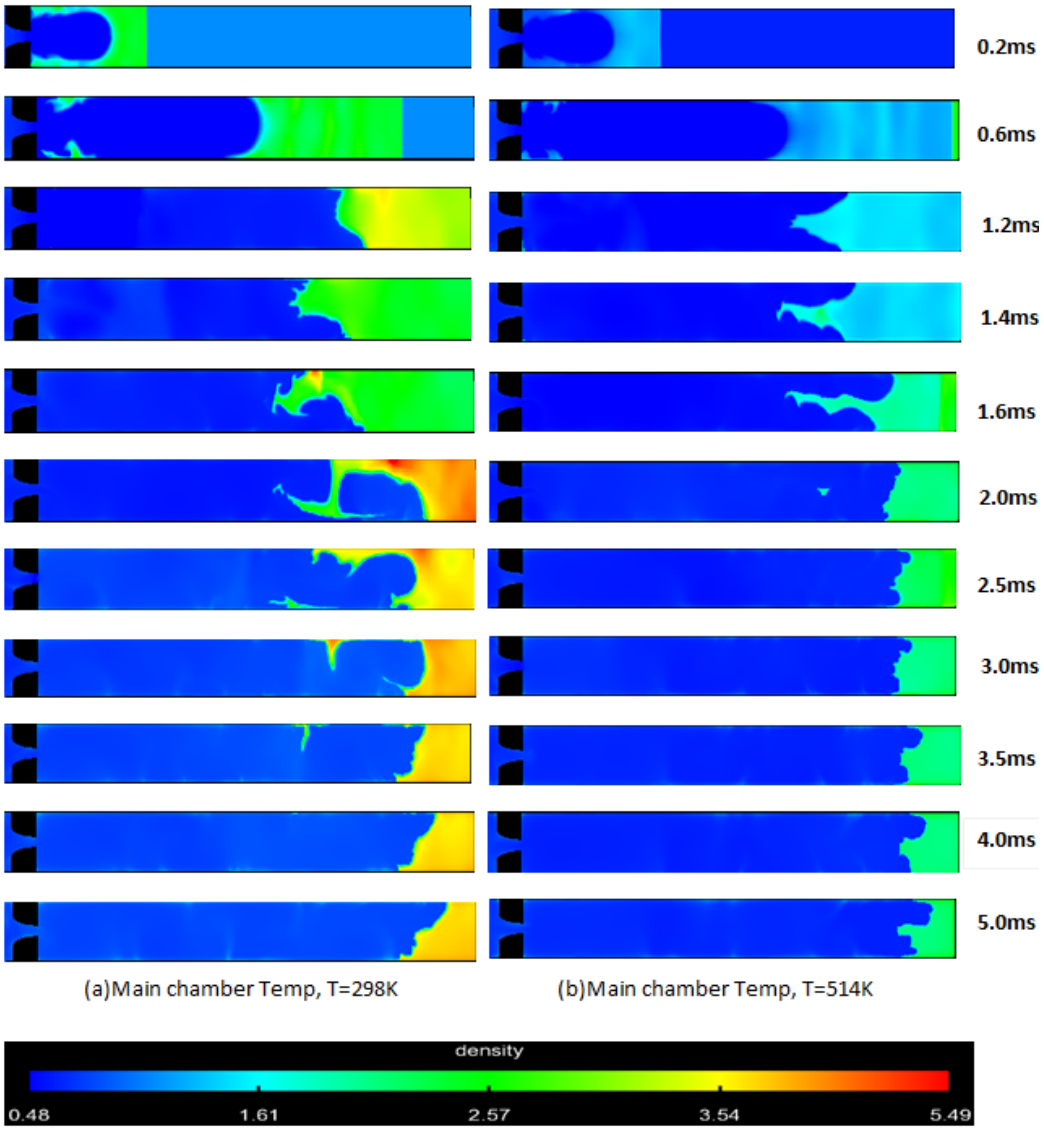

Figure 4.11. History of density (kg/m^3) levels in CVC chamber with inclusion of jet radical species [2]

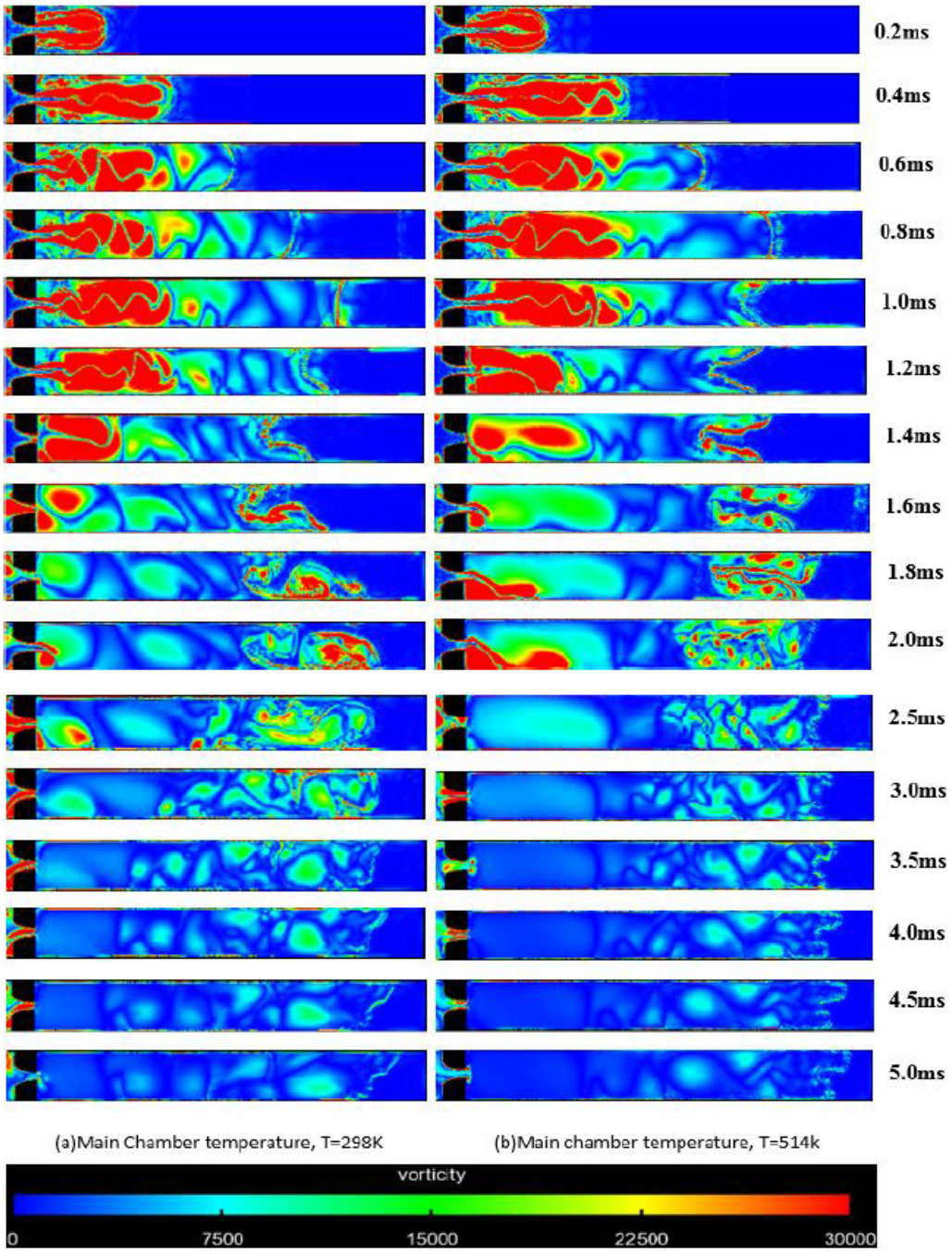

Figure 4.12. Vorticity (1/s) history in CVC chamber with inclusion of jet radical species [2].

5. 3D NUMERICAL INVESTIGATION OF JET IGNITION

5.1 Introduction

Ignition and combustion in a constant volume combustor (CVC) with pre-chamber hot jet ignition system is a very complex phenomenon with hot jet mixing with cold CVC chamber fuel-air mixture, creating vortices, jet penetration and entrainment and shock-wave interaction. Higher pre-chamber pressure causes higher jet penetration and higher level of vorticity in CVC chamber which enhances the mixing of hot jet with cold fuel-air mixture. Global parameters that affect ignition may be classified based on their primary effect as physical or thermochemical, based on their primary effect on the ignition process. Physical parameters include jet traverse speed, jet position, jet direction, nozzle geometry, and the jet velocity, all of which influence the resulting vortex structure. Thermo-chemical parameters are pre-chamber density, composition and temperature, CVC chamber density and temperature, composition (fuel) in pre-chamber and composition (fuel) in CVC chamber. A parameter that is experimentally controllable is the pre-chamber pressure, which directly influences both jet velocity and jet density. Thus it is a parameter that has both physical and chemical effects. Five parameters are investigated with respect to their effects on ignition. Pre-chamber pressure (6, 4 and 2 bar), jet traverse speed (2000 rpm (13.11 m/s), 750rpm (4.92 m/s) and 150 rpm (0.98 m/s)), jet position (centered stationary), CVC chamber composition (30%CH_4 + 70%H_2 (Fuel-A) and 50%CH_4 + 50%H_2 (Fuel-B) by volume) and CVC chamber temperature (300 K and 514 K) are those parameters. Effects of these parameters on flame propagation, flame surface area, vorticity generation are also investigated.

For all the cases pre-chamber fuel is combusted products of 50%CH_4 + 50%H_2 with equivalence ratio 1.1. CVC chamber pressure is 1 bar.

5.2 Effects of Pre-chamber Pressure and CVC Chamber Fuel Reactivity

For centered stationary jet, two different fuel compositions at 300K are considered in CVC. Also, three different pre-chamber pressures are considered. Six different cases are considered depending on the pre-chamber pressure and CVC chamber methane-hydrogen fuel blends which are shown in Table 5.1. Initial temperature and composition for pre-chamber were obtained from the equilibrium calculation for combustion of 50%CH_4 + 50%H_2 fuel blends (by volume) for equivalence ratio 1.1 shown in Table 5.2. The calculation used NASA equilibrium code [103] which were verified with the equilibrium calculations using Cantera [72]. CVC chamber initial conditions and fuel-air composition are also listed in Table 5.2. Total amount of fuel in CVC and the percentage of chemical energy coming from different fuels are showed in Table 5.3.

Table 5.1. Case studied depending on pre-chamber pressure and CVC chamber fuel blends

Case Number	Pre-chamber Pressure (bar)	CVC chamber fuel blends (by volume)
5.1	2	Fuel-B, 50:50 CH_4-H_2 blend
5.2	2	Fuel-A, 30:70 CH_4-H_2 blend
5.3	4	Fuel-B, 50:50 CH_4-H_2 blend
5.4	4	Fuel-A, 30:70 CH_4-H_2 blend
5.5	6	Fuel-B, 50:50 CH_4-H_2 blend
5.6	6	Fuel-A, 30:70 CH_4-H_2 blend

The computed history of chamber-integrated heat release (J) and heat release rate (J/secs) in the CVC chamber is presented in Figure 5.1 and 5.2 respectively. For concise description 30:70 CH_4-H_2 blend will be called Fuel-A and 50:50 CH_4-H_2 blend will be called Fuel-B throughout this study.

Table 5.2. Thermodynamic properties and mass fraction

Thermodynamic properties	Pre-chamber	Nozzle-head and nozzle	CVC chamber Fuel-A	CVC chamber Fuel-B
Equivalence ratio	1.1	0	1.0	1.0
Temperature(K)	2670	300	300	300
Y_{N_2}	0.72364	0.77	0.72872	0.73211
Y_{O_2}	0.00260	0.23	0.22144	0.22252
Y_{H_2}	0.00137	0	0.00553	0.01023
Y_{OH}	0.00380	0	0	0
Y_O	0.00026	0	0	0
Y_{H_2O}	0.14883	0	0	0
Y_H	7.86×10^{-5}	0	0	0
Y_{CO_2}	0.08641	0	0	0
Y_{CO}	0.02991	0	0	0
Y_{NO}	0.00310	0	0	0
Y_{CH_4}	0	0	0.04431	0.03514

For Fuel-A cases it is observed (Figure 5.1) that ignition delay decreases with increasing pre-chamber pressure. For Fuel-B (Cases 5.1, 5.3 and 5.5) cases there is clear indication of ignition for lowest pre-chamber pressure (2 bar) but no rapid increase of heat release for higher pre-chamber pressure (4 and 6 bar) is observed up to 3.0 ms. From Figure 5.2 several sudden rise and drop of heat release rate curve is observed for higher pre-chamber pressure (4 and 6 bar) with Fuel-A cases but smoother shape of heat release rate curve is observed for lower pre-chamber pressure (Figure 5.1 and 5.2) cases. This incident happens because of shock-flame interaction which is explained in detail later.

Table 5.3. Mass and energy from H_2 and CH_4 in CVC for Fuel-A and Fuel-B

Energy and Mass	Fuel-A H_2	Fuel-A CH_4	Fuel-B H_2	Fuel-B CH_4
Mass in CVC (kg)	6.66×10^{-6}	2.29×10^{-5}	3.78×10^{-6}	3.03×10^{-5}
LHV (MJ/kg)	120	50	120	50
Individual Energy (LHV*Mass) (J)	799.2	1145	453.6	1515
Total energy in CVC (J)	1944.2		1968.6	
Percentage of total energy(%)	41.1	58.9	23.04	76.96

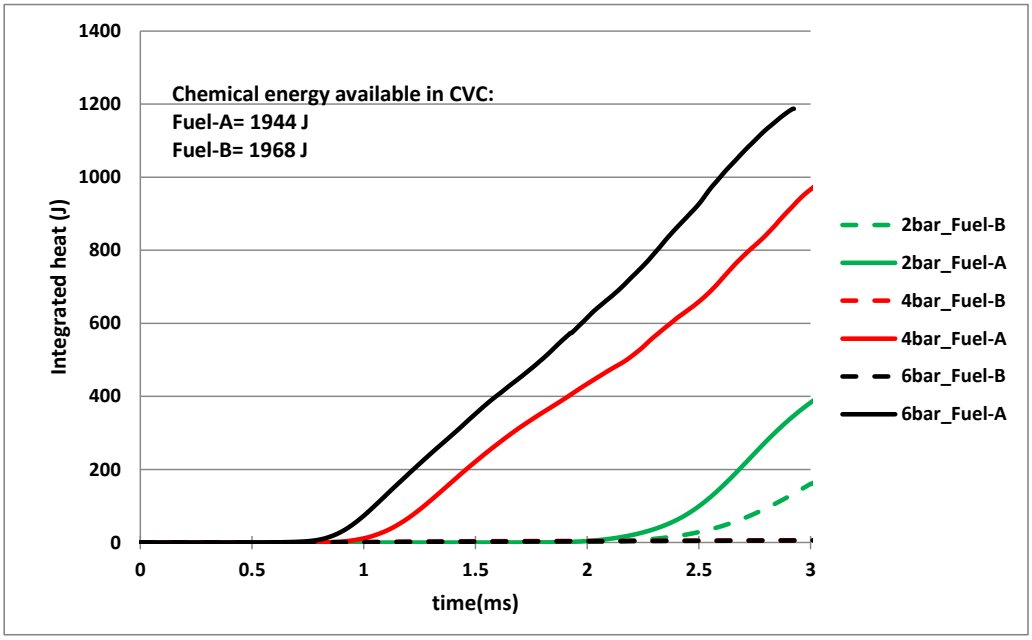

Figure 5.1. Integrated heat release history in CVC chamber for different pre-chamber pressure and fuel blends.

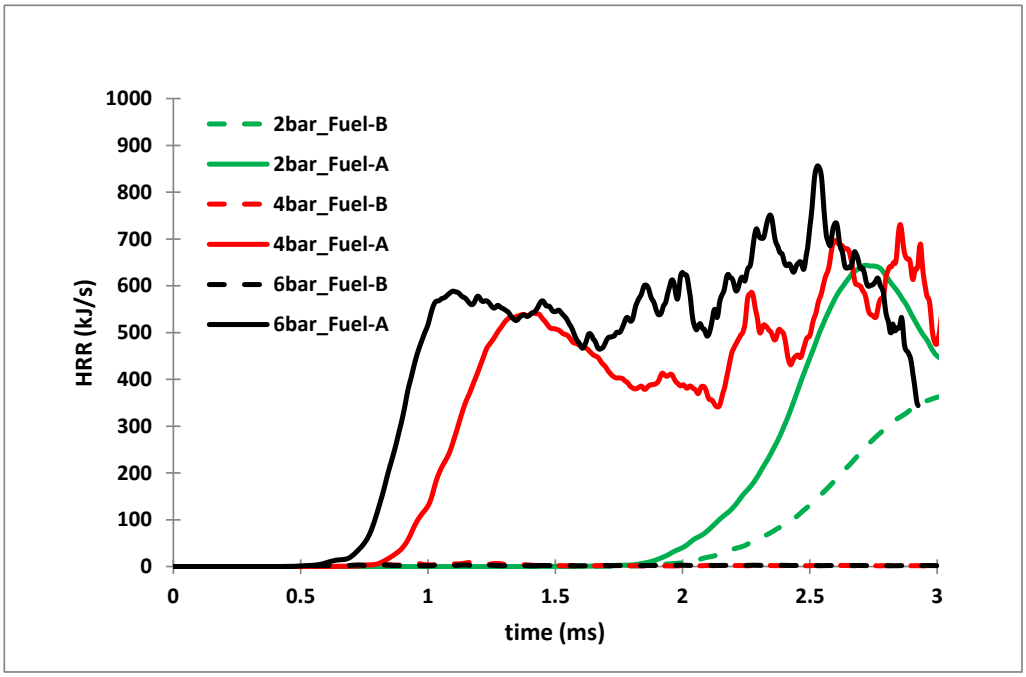

Figure 5.2. Heat release rate variation in CVC chamber for different pre-chamber pressure and fuel blends.

Temperature distribution in CVC chamber for three different pre-chamber pressure is showed for Fuel-A in Figure 5.3 (Cases 5.2, 5.4 and 5.6) and for Fuel-B in Figure 5.4 (Cases 5.1, 5.3 and 5.5). Although all the simulations are in 3D, for better visualization a 2D plane is selected through the center of the nozzle and CVC chamber to show the temperature distribution in nozzle and CVC chamber. As we expected, jet penetration is higher for higher pre-chamber pressure. For Fuel-A cases (Figure 5.3) there is clear indication of ignition just before 1.0 ms for 6 bar, just after 1.0 ms for 4 bar and around 2.2 ms for 2 bar pre-chamber pressure. But for Fuel-B cases (Figure 5.4), there is clear indication of ignition just after 2.2 ms for 2 bar pre-chamber pressure but no sudden increase of temperature is observed for 4 bar and 6 bar pre-chamber pressure. Also from Figure 5.3, distortion of the flame front is located around 1.8 ms for 4 bar and 6 bar pre-chamber pressure. The high speed compressible transient jet from the pre-chamber creates shock in the confined volume,

which interacts with the flame front creating shock flame interaction and deformation of the flame. Distorted flame front increase the flame surface area with time which leads the flame to encompass more fuel-air mixture, increasing the fuel consumption hence the sudden increase of heat release rate.

Damkohler number (Da) is a dimensionless number which is the ratio of mixing time scale and chemical time scale. If in a region mixing time scale is reasonably low compared to chemical time scale (means everything is fully mixed), that is called low Damkohler number region. In the same way, at higher Da, chemical time scale is lower than mixing time scale. Fuel-A has smaller chemical time scale than Fuel-B. Because Fuel-A is relatively more reactive (smaller chemical ignition delay) than Fuel-B. Also with the increase of pre-chamber pressure, mixing time scale decreases. Therefore, for a specific fuel (constant chemical time scale) with the increase of pre-chamber pressure, Da decreases. Which means for a specific fuel, 2 bar pre-chamber pressure has highest Da and 6 bar pre-chamber pressure has lowest Da. Moreover, for a specific pre-chamber pressure (constant mixing time scale) Fuel-A has relatively higher Da compared to Fuel-B (because Fuel-A has smaller chemical time scale). At this point, if the idea of Da is used to understand the ignition behavior qualitatively, it can be said that for more reactive fuel (Fuel-A), jet with higher pressure and speed gives quicker ignition, as Da is large enough (compared to Fuel-B) to sustain ignition kernel. For Fuel-B, jet with lowest pressure and speed is better to ensure ignition because 2 bar case has the highest Da (compared to 4 and 6 bar) and Da is not too small to cause ignition failure.

5.2.1 Turbulent Mixing Effects

To understand the effects of turbulent mixing the inverse of eddy turnover time (ϵ/tke) which is also called mixing rate and heat release rate is plotted for three different pressures in Figure 5.5 and 5.6 for Fuel-A and Fuel-B cases respectively. It appears that, there is an early spike in turbulence generation which is primarily the

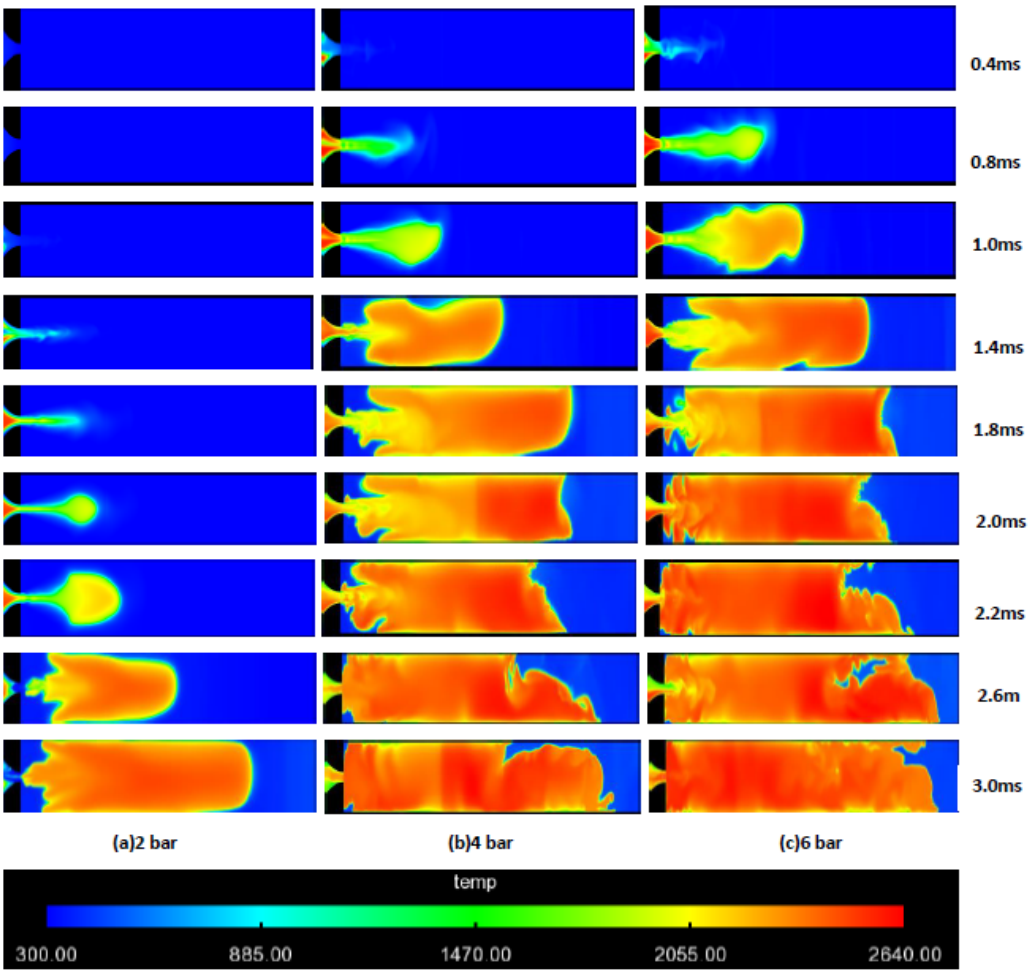

Figure 5.3. History of temperature in CVC chamber for stoichiometric mixture of Fuel-A for pre-chamber pressure (a) 2 bar, (b) 4bar and (c) 6bar.

effect of hot jet injection process. However, it is seen that the turbulence mixing rate does not remain elevated until the end of combustion. In other words, at later stages mixing rate is not enhanced by the reaction. This implies that turbulence from hot jet does not affect the reaction at the later stages of combustion.

There is apparent relation between turbulent mixing and heat release rate. Fuel-A (Figure 5.5) cases has lower chemical ignition delay and higher reactivity (Figure 2.7), where 41.1% of energy is coming from hydrogen in CVC chamber. This rela-

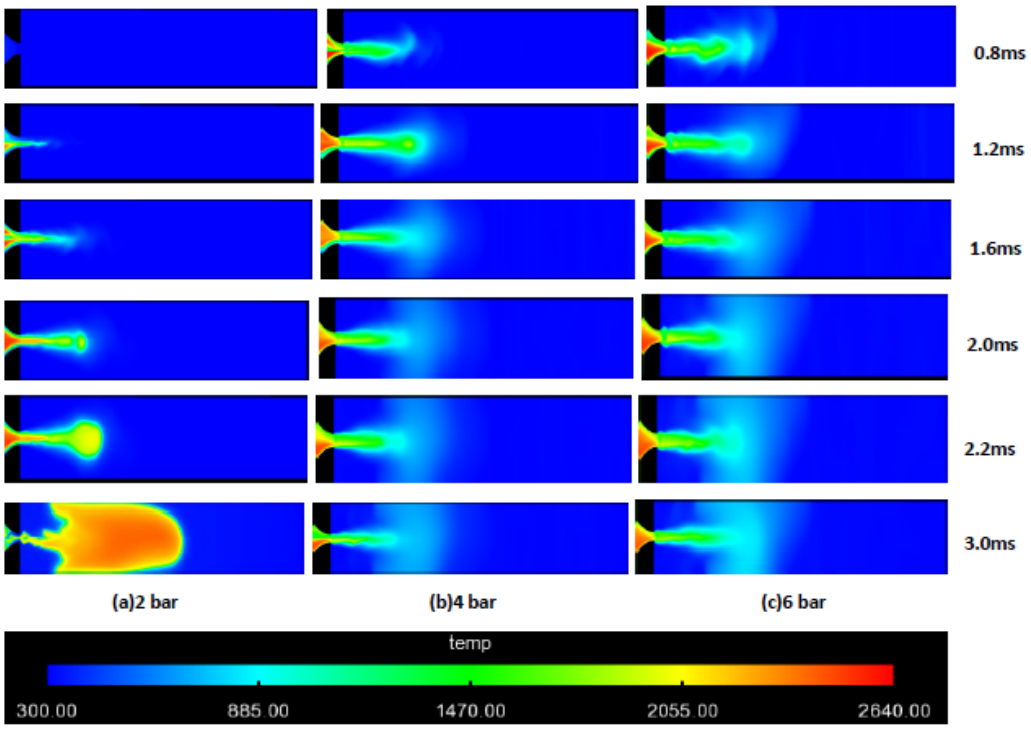

Figure 5.4. History of temperature in CVC chamber for stoichiometric mixture of Fuel-B for pre-chamber pressure (a) 2 bar, (b) 4bar and (c) 6bar.

tively higher reactive fuel composition overcomes the turbulent diffusion and start the ignition within the simulation time frame.

For 6 bar pre-chamber pressure, turbulent mixing is highest and ignition delay is lowest, showing the trend of increasing turbulent mixing-decreasing ignition delay. The difference of turbulent mixing for 6 bar and 4 bar pre-chamber pressure cases are relatively small and from the heat release rate it appears that the ignition delay gap is also relatively small for both cases. This ignition delay gap may be comparable with the turbulent mixing. But there is a comparably bigger difference in turbulent mixing for 6 bar and 2 bar pre-chamber pressure resulting bigger difference in ignition delay. Therefore, it can be said that higher turbulent mixing decreases the ignition delay for comparably high reactive fuel blend. For highly reactive fuel, the chemical delay time is short, and the limiting process is the physical mixing time. Thus turbulence

reduces the physical mixing time, and thus the overall ignition delay. For less reactive fuel, the chemical delay is long, and small differences in physical delay time are not significant. More important then is the effect that entrainment has on temperature and thus chemistry. Also it should be noted that, for higher pre-chamber pressures there is higher induced hot mass to the CVC chamber within the computational time frame. This also can contribute to the shorter ignition delay.

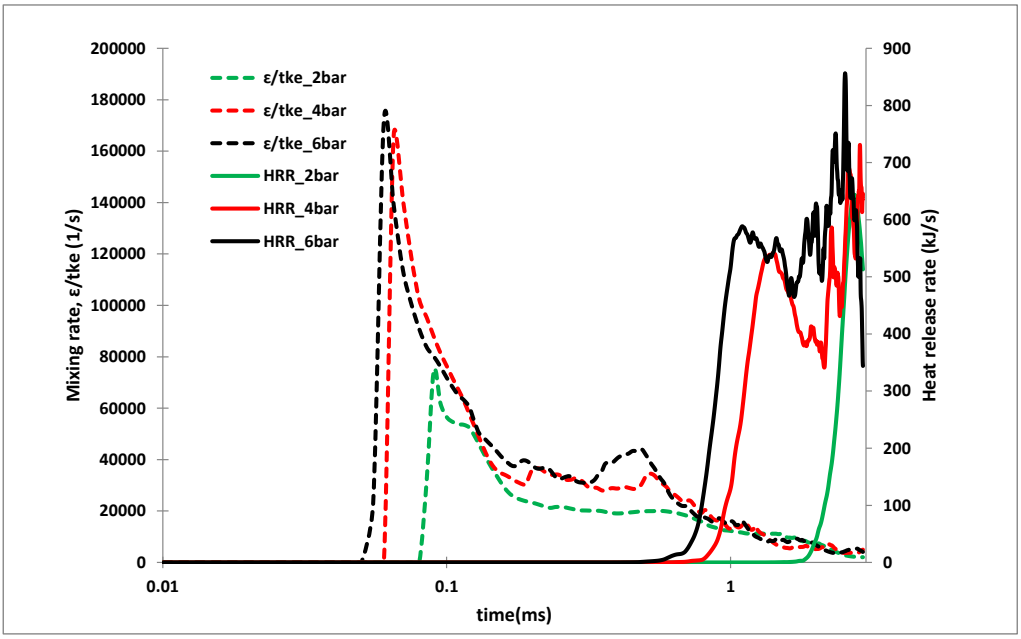

Figure 5.5. Inverse of eddy turnover time (mixing rate) and heat release rate in CVC chamber for Fuel-A cases.

For Fuel-B cases (Figure 5.6) 23.04% of energy is coming from hydrogen, so this is a relatively less reactive fuel blend with higher chemical ignition delay (Figure 2.7). Mixing rate is same as Fuel-A cases (Figure 5.5) but only 2 bar case shows reasonably higher heat release rate or trace of ignition. But if we look closely between 0.05 ms-1.5 ms, there is a relatively smaller amount of increase in heat release rate for 6 and 4 bar cases. This indicates that flame kernel developed at that time and fuels start to react but no rapid increase of heat is developed. Which means, in this case higher mixing rate diffuses the hot mass with relatively cold mass of CVC chamber and

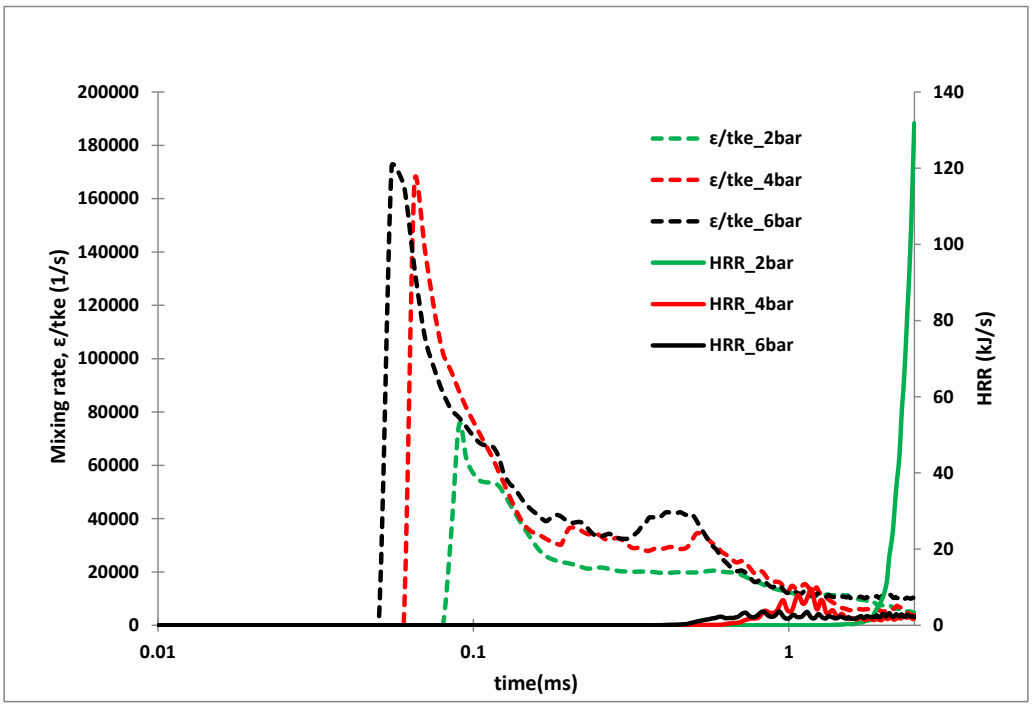

Figure 5.6. Inverse of eddy turnover time (mixing rate) and heat release rate in CVC chamber for Fuel-B cases.

chemical kinetics of Fuel-B is not fast enough to ignite and develop a flame kernel. Ignition is a three dimensional phenomena. It is possible that, at a certain cell, favorable conditions are available to start a flame kernel but if cells adjacent to the flame kernel are unable to provide favorable conditions that kernel will eventually dissipate. May be for this reason, at higher pressure Fuel-B cases are unable to ignite within the simulation time.

5.2.2 Effects of Jet Velocity and Mass Flow Rate

For centered stationary jet, three more cases are considered to compare Mach number, mass flow rate and velocity vector at nozzle and CVC chamber. As combustion affects the thermodynamic properties inside the CVC chamber, three cases are considered with combustion model turned off. It means, hot gas is entering into CVC

chamber through nozzle and mixing with colder CVC chamber gas but no combustion is happening. As a result fluid dynamic properties are unaffected by combustion and are available to compare with cases when combustion happens inside the CVC chamber.

Table 5.4. Case properties with combustion model turned off

Case number	Case condition
5.7	Case 5.2 with combustion model turned off
5.8	Case 5.4 with combustion model turned off
5.9	Case 5.6 with combustion model turned off

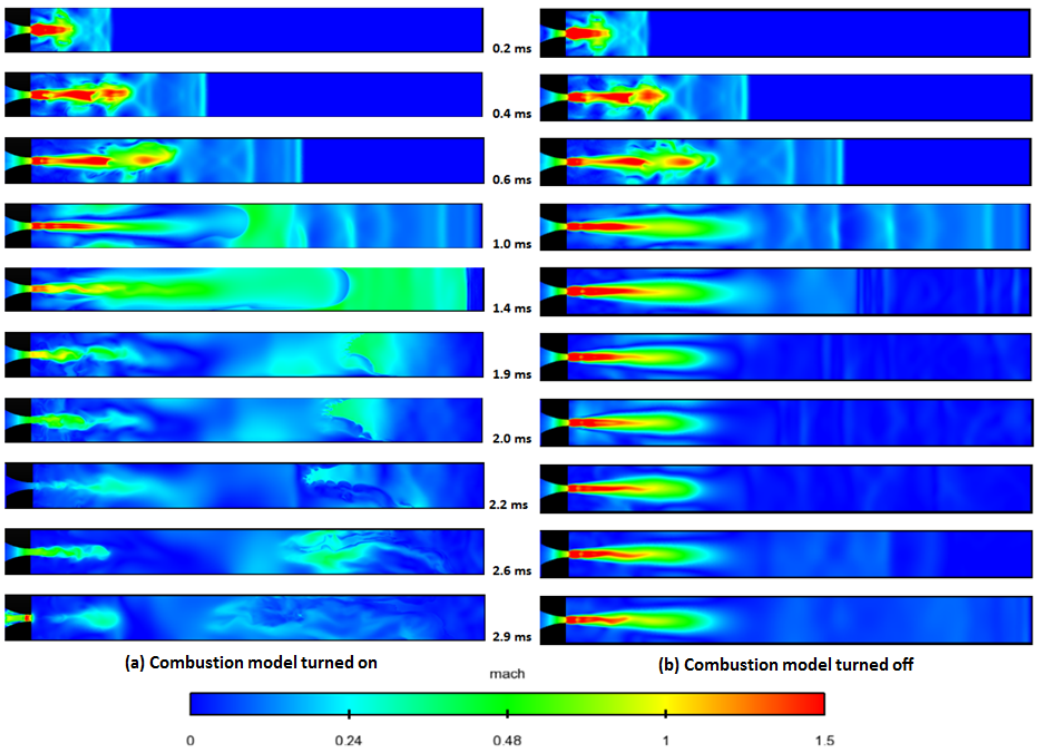

Figure 5.7. Mach number contour plot of centered stationary jet for 6 bar pre-chamber pressure and Fuel-A (a) Combustion model turned on (Case 5.6), (b) Combustion model turned off (Case 5.9).

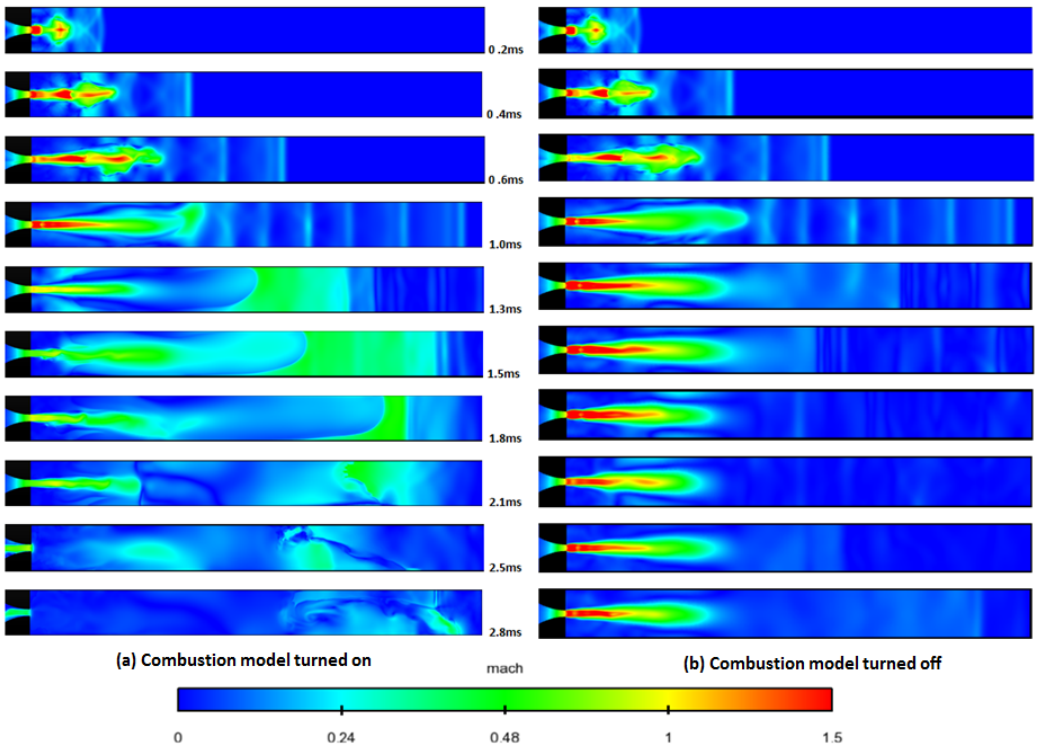

Figure 5.8. Mach number contour plot of centered stationary jet for 4 bar pre-chamber pressure and Fuel-A (a) Combustion model turned on (Case 5.4), (b) Combustion model turned off (Case 5.8).

Through Figures 5.7 to 5.9, Mach number history is plotted at the center plane of CVC chamber for Fuel-A and three different pre-chamber pressures for both combustion model turned on and off. A supersonic jet is called underexpanded when pressure at the nozzle exit is slightly higher than the ambient pressure, overexpanded when nozzle pressure is slightly lower than the ambient pressure and pressure matched if nozzle pressure is equal to ambient pressure. An ideal axisymmetric supersonic jet has some remarkable features [104]. First, the jet periodically expands and contracts to match the ambient pressure. As a result the jet boundary oscillates. The interior of the supersonic jet communicates with the boundary via sound waves, which is slower than supersonic jet flow. The characteristics paths of the sound waves create a very complicated crisscrossed pattern of shock waves, called shock diamonds or Mach discs, which is the second remarkable feature. Jet passes through an intricate and

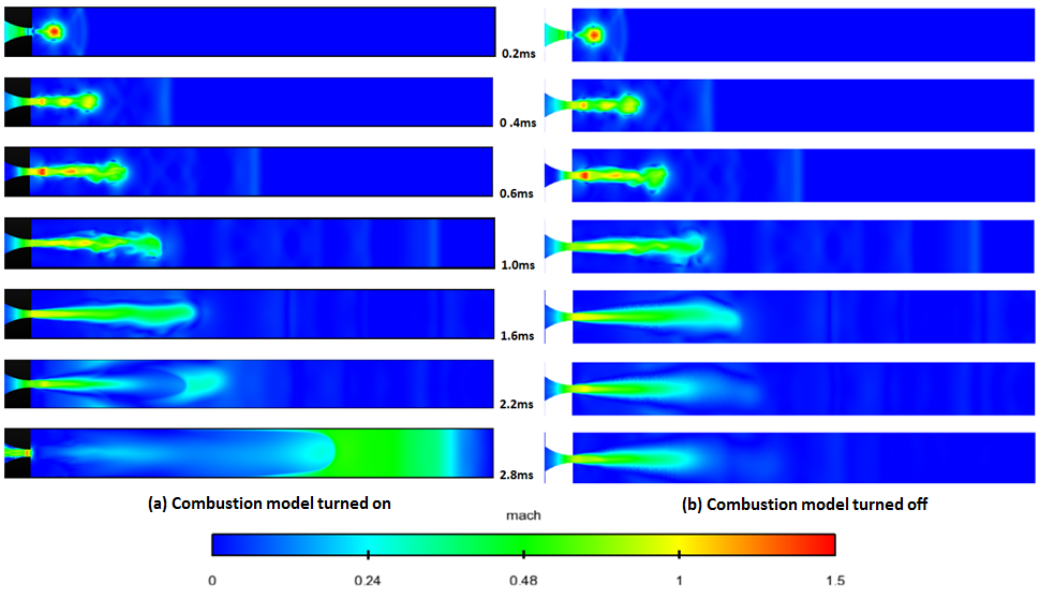

Figure 5.9. Mach number contour plot of centered stationary jet for 2 bar pre-chamber pressure and Fuel-A (a) Combustion model turned on (Case 5.2), (b) Combustion model turned off (Case 5.7).

complicated pattern of rarefaction fans and shock diamonds. When flows through rarefaction fans, jet interior expands and cools. Jet interior compresses and heats up when passes through shock diamonds.

When a flow is underexpanded, the higher gas pressure within the exhaust compared to that of the external atmosphere causes the exhaust to be exploded outward. This expansion decreases the pressure of the exhaust. However, the flow may be expanded too much so that its pressure goes below the atmospheric pressure. As a result, the flow now contracts inwards to increase the lost pressure. Each time the flow passes through one of the compression or expansion processes, the differences between jet interior pressure and ambient pressure decays. This compression and expansion process continues until the exhaust pressure is equal to ambient pressure. In other words, the flow will repeatedly contracts and expands while gradually equalizing the pressure difference between the exhaust and the atmosphere [105].

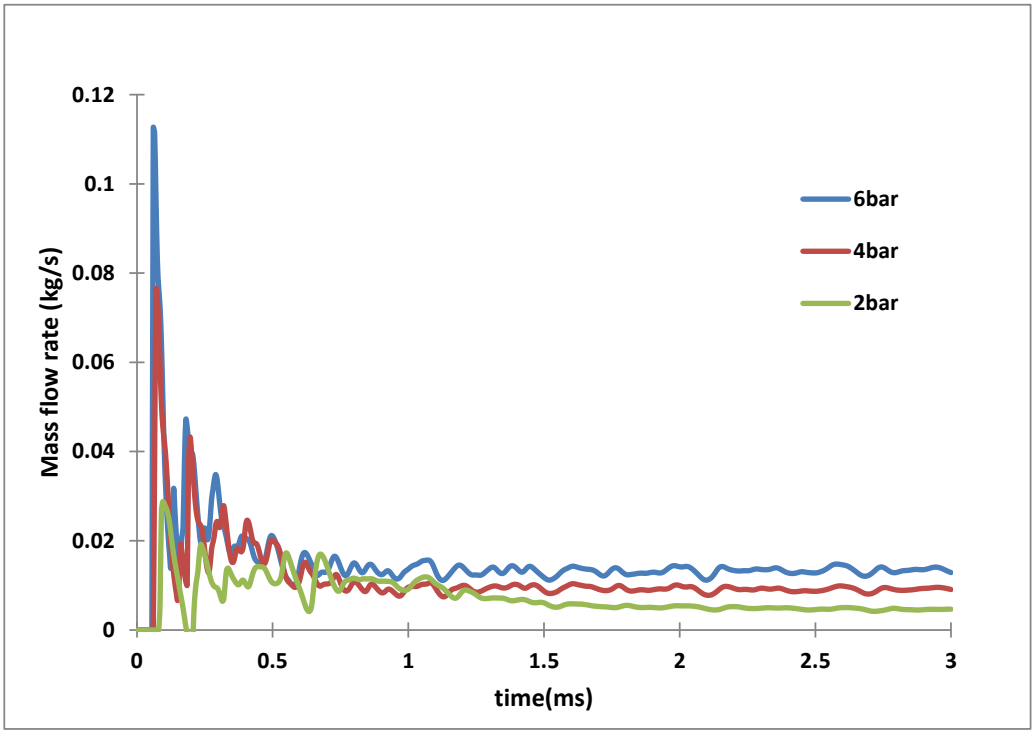

Figure 5.10. Mass flow rate from nozzle to CVC for centered stationary jet with three different pre-chamber pressures (combustion model turned off).

With higher pre-chamber pressure cases (Figures 5.7 and 5.8), there is clear indication of shock diamonds and progress of normal shock waves. For relatively lower pre-chamber pressure (Figure 5.9), shock diamonds are not that clear. Also shock waves are relatively less strong. Coarser grid resolutions and averaged velocity profiles of RANS simulation may be one of the reasons for not getting clear view of the shock diamonds. LES turbulence models are better suited for these kinds of visualizations. Also, beautiful structures of supersonic jets can be found on NASA website for test fire of 7,500 pound-thrust LOX/methane engine [106]. It is also important to note that, for all the cases with combustion model turned off, flow remains choked until simulation end time (3.0 ms). For 6 and 4 bar pre-chamber pressure, Mach number of the core of the jet is much higher (around Ma = 1.5) than 2 bar pre-chamber pressure (around Ma = 1.0). The first shock wave reaches the end wall around 1.0ms. Com-

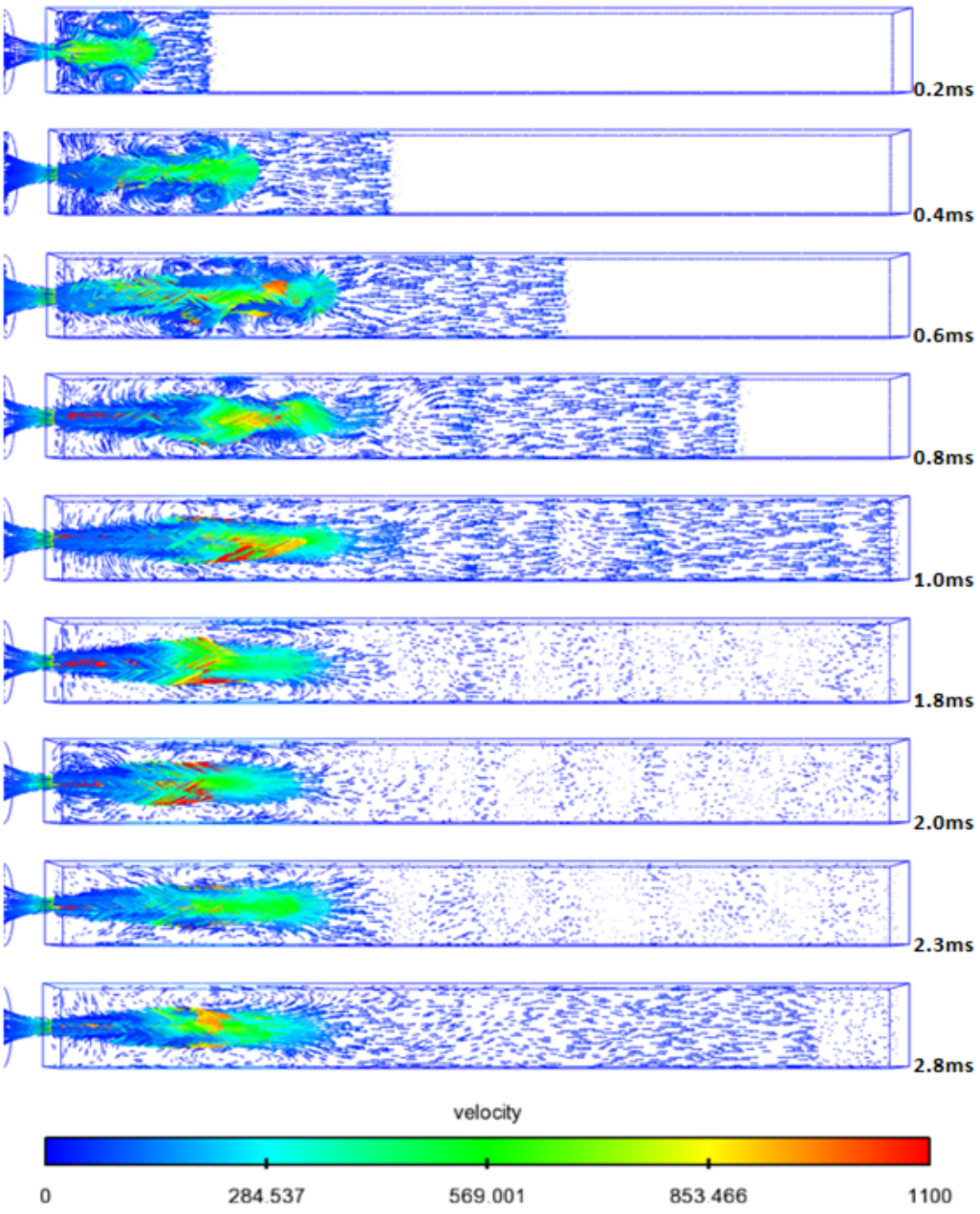

Figure 5.11. Velocity vector contour plot of centered stationary jet for pre-chamber pressure 6 bar, Fuel-A and colored by velocity (m/s) (combustion model turned off, Case 5.9)

bustion increases pressure inside the CVC chamber which disturbs the continuous flow from nozzle (part (a) of Figures 5.7-5.9). Mach number at the nozzle exit goes below 1.0 around 2.0ms, 1.5ms and 2.2ms for Cases 5.6, 5.4 and 5.2 respectively.

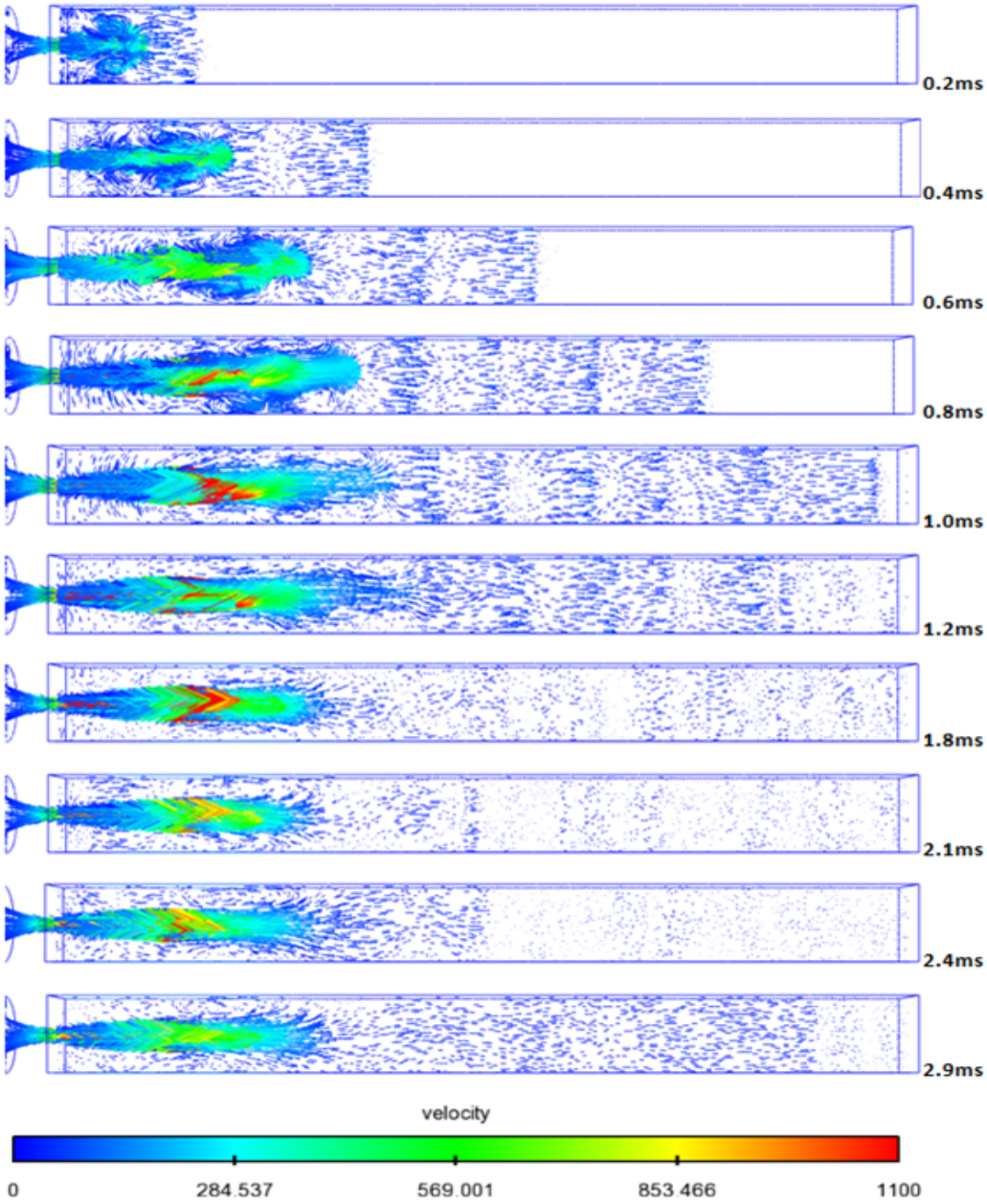

Figure 5.12. Velocity vector contour plot of centered stationary jet for pre-chamber pressure 4 bar, Fuel-A and colored by velocity (m/s) (combustion model turned off, Case 5.8)

Mass flow rate from the nozzle into CVC chamber is a good parameter to compare for which conditions mass flow rate is maximum, as the intention is to supply the maximum amount of hot jet mass in CVC chamber. Figure 5.10 shows the mass flow

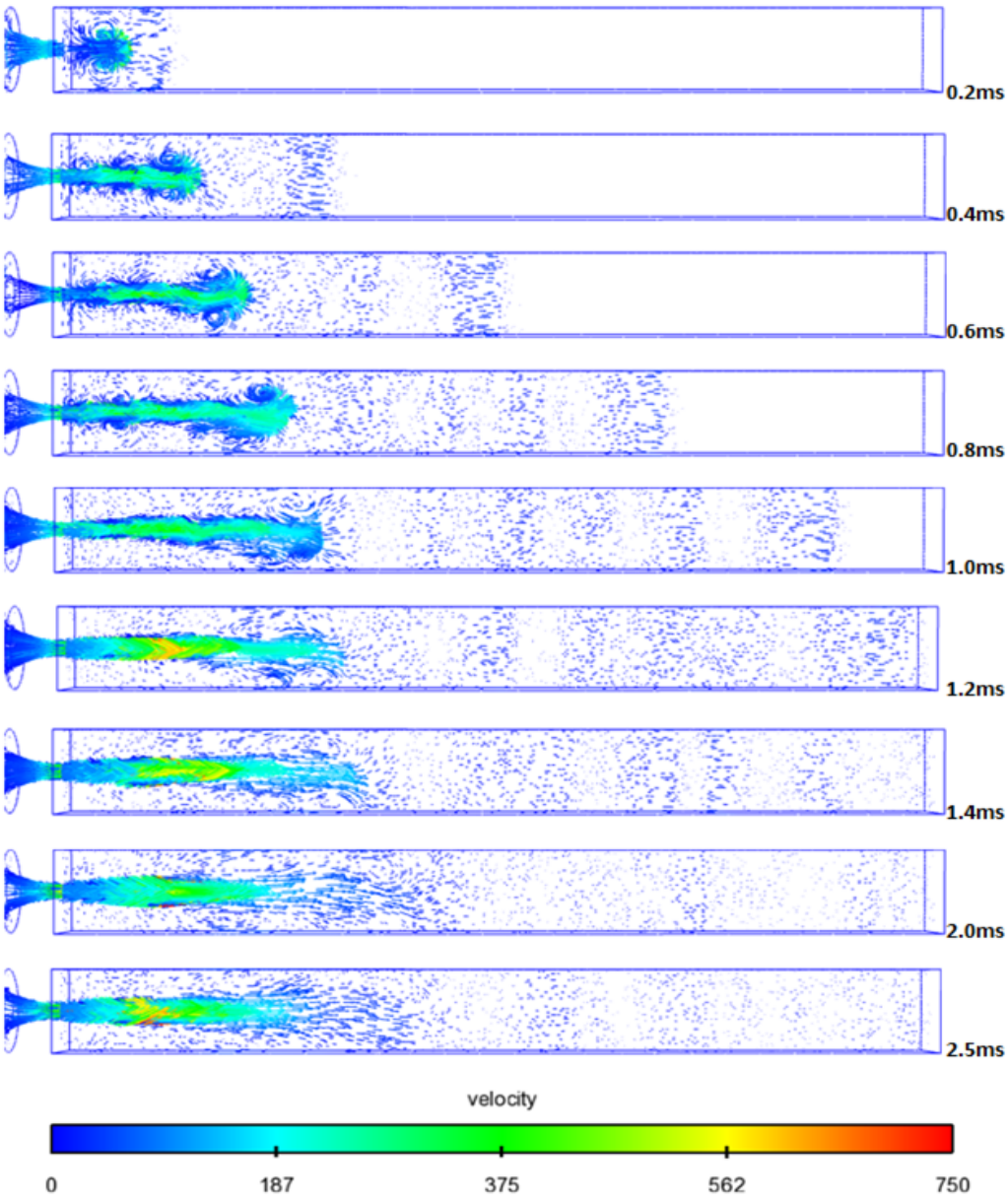

Figure 5.13. Velocity vector contour plot of centered stationary jet for pre-chamber pressure 2 bar, Fuel-A and colored by velocity (m/s) (combustion model turned off, Case 5.7)

rate into CVC chamber for Cases 5.7, 5.8 and 5.9. For 6 and 4 bar pre-chamber pressure, hot jet starts to enter into CVC chamber at the same time but 6 bar case has higher peak value, because the pressure difference is higher which results to

higher thrust. For 2 bar pre-chamber pressure, the maximum mass flow rate is the lowest. Due to underexpansion, there is sudden expansion and contraction of the jet flow which creates shock waves inside the CVC chamber. Sudden pressure rise and drop in CVC chamber affects the mass flow rate from nozzle. Upto 0.6 ms there is fluctuation in mass flow rate for all the cases. But after 0.6 ms when shock diamonds disappears and pressure goes towards equilibrium, fluctuations decreases for all the cases. After 0.8 ms mass flow rate becomes almost constant. Highest mass flow rate is observed for 6 bar pre-chamber pressure and lowest for 2 bar pre-chamber pressure.

Velocity vectors in nozzle and CVC chamber for Cases 5.9, 5.8 and 5.7 are plotted in Figures 5.11, 5.12 and 5.13 respectively. The supersonic hot jet from pre-chamber is entering the CVC chamber through nozzle and mixing with the colder mixture in CVC chamber. Mixing begins at the shear layer of the jet in CVC chamber. Unburned fuel entrainment takes place at the large scale vortices created by the jet. A turbulent jet plume has three distinct structure [107]. First one is zones of intense shear, which is the jet shear layer just outside of the nozzle. Second one is cores of large scale vortices and third is entrainment paths. These structures help the hot jet to mix with the CVC chamber reactants.

The velocity vectors of turbulent hot jets plotted in Figures 5.11 through 5.13 consist of vortices which contain mixture of hot pre-chamber jet and cold CVC chamber reactant. Hot jet plume penetration and shock wave propagation is clearly visualized from the figures. For 6 and 4 bar pre-chamber pressure, the first wave reaches the end wall around 1.0 ms. For 2 bar pressure, shock wave reaches end wall around 1.2 ms. From the fluctuations of velocity vectors, how several shock waves follows the first shock wave is also visible. As expected, for 6 bar pre-chamber pressures, the velocity magnitude is the highest and for 2 bar pressure, is the lowest. The intricate structure of the vortex, generated at the shoulder of the tip of the jet plume is also analyzed. With increasing pre-chamber pressure the vortex size increases. Also several vortices are generated within the short distance of jet tip shoulder and nozzle exit which has countar-rotating direction with respect to each other. Although the figures are in

2D, jet penetration and vortex generation are purely 3D phenomena. High velocity magnitudes are present around the center of the jet plume (yellow and red colors). From their direction it is evident that the jet plume has high swirling and rotating motion like a cyclone.

5.2.3 Flame Surface Area and Shock Flame Interaction

Shock-flame interaction accelerates the initial laminar flame to deflagration to detonation transition, which may create faster combustion in pulsed detonation engine and wave rotor constant volume combustor. When a shock interacts with a flame, due to density gradients baroclinic vorticity generate on the flame surface [108]. Vorticity increase mixing and turbulence which stretches the flame surface and increases the surface area. Increased flame surface also increase the fuel burning rate which yields to increase the heat release rate. Increased heat release rate on propagating flame creates compression waves. These pressure waves compress the unburned fuel in front of the flame, which increase the density and pressure gradient hence increase the burning rate.

Quantification of highly turbulent and deformed flame area is very complicated but helpful to understand the effects of flame area to heat release rate, mixing and vorticity generation. Commercial visualization tool, Ensight [109], is used throughout this study to analyze and calculate very complicated jet flow structures and combustion phenomena. The flame surface area is represented by CH_3 isosurface of value $5e^{-05}$ which is used before in literature [30,92]. Cases 5.6, 5.4 and 5.2 are selected to visualize highly complicated flame propagation characteristics and represented in Figures 5.14, 5.15 and 5.16 respectively. It is also important to note that, there are several other ways to calculate flame surface area. Isosurface plot of selected mass fraction of OH or temperature around 1800 K are some of the effective ways. Each will have a different flame surface area from the others, depending on the selected isosurface quantity. But, the absolute value of flame surface area does not give much insight

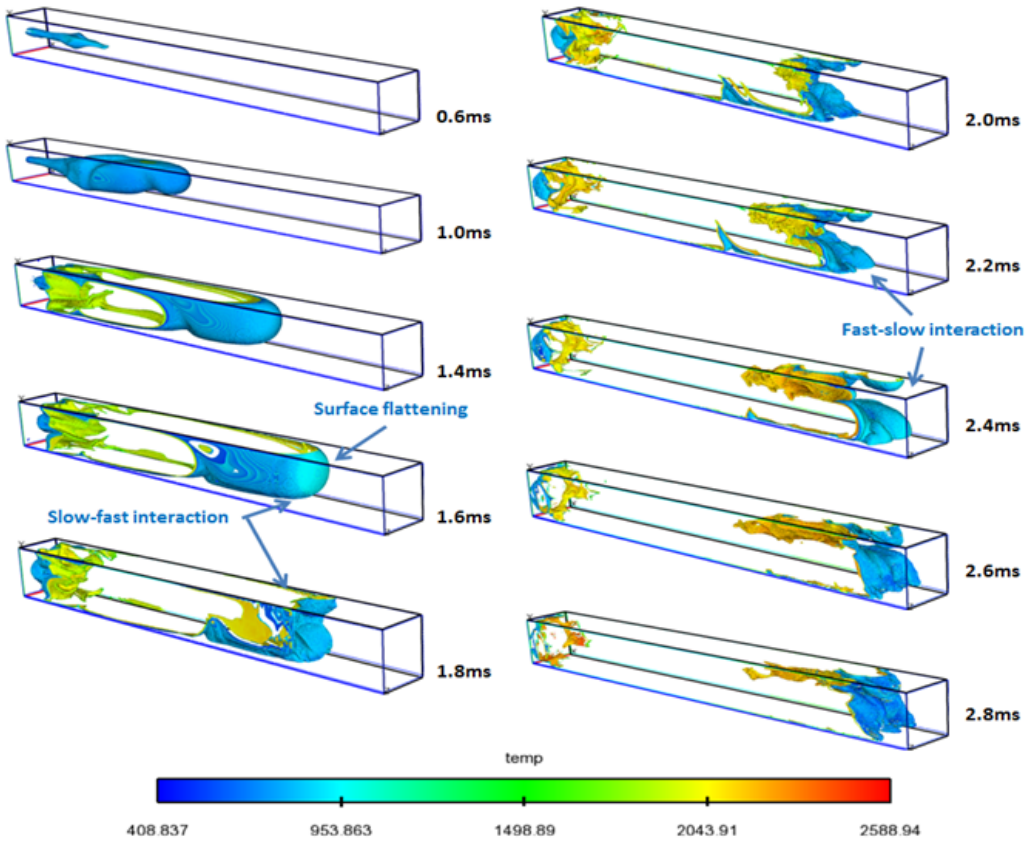

Figure 5.14. Isosurface plot of $Y_{CH_3} = 5e^{-05}$ to visualize flame for centered stationary, Fuel-A , 6 bar pre-chamber pressure jet and colored by temperature (K).

into shock flame interaction problem. How the flame surface area is changing with shock interaction is one of the main focuses of this study.

Due to pressure difference between pre-chamber and CVC chamber, pre-chamber hot jet creates shock in CVC chamber which interacts with the propagating flame. This phenomenon is called Shock Flame Interaction (SFI). There are two stages of SFI. The first one is when shock wave reflects back from the end wall of CVC chamber and interacts with the propagating flame traveling to the opposite direction. The shock is traveling from the unburnt relatively cold reactant (where speed of sound is lower- SLOW) to the hot combusted gas mixture (higher speed of sound- FAST). This is called slow-fast interaction. The second one is when shock reflects back from

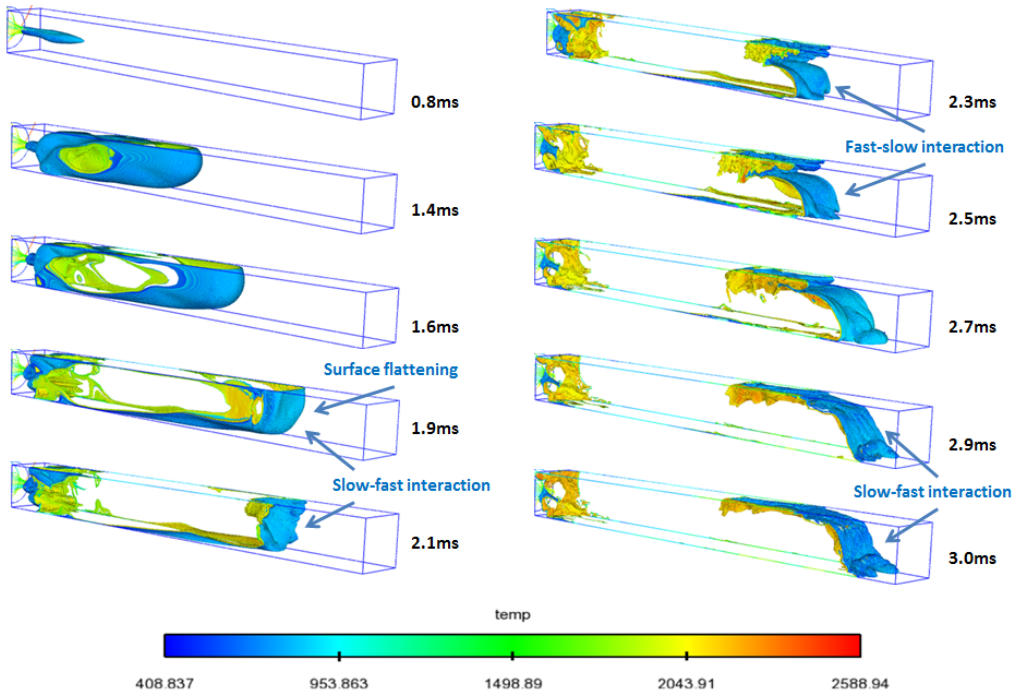

Figure 5.15. Isosurface plot of $Y_{CH_3} = 5e^{-05}$ to visualize flame for centered stationary, Fuel-A , 4 bar pre-chamber pressure jet and colored by temperature (K).

the nozzle end of CVC chamber and interacts the propagating flame traveling to same direction. Shock is traveling from hot combusted gas (higher speed of sound-FAST) to unburnt reactants (lower speed of sound-SLOW). This is called fast-slow interaction.

For 6 bar pre-chamber pressure (Figure 5.14) first slow-fast interaction happens around 1.7 ms and fast-slow interaction happens around 2.2 ms. For 4 bar pre-chamber pressure (Figure 5.15) first slow-fast interaction happens around 1.9 ms and fast-slow interaction happens around 2.3 ms. For 2 bar pre-chamber pressure (Figure 5.16) shock waves are not strong enough to interact and distort the flame surface. As a result, smooth flame surface is visible throughout the simulation time.

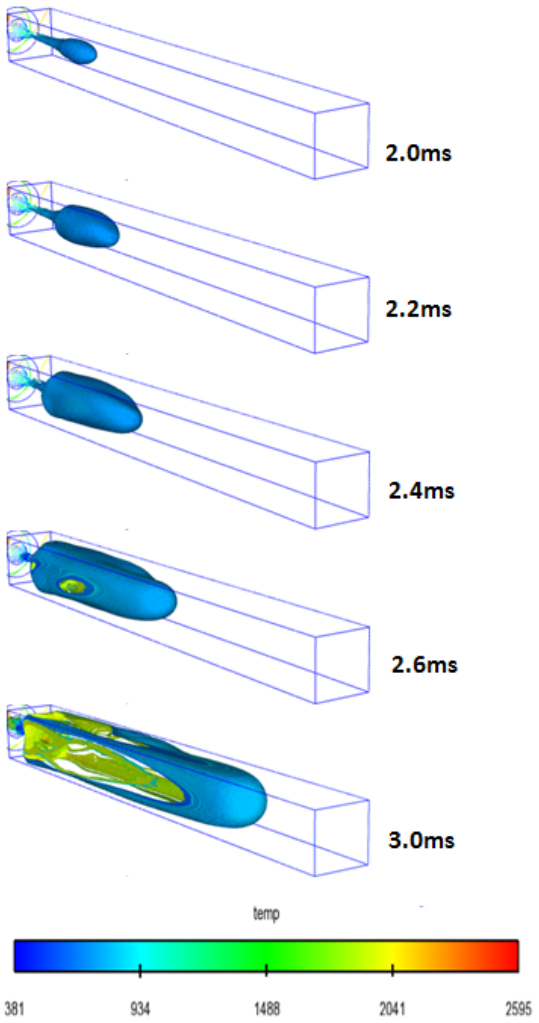

Figure 5.16. Isosurface plot of $Y_{CH_3} = 5e^{-05}$ to visualize flame for centered stationary, Fuel-A , 2 bar pre-chamber pressure jet and colored by temperature (K).

5.2.4 Heat Release Rate and Vorticity Generation Effects on Flame Surface

Two different flame surface areas are selected for further studying which is showed in Figure 5.17. Total flame surface area is the area of Y_{CH_3} isosurface inside the whole CVC chamber. But most of the complicated phenomena of combustion (shock flame interaction, flame surface corrugation etc.) in CVC chamber are happening at leading

part of the flame. As a result, another volume is chosen carefully to calculate Leading flame surface, which is the area of the isosurface within that selected volume. The length of the area (230 mm) is chosen after trial and error to capture most of the SFI. Studying cumulative vorticity generated at a flame surface is an effective way to understand flame wrinkling. Deposited cumulative vorticity at 'total flame surface' is calculated and plotted. Total and leading flame surface area divided by CVC chamber cross sectional area and HRR is plotted with time in Figures 5.18, 5.20 and 5.22 for Cases 5.6, 5.4 and 5.2 respectively. Flame surface area divided by CVC chamber cross sectional area means how much bigger the flame surface area is with respect to channel cross section. Cumulative vorticity and flame surface areas with time are plotted in Figures 5.19, 5.21 and 5.23 for the same cases respectively. Two vertical black lines in each figure is representing the of SFI. The first line is for first SFI (SLOW-FAST) and second line is for second SFI (FAST-SLOW). For 2 bar pressure cases SFI has minimal effect and not indicated in the figures.

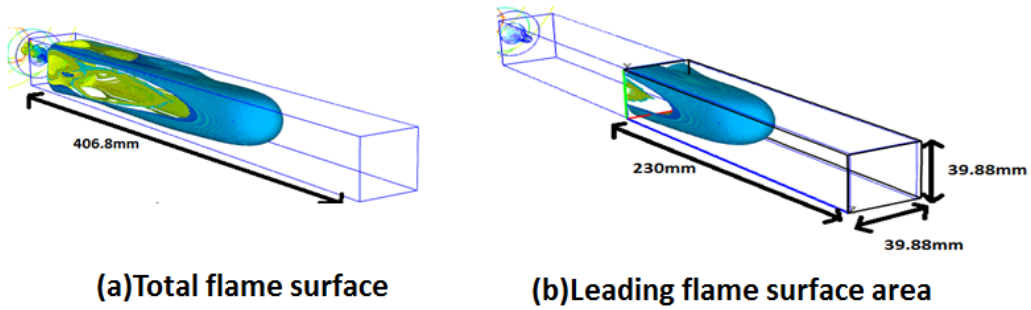

Figure 5.17. Selected volume in CVC chamber to calculate (a) total flame surface area, (b) leading flame surface area.

Total flame surface area and leading flame surface area divided by channel cross sectional area is plotted in Figure 5.18 for 6 bar pre-chamber pressure and their effects on HRR is analyzed. Total flame surface area reaches maximum value which is about 30 times bigger than channel cross sectional area. This higher flame surface area is one of the major advantages of very fast deflagration type combustion over

detonation type combustion. In detonation the flame moves with a speed of sound but the flame front is flat. After the first slow-fast interaction at around 1.6 ms the flame surface area is reduced. For leading flame surface the amount of reduction is about 30% before it starts to increase again. Wijeyakulasuriya and Mitra [92] for a 3D study and Kilchyk et al. [110] for a 2D study also reported a flame surface area reduction immediately after a slow-fast interaction. The leading flame surface reaches maximum value after the fast-slow interaction at around 2.4 ms which is about 18 times bigger than channel cross sectional area. Similar trends are found also for total flame surface but only leading flame surface is analyzed. Because CH_3 isosurface near the nozzle end of CVC chamber is also included in total flame surface area calculation, which is not directly related to SFI and unable to provide useful information.

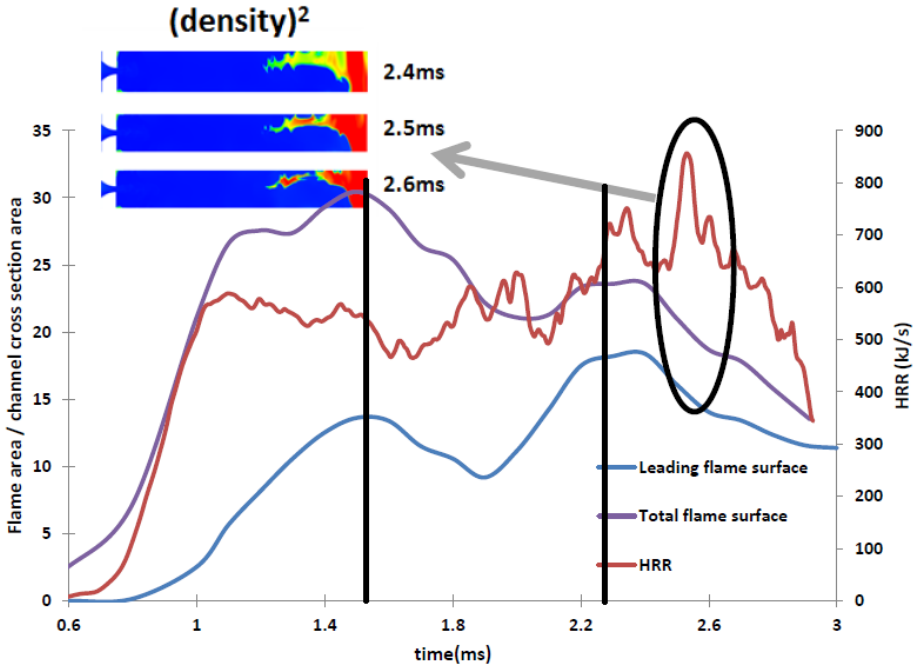

Figure 5.18. Flame surface area and heat release rate for centered stationary, 6 bar pre-chamber pressure, Fuel-A jet. Density square contours are plotted at the top right corner for the same case.

HRR reaches a peak value when leading flame surface reaches maximum at 2.4 ms (Figure 5.18). But there are two notable phenomena to look at. First, the HRR

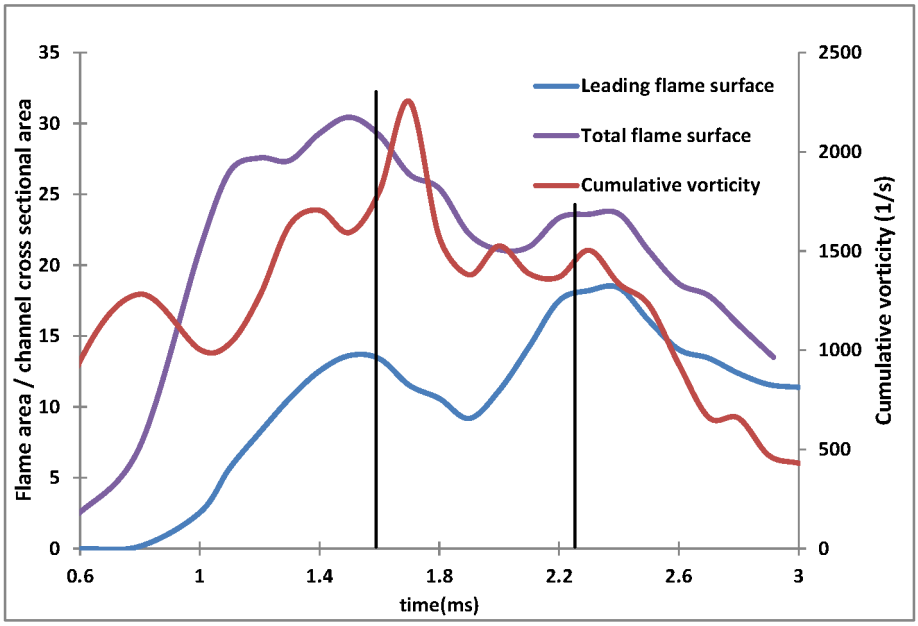

Figure 5.19. Flame surface area and cumulative vorticity generated at total flame surface for centered stationary, 6 bar pre-chamber pressure, Fuel-A jet.

does not decrease at the first SFI when leading flame surface starts to decrease (from 1.6 ms).Second, HRR starts to increase when flame surface start decreasing (at 2.4 ms), suddenly reaches maximum value after 2.5 ms when flame surface is actually still decreasing. One of the explanations could be the enhanced kinetics due to SFI [92]. Shock waves actually increase the gas density of the combustible mixture next to the flame. As a result, although the flame surface area is decreasing but flame is gaining access to more fuel to burn which maintains the HRR. Density square is plotted in Figure 5.18 to gain more insight into this matter. From the density plot it is clear that flame front has access to highly dense combustible gas. Also from Figure 5.1 it is evident that, total amount of chemical energy available in CVC chamber is 1944 J, but after 2.8 ms total chemical heat released is only around 1200 J. About 38% energy is still available inside CVC chamber to burn. From Figure 5.14 we can see that flame roughly covered 85% of the CVC chamber. So the remaining 15% area is

containing around 38% of energy and providing the flame surface with highly dense gas to burn.

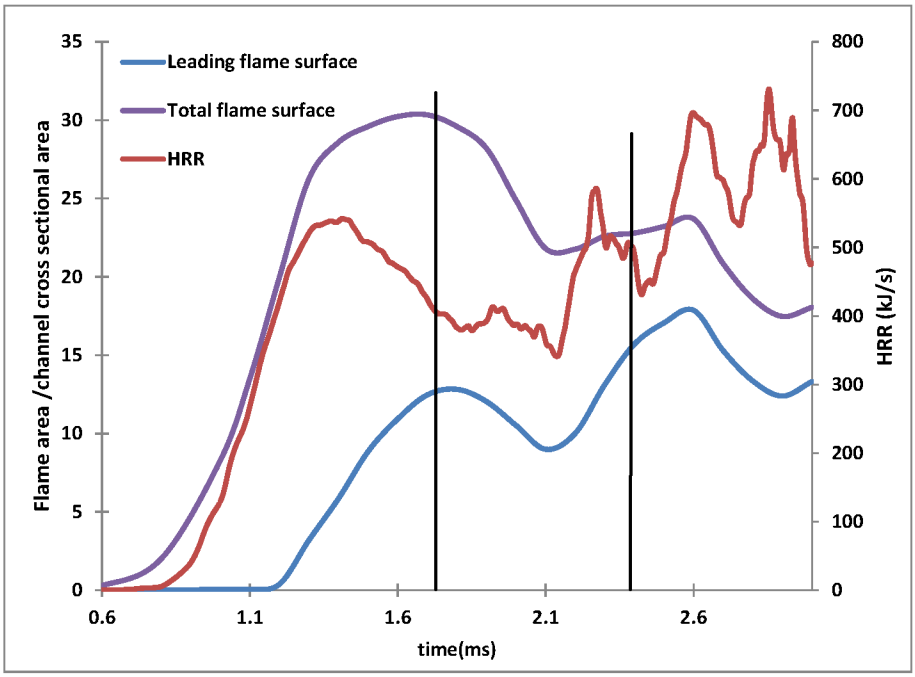

Figure 5.20. Flame surface area and heat release rate for centered stationary, 4 bar pre-chamber pressure, Fuel-A jet.

For 4 bar pre-chamber pressure same trends are observed for flame surface area change and HRR (Figure 5.21). For 2 bar pre-chamber pressure (Figure 5.22) trends are completely different. Only total flame surface is plotted because combustion started later and combusted gas (burned gas) is unable to reach the leading flame surface calculated volume. Also shock wave does not have significant effects on the flame in terms of SFI or flame corrugation. As a result, in Figure 5.22 a linear relation is observed between HRR and total flame surface. Total flame surface area starts to decrease after 2.7 ms. This is because, CH_3 isosurface starts to disappear from the side portion of the total isosurface area (Figure 5.16). HRR also starts to decrease around that time.

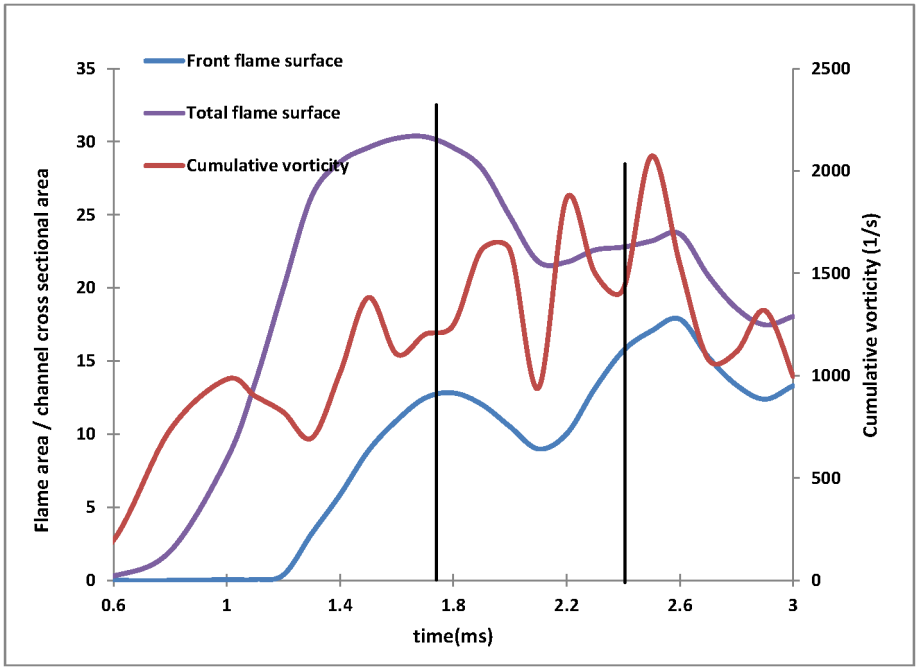

Figure 5.21. Flame surface area and cumulative vorticity generated at total flame surface for centered stationary, 4 bar pre-chamber pressure, Fuel-A jet.

It can be concluded that, Shock wave interaction with the flame can quickly increase flame surface area when the pre-chamber pressure is large, especially on its second pass coming from the hot side. However, even with lower pre-chamber pressure, there is eventual increase in flame surface area and corresponding increase in heat release rate.

During the shock flame interaction, shock waves pass through gases which has different densities. Hot combusted gas has lower density and unburned reactant has higher density. Baroclinic vorticity produces when a shock wave passes through a region with non-uniform density. The strength of this vorticity produced depends on pressure gradient, density gradient and the angle between the gradient of pressure and density. The flame surface increases due to the strain which is generated by the vorticity. How cumulative deposited vorticity on flame surface changes with SFI is to be studied.

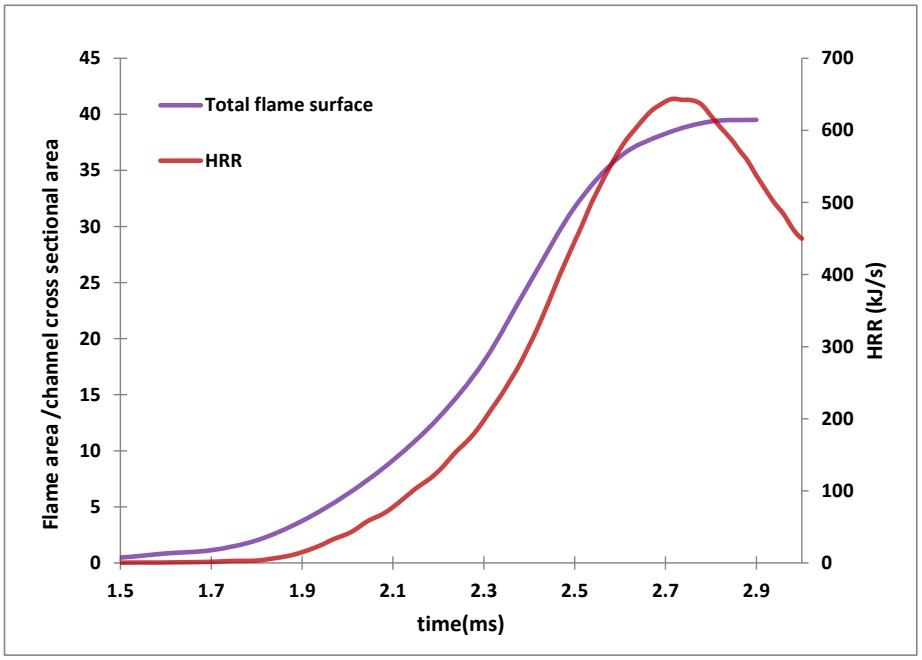

Figure 5.22. Flame surface area and heat release rate for centered stationary, 2 bar pre-chamber pressure, Fuel-A jet.

For 6 bar pre-chamber pressure (Figure 5.19), vorticity starts to increase around 1.0 ms when the total flame surface starts to increase. Vorticity reaches the maximum value just after the slow-fast interaction (at 1.7 ms). Vortex sheets produced at flame surface from baroclinic vorticity, increases mixing between the burned and unburned gas. This could be one of the explanations for why HRR does not drop when flame surface area decreased. Also, fast-slow interaction (at 2.2 ms) does not have the same effect of slow-fast interaction in terms of production of vorticity. For 4 bar pre-chamber pressure (Figure 5.21), cumulative vorticity reaches a peak value just after slow-fast interaction at 1.9 ms. Then decreases with decreasing flame surface area. It reaches the maximum value after the fast slow interaction at around 2.5 ms. For 2 bar pre-chamber pressure (Figure 5.23) flame surface area starts to increase around 2.1 ms and cumulative vorticity starts to increase around 2.5 ms. As SFI does not play any role here, almost linear relation is observed between cumulative vorticity and

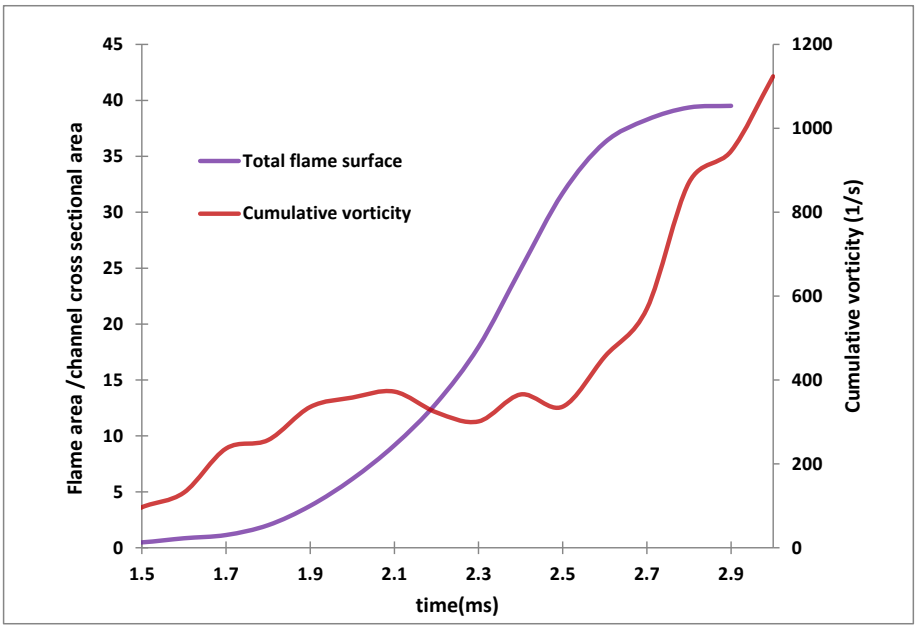

Figure 5.23. Flame surface area and cumulative vorticity generated at total flame surface for centered stationary, 2 bar pre-chamber pressure, Fuel-A jet.

total flame surface area. From the discussion above it is evident that, SFI increases the amount of deposited vorticity on flame surface area.

5.3 Effects of CVC Chamber Initial Temperature

Simulations are performed for a higher initial temperature (514 K) of the methane-hydrogen mixture in the CVC chamber, for the case of a stationary jet issuing from the pre-chamber. Six new cases are considered for studying. All the case numbers and parameters are listed in Table 5.5. The elevated temperature corresponds approximately to the combustor inlet temperature for a gas turbine with a compressor pressure ratio of about 10. For a fixed CVC chamber volume and pressure, the density of the high-temperature mixture will be lower and the total mass of the mixture inside CVC chamber is lower. Total mass and energy available in CVC chamber is listed in Table 5.6.

Table 5.5. Case conditions for 514K CVC temperature

Case number	Case condition
5.10	Case 5.1 with 514K CVC chamber temperature instead of 300K
5.11	Case 5.2 with 514K CVC chamber temperature instead of 300K
5.12	Case 5.3 with 514K CVC chamber temperature instead of 300K
5.13	Case 5.4 with 514K CVC chamber temperature instead of 300K
5.14	Case 5.5 with 514K CVC chamber temperature instead of 300K
5.15	Case 5.6 with 514K CVC chamber temperature instead of 300K

Table 5.6. Total mass and amount of energy from H_2 and CH_4 in CVC for Fuel-A and Fuel-B with 514 K CVC temperature

Energy and Mass	Fuel-A H_2	Fuel-A CH_4	Fuel-B H_2	Fuel-B CH_4
Mass in CVC (kg)	3.87×10^{-06}	1.33×10^{-05}	2.21×10^{-06}	1.76×10^{-05}
LHV (MJ/kg)	120.8	49.6	120.8	49.6
Individual Energy (LHV*Mass) (J)	467.5	661	266.5	875
Total energy in CVC (J)	1128.5		1141.5	
Percentage of total energy("%")	41.4	58.6	23.3	76.7

Normalized integrated heat release and heat release rate is plotted with time for cases 5.1, 5.3, 5.5, 5.10, 5.12 and 5.14 in Figures 5.24 and 5.25 respectively. To make appropriate comparisons, the predicted integrated heat release and HRR is normalized using its corresponding mixture mass in the CVC chamber.

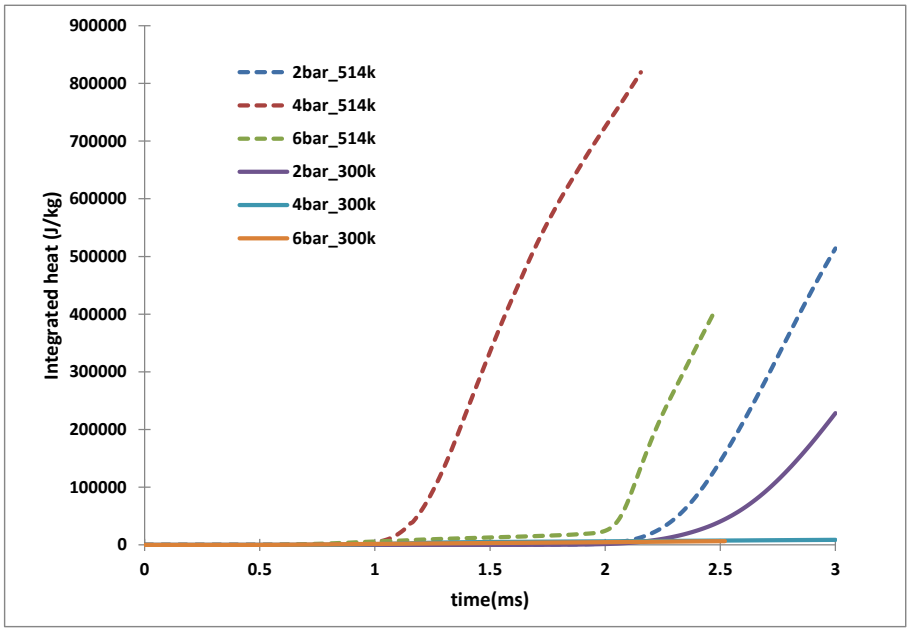

Figure 5.24. Comparison of integrated heat release in CVC chamber normalized by mass for centered stationary, Fuel-B, 514 K and 300 K CVC chamber temperature with different pre-chamber pressure.

For 4 bar and 6 bar pre-chamber pressure ignition does not occur for Fuel-B and 300 K CVC chamber temperature within the simulation run time. For 514 K CVC temperature, ignition starts just after 1.0 ms for 4 bar pre-chamber pressure. For 6 bar pre-chamber pressure, it seems that reaction starts around 1.0 ms but the integrated heat release curve does not rise until 2.0 ms. For 2 bar pre-chamber pressure, ignition delay is around 2.2 ms for both 300 K and 514 K CVC temperature but a little bit earlier for 514 K CVC temperature. It is interesting to point out that for Fuel-B CVC temperature has significant effect on ignition delay for 4 and 6 bar pre-chamber pressure compared to 2 bar pre-chamber pressure. Also the HRR is higher for all the 514 K CVC temperature cases compared to 300 K CVC temperature, highest for 6 bar pre-chamber pressure. This indicates that at higher initial CVC chamber temperature stronger combustion occurs.

H_2 and CH_4 mass in CVC is plotted with time for Case 5.1, 5.3, 5.5, 5.10, 5.12 and 5.14 in Figures 5.26 and 5.27 respectively. As stated before due to lower density

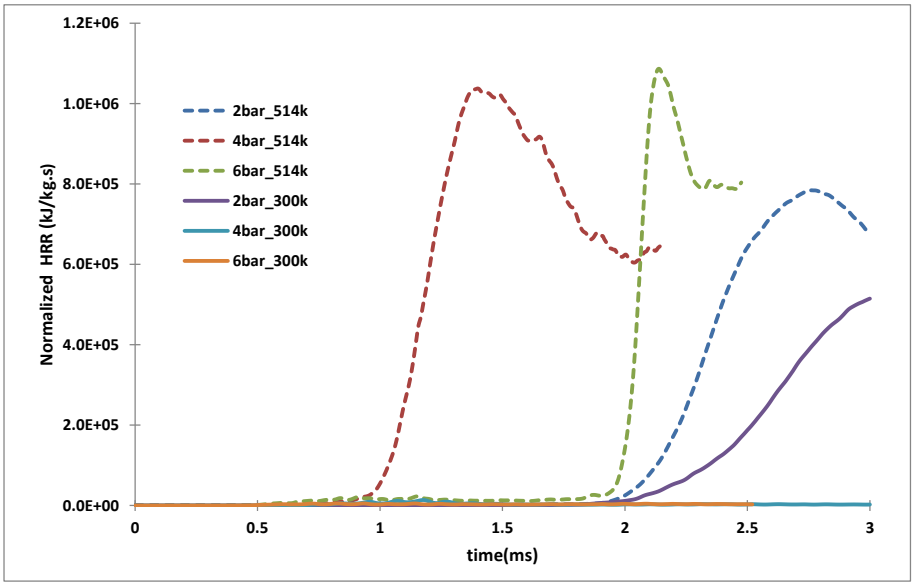

Figure 5.25. Comparison of Heat Release Rate (HRR) in CVC chamber normalized by mass for centered stationary, Fuel-B, 514 K and 300 K CVC chamber temperature with different pre-chamber pressure.

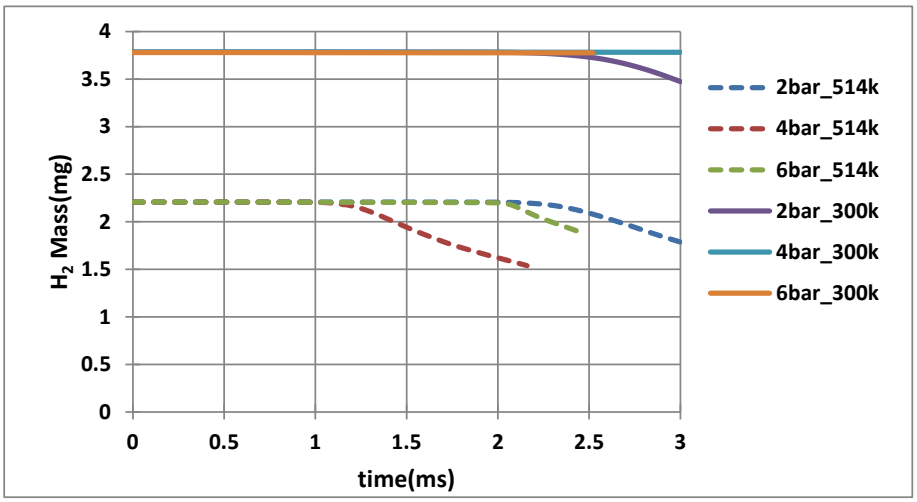

Figure 5.26. Comparison of Hydrogen mass in CVC chamber for centered stationary, Fuel-B, 514 K and 300 K CVC chamber temperature with different pre-chamber pressure.

at higher temperature in CVC chamber, total mass of CH_4 and H_2 is lower for 514 K CVC temperature. CH_4 and H_2 mass remains same for 300 K CVC temperature

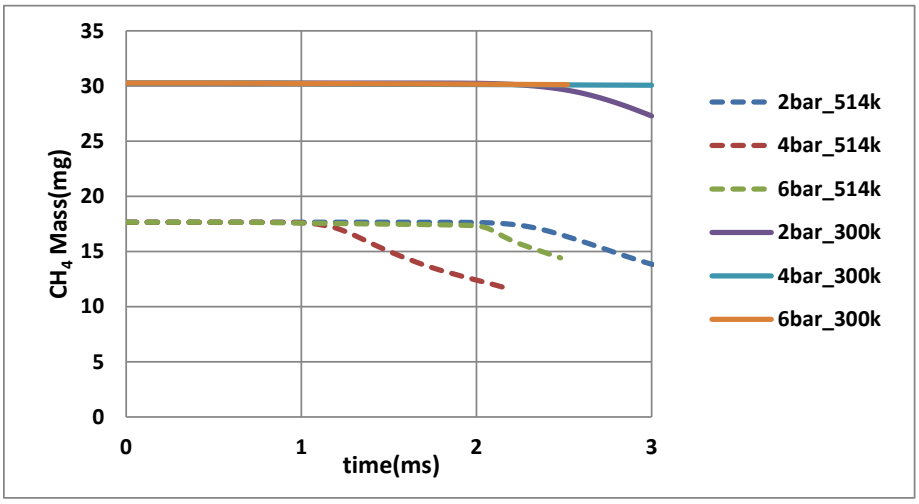

Figure 5.27. Comparison of Methane mass in CVC chamber for centered stationary, Fuel-B, 514 K and 300 K CVC chamber temperature with different pre-chamber pressure.

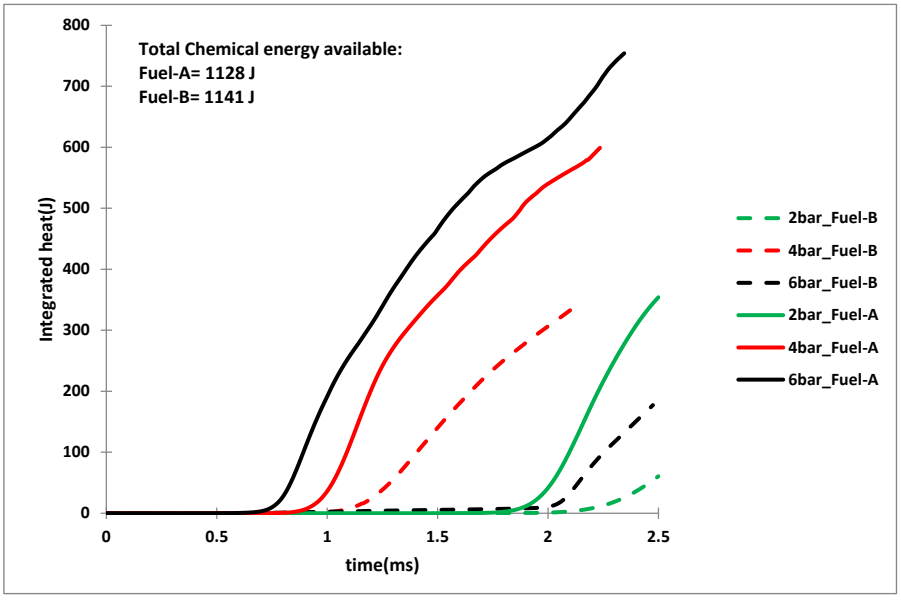

Figure 5.28. Comparison of Integrated heat release in CVC chamber for centered stationary, 514 K CVC chamber temperature, Fuel-B and Fuel-A with different pre-chamber pressures.

with 4 and 6 bar pre-chamber pressure, indicates that no chemical reaction starts within the simulation time to start ignition. For all the other cases where ignition occurs, both CH_4 and H_2 start to drop mass at the same time for the same case. The rate of decreasing the mass is also same. This is indicating that, although addition of H_2 helps to ignite the fuel mixture earlier, after the ignition both H_2 and CH_4 help equally to progress the combustion process further. The chain initiating and chain branching reactions of H_2 and CH_4 should be investigated further for better understanding of the ignition and combustion process. Also the intermediate species that H_2 and CH_4 produce should also be looked into.

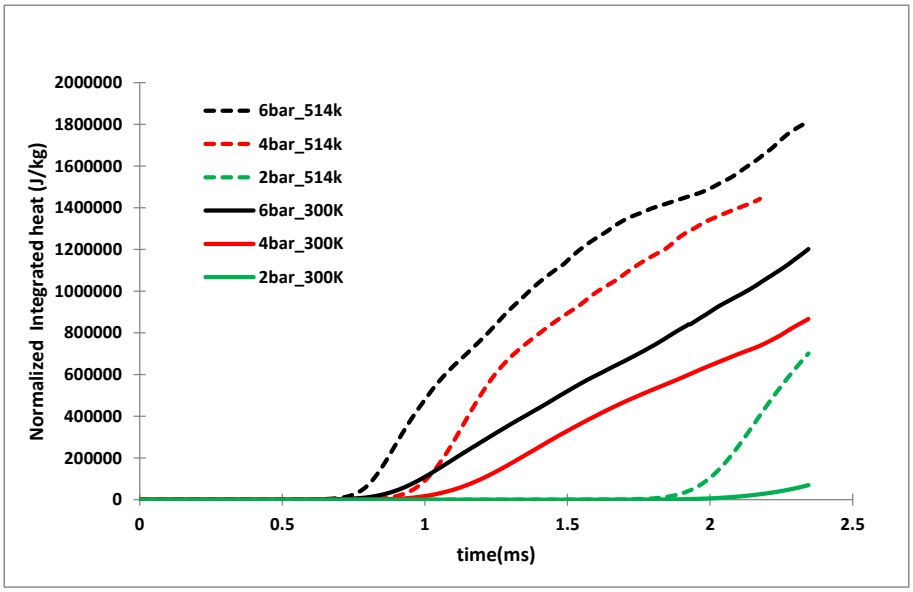

Figure 5.29. Comparison of integrated heat release in CVC chamber normalized by mass for centered stationary, Fuel-A, 514 K and 300 K CVC chamber temperature with different pre-chamber pressures.

Integrated heat release with time in CVC chamber for Cases 5.10 to 5.15 is plotted in Figure 5.28. For Fuel-A lowest ignition delay is observed for 6 bar pre-chamber pressure at 0.7 ms, 4 bar case has an ignition delay around 0.9 ms and 2 bar pressure has the highest 1.8 ms delay. For Fuel-B the lowest ignition delay is 1.1 ms for 4 bar pre-chamber pressure, 6 bar has around 2.1 ms and 2 bar has the highest around

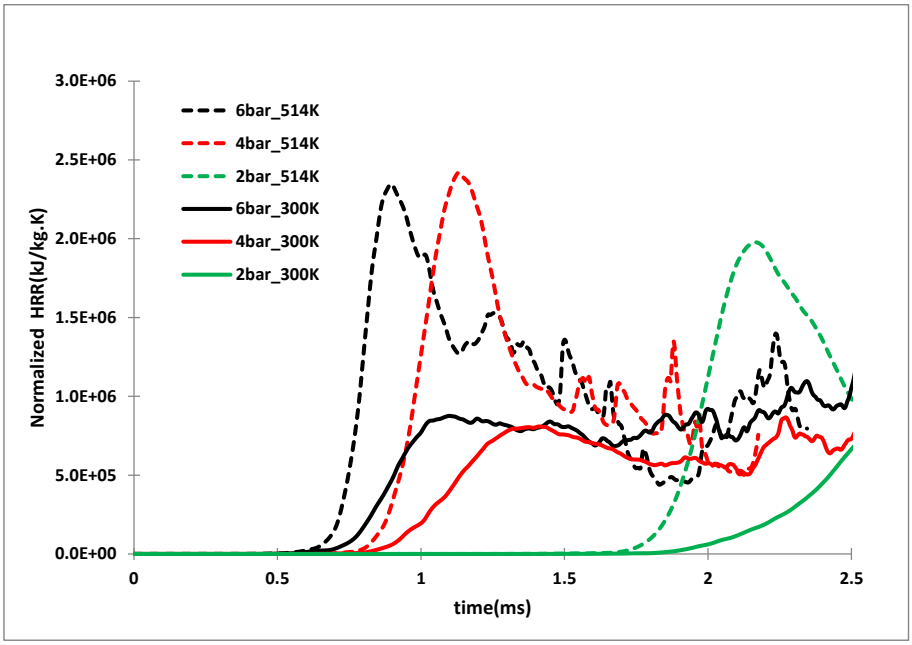

Figure 5.30. Comparison of Heat Release Rate (HRR) in CVC chamber normalized by mass for centered stationary, Fuel-A, 514 K and 300 K CVC chamber temperature with different pre-chamber pressures.

2.3 ms. All the Fuel-A cases have higher slope for integrated heat release curve mean that fuel is burning faster. Also case 5.15 (6 bar pre-chamber pressure, Fuel-A, 514 K CVC temperature) burns almost 67% of the chemical energy available in CVC chamber compared to case 5.6 (6 bar pre-chamber pressure, Fuel-A, 300 K CVC temperature) which only burns 42% of the energy available within the simulation time (2.3 ms). Comparing Figure 5.28 with 5.1 shows how CVC temperature affects and increases the chemical kinetics in CVC chamber for faster ignition and combustion.

Normalized integrated heat release and heat release rate is plotted with time for Cases 5.2, 5.4, 5.6, 5.11, 5.13 and 5.15 in Figure 5.29 and 5.30 respectively. To make appropriate comparisons, the predicted integrated heat and HRR is normalized using its corresponding mixture mass in the CVC chamber. For 514 K CVC chamber temperature, 6 bar pre-chamber pressure case ignited earlier than any other case. Then 4 bar and then 2 bar case ignited. The same trend is also found for 300

K CVC chamber temperature. This indicates that higher pre-chamber pressure is advantageous for Fuel-A. With higher jet penetration and higher mixing rate in CVC chamber, higher pre-chamber pressure helps to ignite faster for a specific or a range of specific fuels. Also the normalized integrated heat release or HRR is higher for higher CVC chamber temperature, which is expected. Higher temperature increases the chemical kinetics, as a result fuels burn faster and results stronger combustion.

5.3.1 Defining The Ignition Delay

The definition of ignition delay could vary depending on the type of ignition. Ignition by a jet of reactive hot gas is a significantly different phenomenon in that there is a significant physical mixing process that must occur before chemical reactions can commence, yet the injected reactive species may remain active while it mixes with relatively cold reactive gas [2]. The ignition delay time for a jet-ignited constant volume combustor (CVC) may be defined as the time from jet initiation to the occurrence of rapid, visible, and pressure-generating heat release in the CVC chamber [33]. Also, ignition could reasonably be defined as, "occurring either at the time of maximum rate of change or at the time when the peak value of some species or variable such as [OH], [CH] or pressure is reached, or could be based on an extrapolation of the maximum slope to the zero signal level" [111]. In general, pressure rise is a good indicator of ignition at high fuel concentrations.

Rapid increase of integrated heat and HRR in CVC chamber are used in this study to define ignition delay. But as stated in literature, rapid generation of active radicals such as [OH] could also be an indicator of ignition delay. As a result, rapid change of [OH] and integrated heat is compared to find out their effects on defining ignition delay.

Cases 5.10 to 5.14 (five cases) are considered for this comparison. To calculate the OH mass fraction, the location where ignition initiates in CVC chamber is pinpointed from post processing tool. A sphere of 8 mm diameter (arbitrarily chosen) is placed at

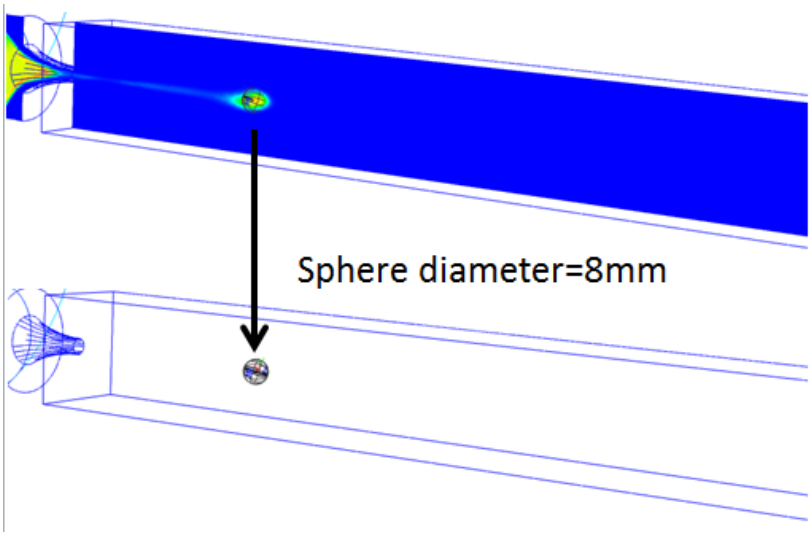

Figure 5.31. Creating a sphere with 8 mm diameter at ignition point in 3D space to calculate temporal OH mass fraction within the sphere domain.

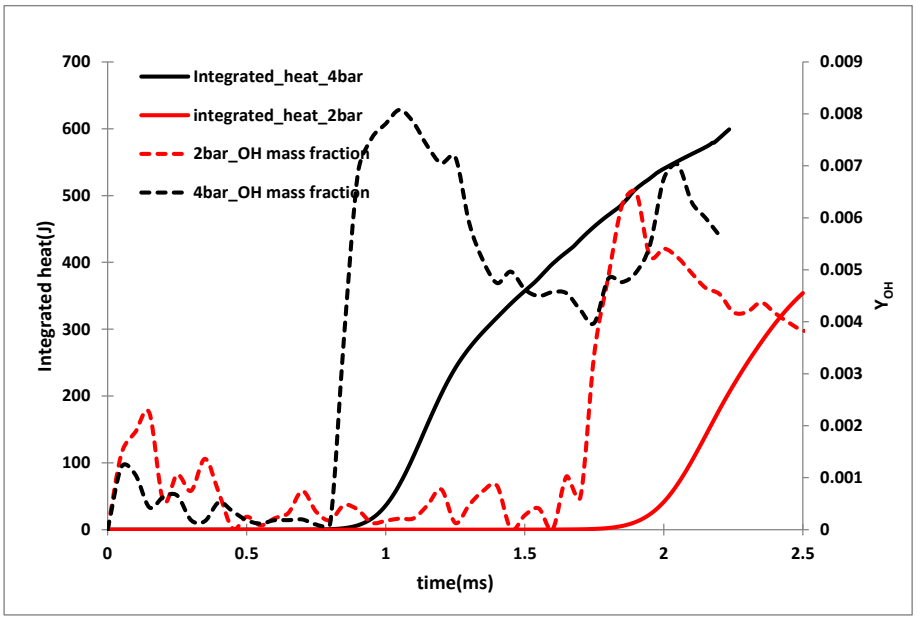

Figure 5.32. Integrated heat release in CVC chamber and OH mass fraction inside sphere domain for centered stationary jet, Fuel-A and 514 K CVC temperature and different pre-chamber pressure.

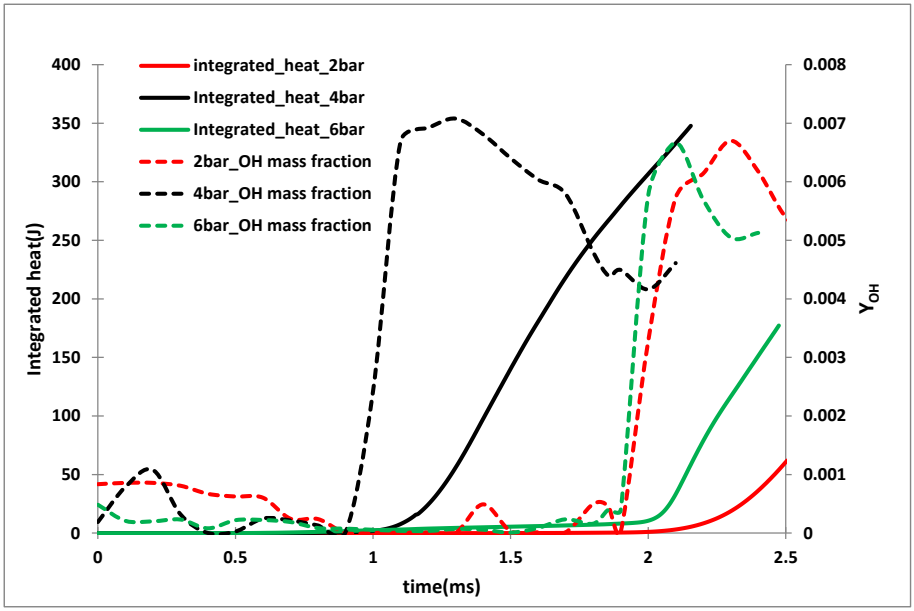

Figure 5.33. Integrated heat release in CVC chamber and OH mass fraction inside sphere domain for centered stationary jet, Fuel-B and 514 K CVC temperature and different pre-chamber pressure.

that ignition point. OH mass fraction is calculated within that sphere domain. This process is showed in Figure 5.31. Integrated heat release is the total value of heat generation within CVC chamber. OH mass fraction and integrated heat is plotted with time in Figure 5.32 for Case 5.11 and 5.13. For Cases 5.10, 5.12 and 5.14, OH mass fraction and integrated heat release is plotted in Figure 5.33.

OH mass fraction threshold is considered 0.003 (arbitrarily chosen) for successful ignition. From Figure 5.32 it is clear that, there is a time gap of 0.1 ms to 0.15 ms between the rapid increase of OH mass fraction and integrated heat. The same trend is also present in Figure 5.33. OH is an active radical which produces at the instant the fuel in CVC chamber start reacting. It generates at a certain region and then reacts with other species to generate more stable products. On the other hand, integrated heat release or heat release rate is the cumulative value energy or energy production rate in CVC chamber. Although OH mass production starts at the same time of heat generation in CVC chamber, cumulative heat needs 0.1 ms to 0.2 ms

more to show the increase. Mainly because it is accumulated over the whole CVC chamber not at the ignition point and also the range is reasonably higher compared to OH mass fraction. But from integrated heat or HRR plot significant amount of information can be extracted like the overall chemical kinetics rate, effects of shock wave etc. Therefore, ignition actually starts 0.1 ms to 0.2 ms earlier compared to rapid rise of integrated heat release is a reasonable assumption for this study.

5.4 Effects of Jet Traverse Speed

In an actual wave rotor consists of a pre-chamber jet ignition system, the wave rotor rotates while the stationary pre-chamber jet continuously supply hot combusted products into the wave rotor channels. This process creates counter rotating vortices in wave rotor combustor chamber, enhances mixing, creates possible ignitions sights by entraining unburnt fuel inside a vortex. This same process can be replicated by rotating the pre-chamber, keeping CVC chamber stationary. The single shot test rig at IUPUI replicates the actual physical phenomenon of wave rotor by rotating the pre-chamber which also contains the nozzle and keeping the CVC chamber stationary. Depending on the pre-chamber rotation rate, three different traverse speeds are considered for numerical study which is showed in Table 5.7. Different pre-chamber spin speeds means different traverse speeds of the jet. Different traverse speed affects the fluid mixing and vortex generation process. The slow traverse jet (40.1 ms) initially acts as a near wall jet and later impinges on the trailing wall of the CVC chamber. At this speed jet barely moves away from the side wall within the simulation time frame because the simulation time is around 3 ms and the jet needs 40.1 ms to move from leading edge of CVC chamber to trailing edge. As a result, the jet structure, penetration, and entrainment are close to near wall jet (a stationary jet near the leading wall), compared to the traversing motion. Traverse speed means the speed of nozzle in traverse direction (from leading wall to trailing wall) and traverse time means how much time the nozzle needs to cover the distance between the top wall

and bottom wall of CVC chamber at a certain traverse speed. Figure 5.34 shows the schematic representation of nozzle traverse.

Figure 5.34. Schematic illustrating the position of the nozzle at the start of jet traverse and at the end [36].

Table 5.7. Jet traverse speed and traverse time

Spin Rate (rpm)	Linear Traverse Speed (m/s)	Linear Traverse Time (ms)
150 (slow)	0.983	40.5
750 (moderate)	4.917	8.1
2000 (high)	13.112	3.1

Pre-chamber is consists of combusted products of 50% H_2 + 50% CH_4 with equivalence ratio 1.1. For CVC chamber Fuel-A with equivalence ratio 1.0, nine cases are considered depending on pre-chamber traverse speed and pressure. CVC chamber temperature and pressure are considered 300 K and 1 bar respectively. Detail properties of pre-chamber and CVC chamber are tabulated in Table 5.2.

With the same pre-chamber fuel and CVC chamber Fuel-B with equivalence ratio 1.0, three cases are considered which is showed in Table 5.9. Only 6 bar pre-chamber pressure is considered for this set of simulation because 6 bar has highest jet pen-

Table 5.8. Cases considered for traversing jet with Fuel-A

Case number	Pre-chamber pressure (bar)	Pre-chamber linear traverse time (ms)
5.16	2	40.5
5.17	2	8.1
5.18	2	3.1
5.19	4	40.5
5.20	4	8.1
5.21	4	3.1
5.22	6	40.5
5.23	6	8.1
5.24	6	3.1

Table 5.9. Cases considered for traversing jet with Fuel-B

Case number	Pre-chamber pressure (bar)	Pre-chamber linear traverse time (ms)
5.25	6	40.5
5.26	6	8.1
5.27	6	3.1

etration. CVC chamber temperature and pressure are considered 300 K and 1 bar respectively.

Integrated heat (IH) release in CVC chamber for Cases 5.16 through 5.24 is plotted in Figure 5.35. For 2 bar pre-chamber pressure, higher traverse speed cases fails to ignite (8.1 ms and 3.1 ms). Lowest traverse speed case (40.5 ms) which acts as a near wall jet starts ignition around 1.7 ms. For 4 bar pre-chamber pressure, ignition occurs for all the traverse speeds and it seems that traverse speed has minimal effect

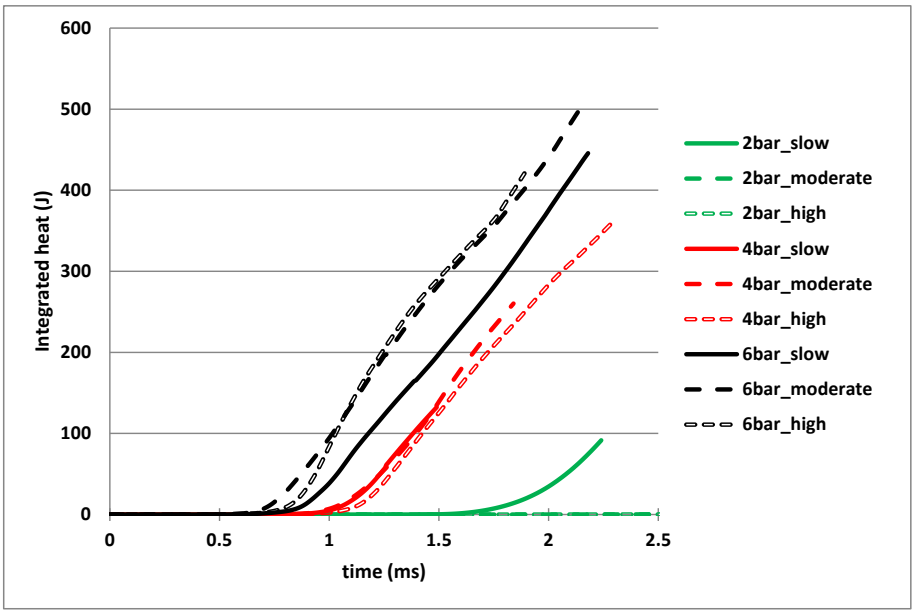

Figure 5.35. Comparison of integrated heat release in CVC chamber for rotating jet, Fuel-A, 300 K CVC chamber temperature with three different pre-chamber pressures and traverse speeds.

on ignition delay for this specific pre-chamber pressure. 40.1 ms and 8.1 ms case starts ignition at exact same time but the fastest jet (3.1 ms) starts ignition a bit later compared to other two cases. The slope of the integrated heat curve is almost similar for all the cases which indicate flame propagation and fuel burning rate is also identical within the simulation time. For 6 bar pre-chamber pressure, moderate jet speed case (8.1 ms) has the lowest ignition delay at around 0.7 ms. The fastest jet (3.1 ms) ignites at around 0.75 ms and the slowest jet (40.1 ms) starts ignition a bit later at around 0.8 ms. Although the fastest jet ignites a bit later than the moderate speed jet, the slope of the fastest jet integrated heat release curve is higher and at around 1.0 ms the integrated heat curve of the fastest jet go past the integrated heat release curve of moderate speed jet. This means that at this specific pressure, fastest jet has higher fuel burning rate compared to other jets.

Integrated heat(IH) release in CVC chamber for Cases 5.25 through 5.27 is plotted in Figure 5.36. In this figure, no rapid increase of heat is spotted within the simulation

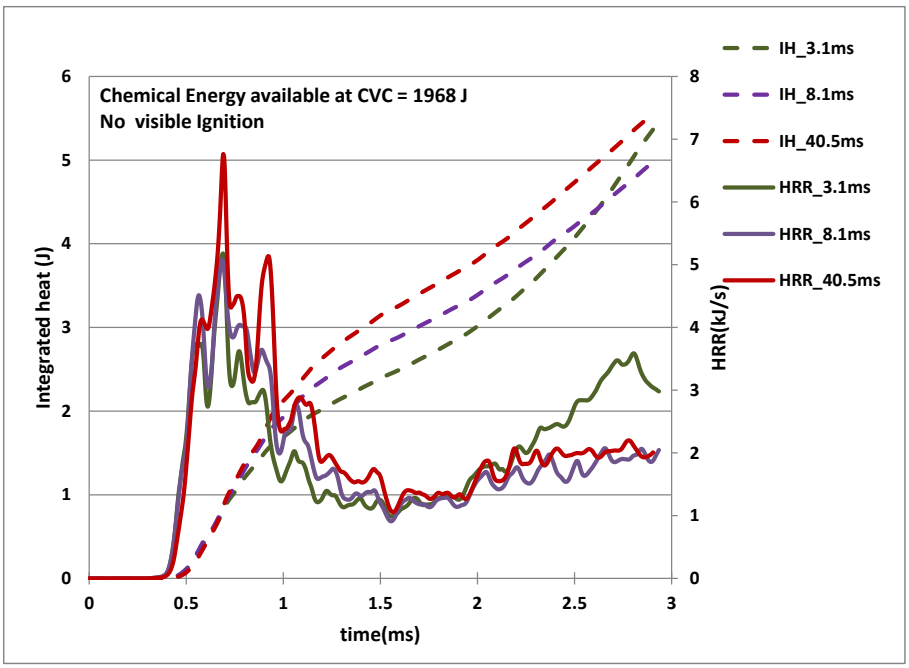

Figure 5.36. Comparison of integrated heat (IH) release and HRR in CVC chamber for rotating jet, Fuel-B, 300 K CVC chamber temperature with 6 bar pre-chamber pressure and different traverse speeds.

time for any of the cases as the total amount of energy available inside CVC chamber is 1968 J and after 3 ms integrated heat reaches around 5.5 J. As a result it is concluded that, ignition did not occur for any of the cases within the simulation time frame.

From traversing jet study it can be concluded that, the nozzle traverse time and pre-chamber pressure (which controls the mass flow rate) are found to be the two most important factors for successful ignition for a specific fuel in CVC chamber. Bilgin [31] concluded that temperature of the jet had major impact on main chamber ignition compared to the effects of nozzle thrust. As only one gas is considered for pre-chamber fuel, adiabatic temperature of pre-chamber combusted gas is same for all the cases. Only the nozzle thrust is varying. The varying pressure difference enables different amount of hot-jet mass to be injected into the main chamber highest for 6 bar pre-chamber pressure and lowest for 2 bar pre-chamber pressure (Figure 5.10) in a short duration. This mass becomes the defining variable as the jet traverse speed

increases. For successful ignition a certain amount of hot gas is needed at a certain place. If mass flow rate is low and traverse speed is high, hot gas eventually distribute itself and dilutes which results in unsuccessful ignition (Case 5.17 and 5.18). With higher pre-chamber rotation, higher distribution and mixing of hot jet take place in CVC chamber. If the mass flow rate is high enough, successful ignition will occur probably earlier for higher traverse speed jet. But this whole process inherently depends on fuel properties of pre-chamber and CVC chamber, specifically on their chemical ignition delay. So to draw an extensive conclusion, more research is needed for fuels with different ignition delay.

5.4.1 Flame Propagation for Traversing Jet

Turbulent flame is a highly complicated phenomenon and a unified definition for turbulent flame speed independent of measurement technique or diagnostic tool is not determined yet. The interaction process between turbulence and combustion chemistry is highly complicated. A turbulent flame is a highly wrinkled surface which may be thinner than the Kolmogorov scale and separates the reactants from the products [112]. Unlike laminar flame, turbulent flame propagation velocity depends on both characteristics of the flow (strain rate, surface curvature etc.) and mixture properties (chemical and thermal) [102]. According to Turns [102], "if an observer is traveling with a flame, turbulent flame speed is the velocity at which unburned mixture enters the flame in a direction normal to flame". The flame propagation velocity is relative to unburned gas velocity and if the unburned gas is not stationary, it is subtracted from the flame speed to get the proper turbulent flame speed.

Gas motion in pre-chamber jet ignition CVC chamber is highly complicated. Gas properties behind the flame are different than the gas properties in front of the flame due to volume expansion of combustion. Also the unburned gas is highly compressed into a small volume due to shock waves which is formed because of high pressure difference between pre-chamber and CVC chamber. As a result, the flame has access

to a relatively shorter distance to move. What we see is actually the gas motion velocity not the free flame propagation velocity. Flame is actually propagating with gas motion at a very high velocity compared to a reasonable turbulent flame speed of a hydrocarbon fuel. This very fast deflagration type flame is one of the major advantages of hot jet ignited constant volume combustion process.

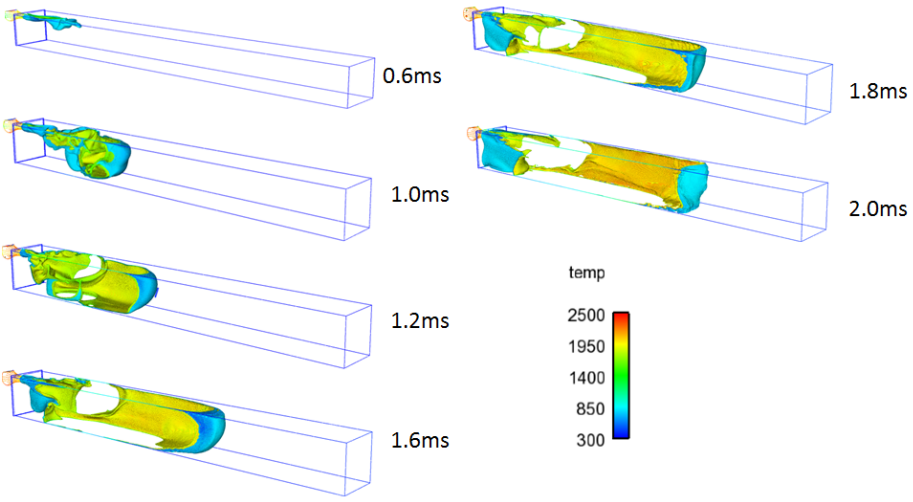

Figure 5.37. Isosurface of $Y_{CH_3} = 5e^{-5}$ to visualize flame propagation for 6 bar pre-chamber pressure, Fuel-A and 40.5 ms traversing time jet (Case 5.22) colored by temperature(K).

Isosurafce of $Y_{CH_3} = 5e^{-5}$ is plotted in Figures 5.37, 5.38 and 5.39 to visualize Cases 5.22, 5.23 and 5.24 respectively. After ignition, the flame propagation with gas motion is very fast and the speed is almost same for all the cases as the gas motion largely depends on the pressure difference of pre-chamber and CVC chamber which is same for all the cases. Also the first shock flame interaction occurs at around 1.5 ms for all the cases and deforms the flame front. After the impact, the flame front turns into an inverted dome shaped structured which is highlighted in Figure 5.39. This kind of deformation is also present for centered stationary jet cases. Inside the inverted dome, flame has access to unburned mixture. As a result, flame burns the trapped fuel air mixture and converted to a more flat surface (at 1.8 ms of Figure

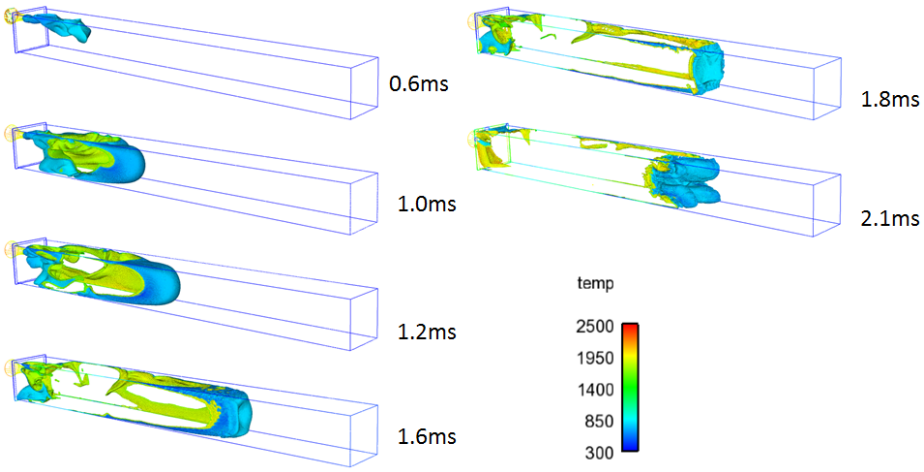

Figure 5.38. Isosurface of $Y_{CH_3} = 5e^{-5}$ to visualize flame propagation for 6 bar pre-chamber pressure, Fuel-A and 8.1 ms traversing time jet (Case 5.23) colored by temperature(K).

5.38). The second shock interacts with the flame from the upstream side and thrust the flame forward (at 2.1 ms of Figure 5.38).

To understand more about the physical structure behind the inverted dome shape of the flame front, velocity magnitude and velocity vector is plotted in Figure 5.40 for Case 5.24. At part (a), Velocity vector is plotted from a line tool carefully placed infront of the propagating flame at the center of the CVC chamber. The arrows of the vector show the direction of the velocity. The length and color show the magnitude of the velocity. Part (b) is showing the velocity magnitude of the flame front. From part (b), it is evident that the velocity of the propagating flame around 1.4 ms is around 280 m/s. The maximum value of freely propagating turbulent flame speed for a hydrocarbon fuel is around 2.0 m/s. This is actually verifying that flame is propagating with gas motion, also demonstrating the difficulty regarding turbulent flame speed calculation. Due to SFI at around 1.5 ms vorticity deposits on flame front which changes the flame surface area. Also SFI changes the pressure difference around the flame surface which may result into velocity change. But the main reason of this behind this structural change of flame front may be momentum. The center region of

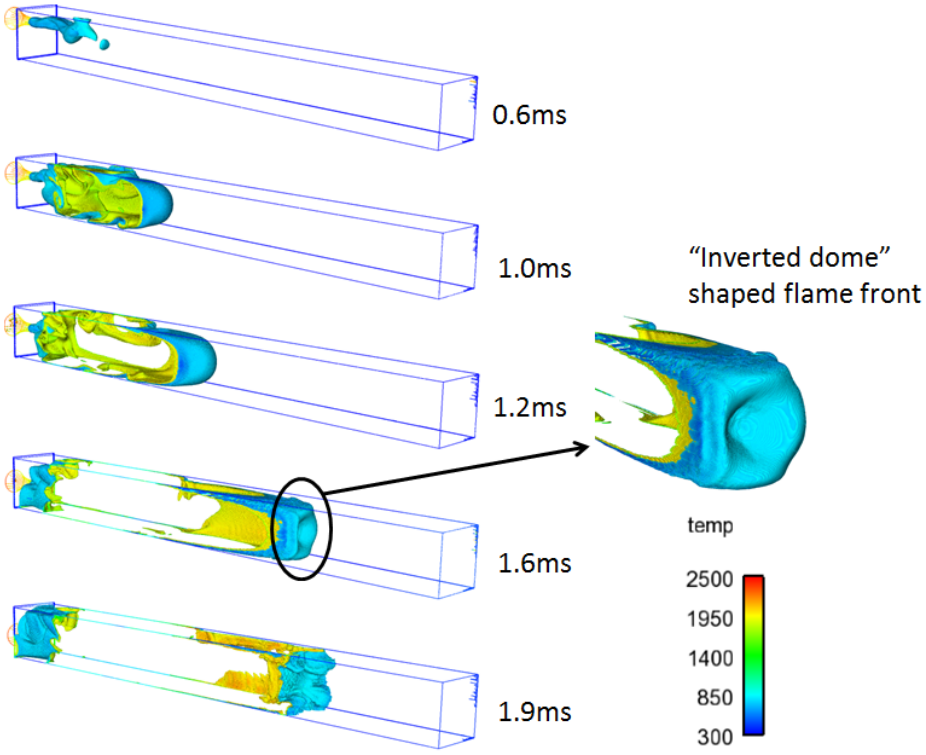

Figure 5.39. Isosurface of $Y_{CH_3} = 5e^{-5}$ to visualize flame propagation for 6 bar pre-chamber pressure, Fuel-A and 3.1 ms traversing time jet (Case 5.24) colored by temperature(K).

the flame front is relatively hotter than the region close to wall. Temperature affects the velocity, that's why the flame front center has velocity magnitude around 280 m/s and the region near the wall have velocity around 150 m/s at 1.4 ms. Also due to higher temperature, center of the flame front has relatively lower density of gas (lower momentum). Also region near the wall has higher density gas (higher momentum). So, when SFI occurs, due to lower momentum and higher acceleration the center of the flame front decrease velocity rapidly compared to the near wall region of the flame which has higher momentum. As a result, the near wall region of the flame keeps going but center of the flame loses momentum, which results to the 'inverted dome' structure.

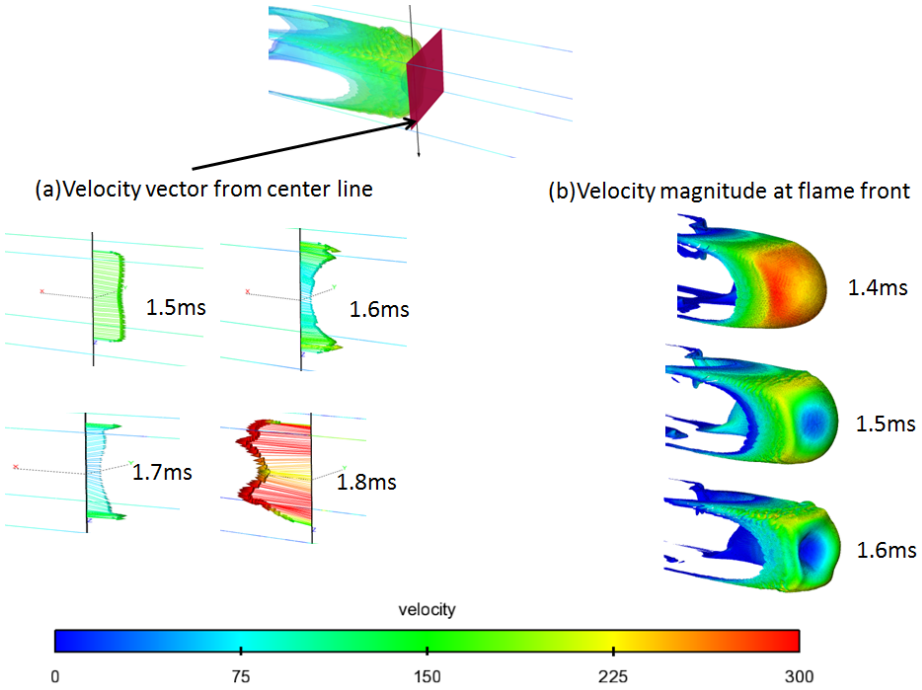

Figure 5.40. For Case 5.24 (a) Velocity vectors from a carefully placed line tool at the center of CVC chamber where arrows show velocity direction and colors show velocity magnitude (m/s), (b) Isosurface of $Y_{CH_3} = 5e^{-5}$ and colored by velocity (m/s).

Temperature contour history of Cases 5.22, 5.23 and 5.24 are plotted in Figure 5.41 (a), (b) and (c) respectively. Case 5.22 and 5.23 shows almost same fluid dynamics behavior with Case 5.23 igniting a little bit earlier. They start as a near wall jet and later impinge to the trailing wall of CVC chamber which is already described in literature [36, 66]. Case 5.24 has the highest jet traverse speed, which creates higher turbulent kinetic energy in CVC chamber. May be due to higher kinetic energy and mixing, at 0.6 ms the front end of the jet is detaching from the main flow and later at 0.8 ms the detached part is igniting.

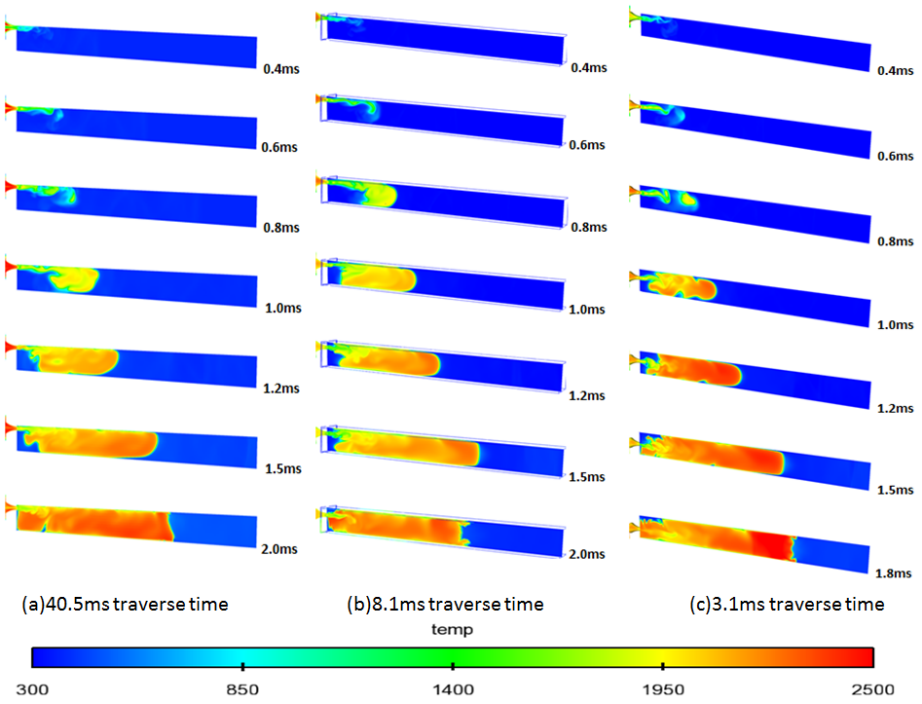

Figure 5.41. Contour plot of temperature (K) history for 6 bar pre-chamber pressure, Fuel-A and (a) 40.5 ms traverse time (Case 5.22), (b) 8.1 ms traverse time (Case 5.23), (c)3.1 ms traverse time jet (Case 5.24).

5.5 Ignition: A Function of Species Mass Fraction and Temperature

Hot jet ignition in CVC chamber is a three dimensional phenomenon which consists of mixing of hot and cold mixture to a certain limit which is suitable for developing a flame kernel and ultimately supporting the flame kernel to grow into a definite extent which will not extinct. Ignition starts at a certain point which can be observed from the temperature contour plot (sudden increase of temperature at a certain point) or OH mass fraction plot. Ignition suddenly changes the thermodynamic and fluid dynamic properties of a certain region by increasing temperature and pressure. After ignition, reactants are converted to products and the changes are too fast to track. Therefore, if the intention is to study the underlying properties of ignition, investigation at the ignition point without the sudden rise of temperature

and pressure (meaning without any chemical reaction or combustion) will provide data which are suitable for ignition. If a certain amount of pre-chamber mass has to mix with a certain amount of CVC chamber mass at a certain temperature for successful ignition; those amounts can be traced if the ignition point is investigated when combustion model is turned off. The reason for using combustion-off results is to find out the species concentration at the possible ignition point.

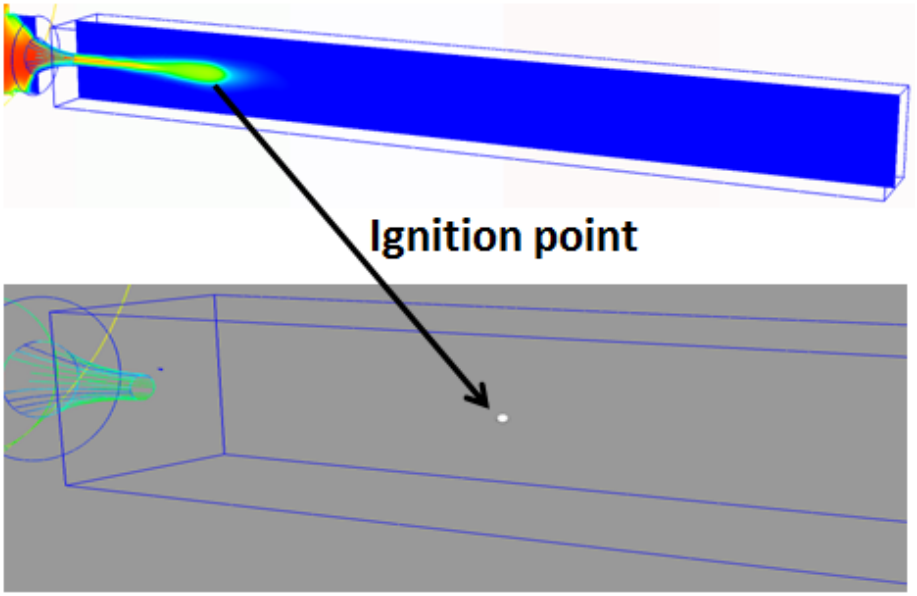

Figure 5.42. Ignition point selected inside the CVC chamber.

Twelve cases are considered to study the ignition trends in 3D space and time which are showed in Table 5.10. Combustion model is turned off for each of the cases. The simulations are showing the fluid dynamic properties of hot gas mixing with cold gas without any chemical reactions.

The ignition point is selected from the case where combustion model is turned on. As an example, for Case 5.2, pre-chamber fuel is combusted products of 50%CH_4 + 50%H_2 with equivalence ratio 1.1, centered stationary jet, 2 bar pre-chamber pressure, Fuel-A, 300 K CVC temperature and combustion model is turned on. From Figure 5.3(a) (temperature contour history) it is evident that ignition starts at around 2.0

Table 5.10. Case number and properties for ignition study cases with combustion model turned off

Case number	Case condition
5.28	Case 5.2 with combustion model turned off
5.29	Case 5.4 with combustion model turned off
5.30	Case 5.6 with combustion model turned off
5.31	Case 5.22 with combustion model turned off
5.32	Case 5.23 with combustion model turned off
5.33	Case 5.24 with combustion model turned off
5.34	Case 5.11 with combustion model turned off
5.35	Case 5.13 with combustion model turned off
5.36	Case 5.15 with combustion model turned off
5.37	Case 5.10 with combustion model turned off
5.38	Case 5.12 with combustion model turned off
5.39	Case 5.14 with combustion model turned off

ms. The point where sudden rise of temperature is first observed is selected as ignition point which is showed in Figure 5.42. The co-ordinate of the ignition point is different for different cases. For each case the specific ignition point is carefully selected. Now the same case (same properties in pre-chamber and CVC chamber) is simulated with combustion model turned off (Case 5.28 for Case 5.2). Now, the co-ordinates of the ignition point which is already measured (from Case 5.2) are used to identify the ignition point for the case with combustion model turned off (Case 5.28). Properties which are identified important are measured at this ignition point with time.

Pre-chamber mass fraction, CVC chamber mass fraction, air mass fraction and temperature history is plotted in Figure 5.43 (a), (b) and (c) for Case 5.28, 5.29 and 5.30 respectively. Ignition delay is selected from the integrated heat release plot (Figure 5.1) for each case when combustion model is turned on. A time range of 0.15

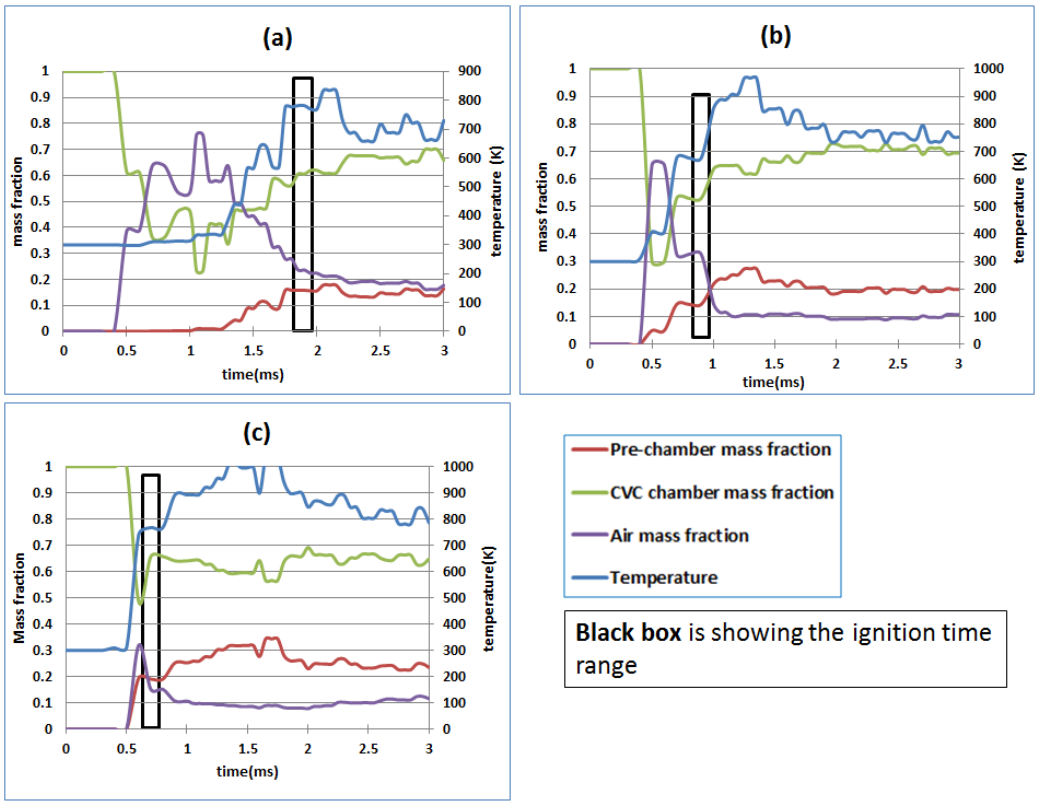

Figure 5.43. For centered stationary jet, Fuel-A, 300 K CVC temperature case calculated pre-chamber mass fraction, CVC chamber mass fraction, air mass fraction and temperature history at ignition point when combustion model is turned off for (a) 2 bar (Case 5.28), (b) 4 bar (Case 5.29) and (c) 6 bar (Case 5.30) pre-chamber pressure. The black box at each graph is showing the time range within which ignition starts when the combustion model is turned on.

ms to 0.2 ms is selected around the ignition delay time within which ignition is most probable to start and showed in the Figure with a black box. Is there any trend which is common for all the cases to start the ignition? The author is seeking answer of this question.

From Figure 5.43 it is evident that, inside the ignition time range (black box), the variables (pre-chamber mass fraction, CVC chamber mass fraction, air mass fraction and temperature) plotted are within a certain range for all the cases. This is implying that, all these variables have to be within this range for a successful igni-

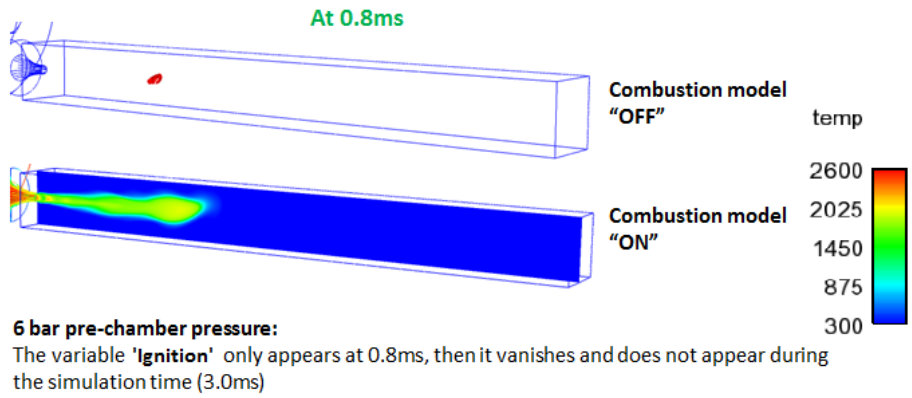

Figure 5.44. Predicting ignition for centered stationary jet, Fuel-A, 300 K CVC temperature 6 bar pre-chamber pressure case and comparing with temperature contour plot (Case 5.30). 'Ignition' is appearing as a red surface when combustion model is off. Combustion model on is showing temperature contour.

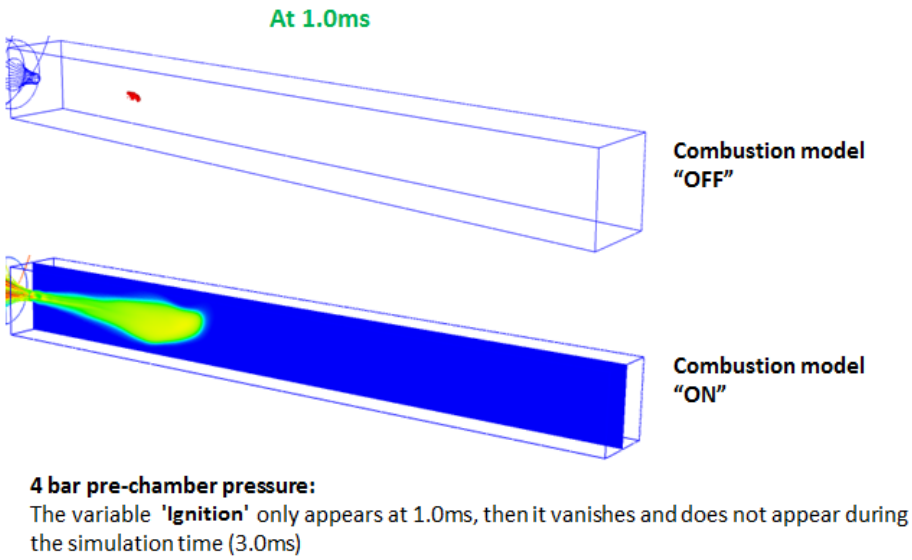

Figure 5.45. Predicting ignition for centered stationary jet, Fuel-A, 300 K CVC temperature 4 bar pre-chamber pressure case and comparing with temperature contour plot (Case 5.29).'Ignition' is appearing as a red surface when combustion model is off. Combustion model on is showing temperature contour.

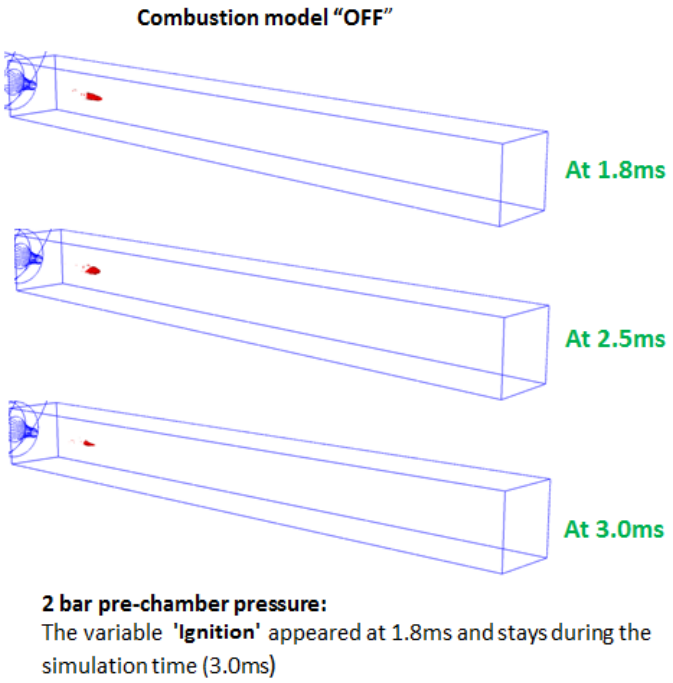

Figure 5.46. Predicting ignition for centered stationary jet, Fuel-A, 300 K CVC temperature 2 bar pre-chamber pressure case and comparing with temperature contour plot (Case 5.28).'Ignition' is appearing as a red surface when combustion model is off.

tion. Therefore, a new variable named 'ignition' is proposed which has the following properties:

'Ignition'

0.1<Pre-chamber mass fraction<0.2

0.55<CVC chamber mass fraction<0.65

Temperature>700 K

This new variable 'Ignition is defined in post-processing in such a way that it will appear as a red surface only when all the above mentioned conditions are met. Which means all the cells inside CVC chamber containing the properties of the variable 'Ignition' will turn to red. Basically this variable is showing which cells are eligible to start ignition inside the CVC chamber. Therefore, 'Ignition' is plotted in Figures 5.44,

5.45 and 5.46 for Case 5.30, 5.29 and 5.28 respectively and compared with the contour plot of temperature which is selected from the same case where combustion model is turned on. At Figure 5.44, 'Ignition' is plotted for Case 5.30 (indicated by combustion model 'off') and compared with temperature contour of Case 5.6 (indicated by combustion model 'on').

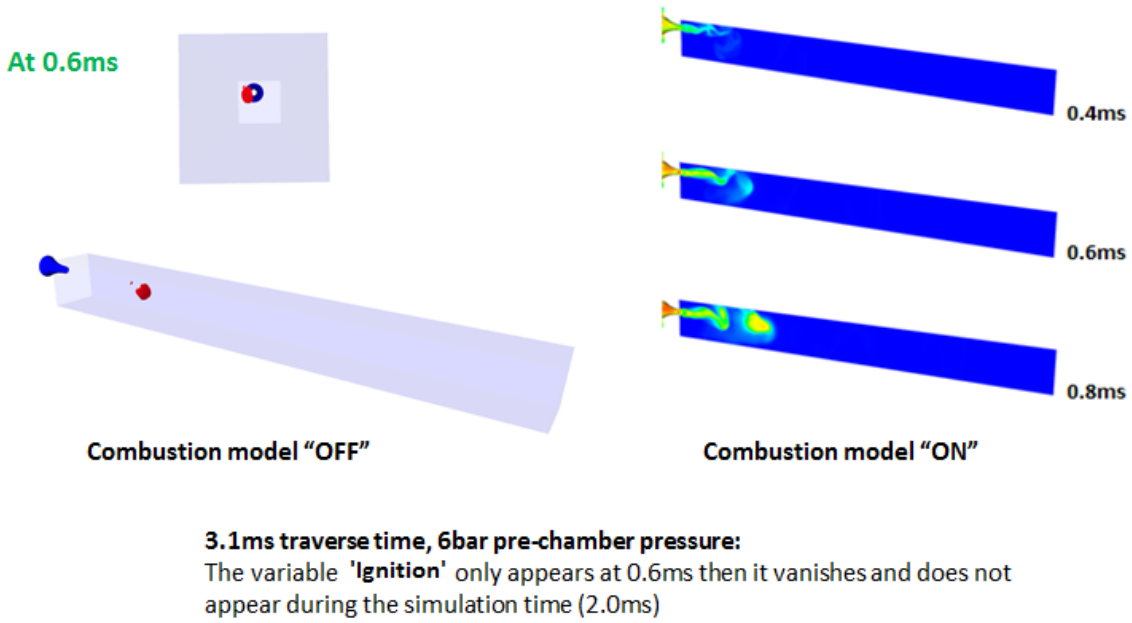

Figure 5.47. Predicting ignition 3.1 ms traverse time jet, Fuel-A, 300 K CVC temperature 6 bar pre-chamber pressure case and comparing with temperature contour plot (Case 5.33). 'Ignition' is appearing as a red surface when combustion model is off. Combustion model on is showing temperature contour.

For 6 bar and 4 bar pre-chamber pressure (Figures 5.44 and 5.45 respectively), the variable 'Ignition' is appeared only at 0.8 ms and 1.0 ms respectively. For 2 bar pre-chamber pressure (Figure 5.46), 'Ignition' appears at around 1.8 ms and stays visible from thereafter. This is actually indicating that, 6 bar and 4 bar pre-chamber pressure cases have higher mixing and as a result the conditions which are suitable for ignition only appear at a certain time and place and then disappears. On the

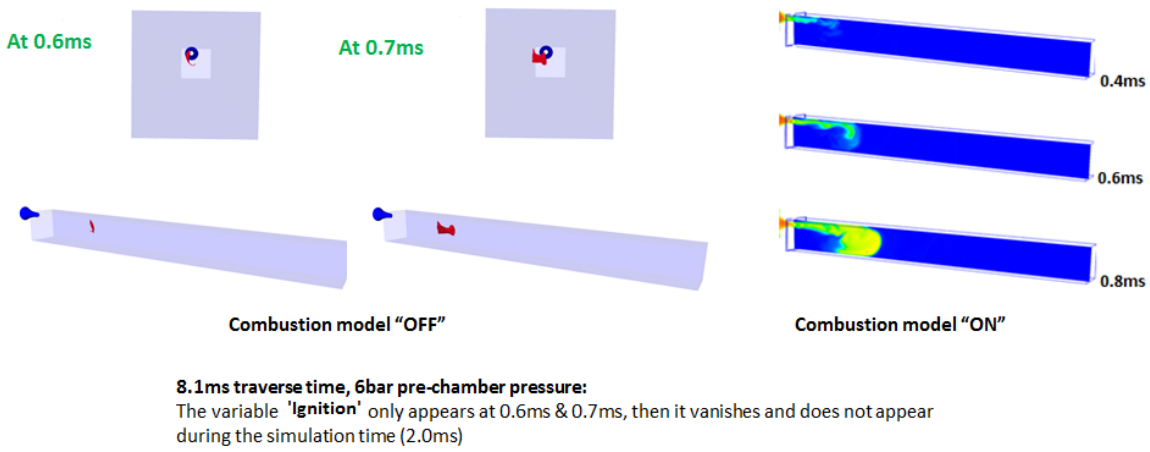

Figure 5.48. Predicting ignition 8.1 ms traverse time jet, Fuel-A, 300 K CVC temperature 6 bar pre-chamber pressure case and comparing with temperature contour plot (Case 5.32). 'Ignition' is appearing as a red surface when combustion model is off. Combustion model on is showing temperature contour.

Table 5.11. Duration time of the variables 'Ignition' and 'Ignition1'

Case number	Duration time
5.28	"Ignition" appears at 1.8 ms and stays till 3.0 ms
5.29	"Ignition" appears only at 1.0 ms
5.30	"Ignition" appears only at 0.8 ms
5.31	"Ignition" appears at 0.6 ms and stays till 0.7 ms
5.32	"Ignition" appears at 0.6 ms and stays till 0.7 ms
5.33	"Ignition" appears only at 0.6 ms
5.34	"Ignition1" appears at 1.7 ms and stays till 2.5 ms
5.35	"Ignition1" appears at 0.7 ms and stays till 0.8 ms
5.36	"Ignition1" appears at 0.6 ms and stays till 0.7 ms

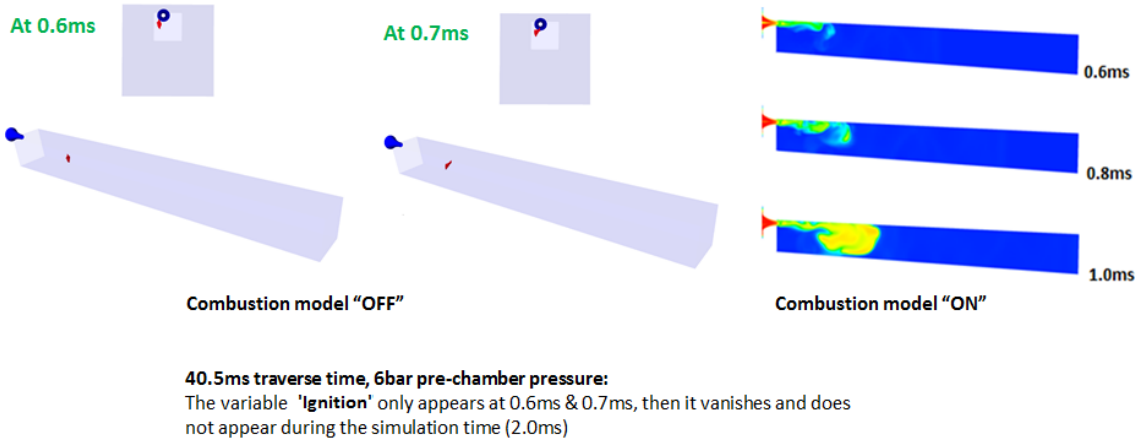

Figure 5.49. Predicting ignition 40.5 ms traverse time jet, Fuel-A, 300 K CVC temperature 6 bar pre-chamber pressure case and comparing with temperature contour plot (Case 5.31). 'Ignition' is appearing as a red surface when combustion model is off. Combustion model on is showing temperature contour.

Table 5.12. Successful ignition criteria for Cases 5.37, 5.38 and 5.39

Case number	Pre-chamber mass fraction	CVC chamber mass fraction	Temperature (K)
5.37	0.2-0.3	0.45-0.5	$\geq$ 1100
5.38	0.35-0.45	0.35-0.45	$\geq$ 1100
5.39	0.2-0.3	0.6-0.7	$\geq$ 1000

other hand, 2 bar pre-chamber pressure has less mixing which results into sustaining the suitable condition for ignition for a longer amount of time. It is also important to note that, for Figure 5.44 and 5.45 the criteria 'Ignition' appears within the time range which is used to define the variable. That means the time of ignition which is

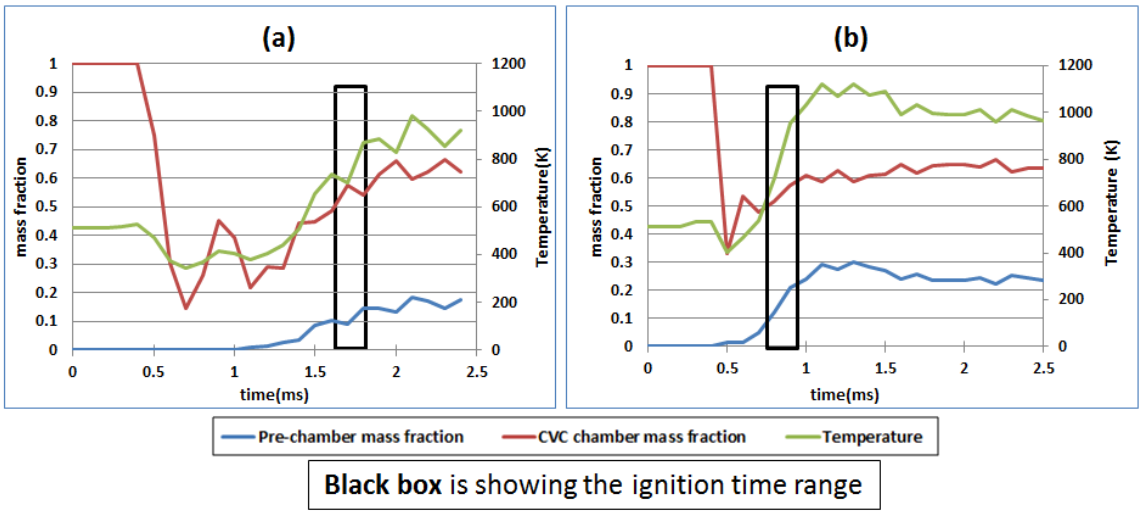

Figure 5.50. For centered stationary jet, Fuel-A, 514 K CVC temperature case calculated pre-chamber mass fraction, CVC chamber mass fraction and temperature history at ignition point when combustion model is turned off for (a) 2 bar (Case 5.34) and (b) 4 bar (Case 5.35) pre-chamber pressure. The black box at each graph is showing the time range within which ignition starts when the combustion model is turned on.

between 0.6-0.8 ms for Case 5.30. But for Figure 5.46 the time range which is used to define 'Ignition' criteria is 1.8 ms to 2.0 ms. But 'Ignition' sustains even after 2.0 ms. Therefore, it is actually showing all the ignition points in 3D space (including the ignition point which is used to calculate 'Ignition' criteria) which are available for successful ignition.

Now to take the study one step further, the same variable 'Ignition' is plotted for Case 5.33, 5.32 and 5.31 at Figure 5.47, 5.48 and 5.49 respectively. The cases considered have the same thermodynamic properties in pre-chamber and CVC chamber, the only thing which is different is the pre-chamber traverse speed. As a result, if ignition is dependent on pre-chamber mass fraction, CVC chamber mass fraction and temperature, the same criteria (range of variables) which are used to define 'Ignition' before should be also successful to predict the ignition for these cases too. Because

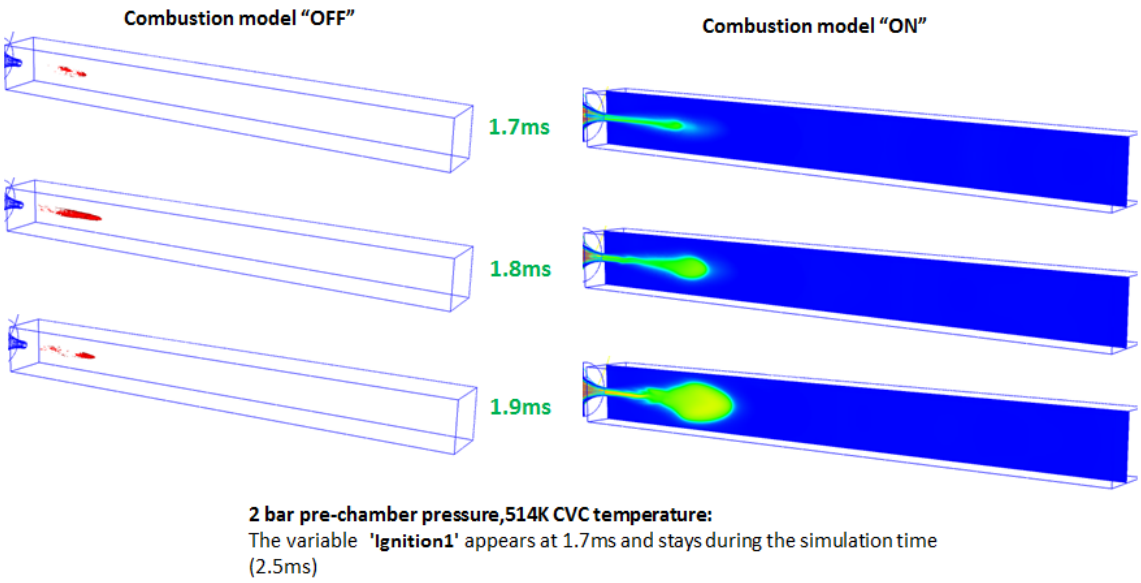

Figure 5.51. Predicting ignition for centered stationary jet, Fuel-A, 514 K CVC temperature, 2 bar pre-chamber pressure case and comparing with temperature contour plot (Case 5.34). 'Ignition1' is appearing as a red surface when combustion model is off. Combustion model on is showing temperature contour.

thermodynamically every case is same, the only difference is, Cases 5.28, 5.29 and 5.30 are for centered stationary jet and Cases 5.31, 5.32 and 5.33 are for rotating pre-chamber.

The variable 'Ignition' appears at 0.6 ms for Case 5.33 (Figure 5.47). Comparing from the temperature contour it is clear that ignition starts around 0.6 ms. The variable is also successful in predicting the ignition spot in 3D space. For Case 5.32 and 5.31 'Ignition' appears at 0.6 ms and 0.7 ms (Figure 5.48 and 5.49). From the temperature plot it is evident that ignition starts at around 0.7 ms for Case 5.32 and 0.9 ms for Case 5.31. Therefore, the variable 'Ignition' is successful in predicting ignition in space and time.

Now three more Cases 5.34, 5.35 and 5.36 are selected where CVC chamber temperature is 514 K. As a result, thermodynamically these cases are different than the

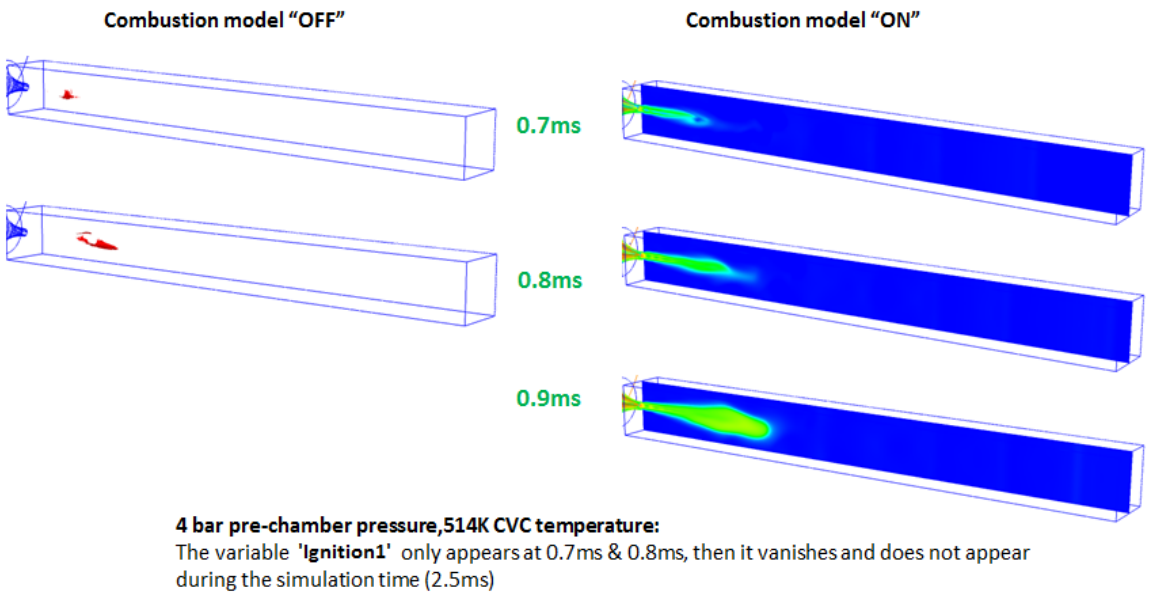

Figure 5.52. Predicting ignition for centered stationary jet, Fuel-A, 514 K CVC temperature, 4 bar pre-chamber pressure case and comparing with temperature contour plot (Case 5.35). 'Ignition1' is appearing as a red surface when combustion model is off. Combustion model on is showing temperature contour.

cases discussed before. Pre-chamber mass fraction, CVC chamber mass fraction and temperature history at ignition point is plotted in Figure 5.50 for Cases 5.34 and 5.35. Ignition delay is calculated from integrated heat plot from Figure 5.28. Studying Figure 5.50 a new variable 'Ignition1' is defined which has the following criteria:

'Ignition1'

0.1<Pre-chamber mass fraction<0.2

0.5<CVC chamber mass fraction<0.6

Temperature>750 K

'Ignition1' is a subset of the previously defined variable 'ignition' and plotted in Figures 5.51, 5.52 and 5.53 for Cases 5.34, 5.35 and 5.36 respectively and compared with the contour plot of temperature which is selected from the same case where

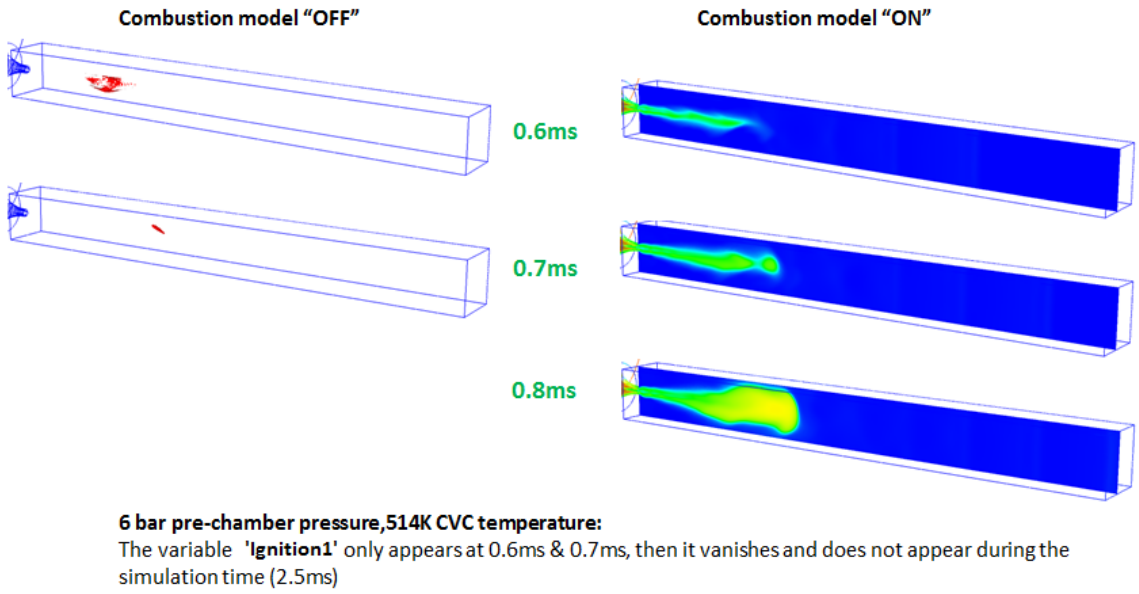

Figure 5.53. Predicting ignition for centered stationary jet, Fuel-A, 514 K CVC temperature, 6 bar pre-chamber pressure case and comparing with temperature contour plot (Case 5.36). 'Ignition1' is appearing as a red surface when combustion model is off. Combustion model on is showing temperature contour.

combustion model is turned on. For 2 bar and 4 bar pre-chamber pressure (from which 'Ignition1' is calculated, Case 5.34 and 5.35) successfully predicts the ignition in 3D space and time which is evident from Figures 5.51 and 5.52 respectively. For 6 bar pre-chamber pressure (from which 'Ignition1' is not calculated, Case 5.36) 'Ignition1' also successfully predicts the ignition in 3D space and time which is showed in Figure 5.53. It is also important to note that, both variables 'Ignition' and 'Ignition1' are calculated from a single ignition point in 3D space. But their contour plots show that there are actually several regions where the condition for successful ignition is actually available but the flame kernel fails to develop. This evidently supports the previous claim that, to develop the ignition kernel, supports from the nearby cells are necessary.

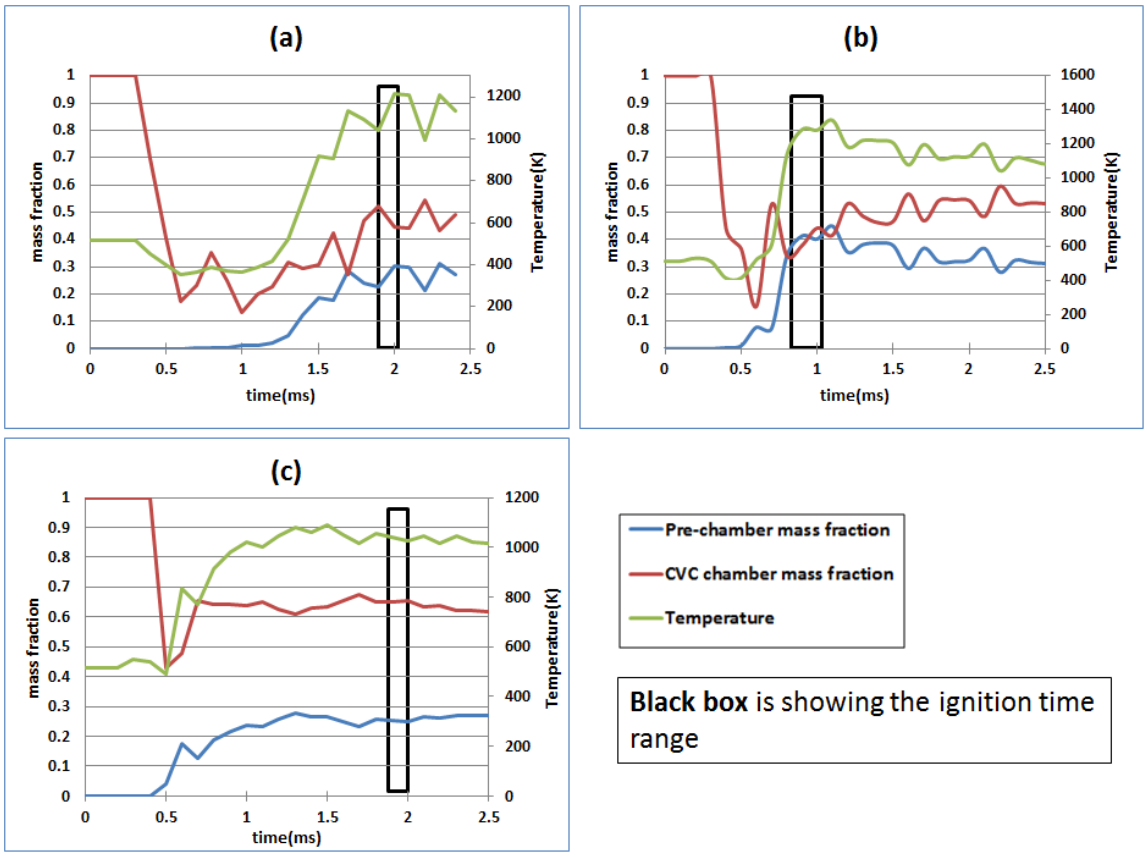

Figure 5.54. For centered stationary jet, Fuel-B, 514 K CVC temperature case calculated pre-chamber mass fraction, CVC chamber mass fraction and temperature history at ignition point when combustion model is turned off for (a) 2 bar (Case 5.37), (b) 4 bar (Case 5.38) and (c) 6 bar (Case 5.39) pre-chamber pressure. The black box at each graph is showing the time range within which ignition starts when the combustion model is turned on.

The duration time of the variables 'Ignition' and 'Ignition1' with respect to their case numbers is tabulated in table 5.11.

For Fuel-B a same set of analysis of ignition is carried out for centered stationary jet and 514 K CVC chamber temperature. Mass fraction of pre-chamber and CVC chamber species, and temperature is analyzed in Figure 5.54 and tabulated in table 5.12.

For Fuel-B, ignition temperature is above 1000 K which is relatively higher compared to Fuel-A (700 K). Also a higher amount of pre-chamber mass fraction (which contains the active radicals and hot jet) is needed to start ignition. AS Fuel-B has lower reactivity compared to Fuel-A, these trends are expected and reasonable.

5.6 Validation

Validation is important and necessary for CFD studies. For combustion CFD, most common type of validation is pressure history comparison in combustion chamber. Ignition delay comparison is also important. The ignition rig studied here has pressure sensors installed in three different locations. Ignition delay can also be measured using high speed camera and Z-type schlieren system. CFD results are available for pressure sensors and ignition delay. But high quality experimental data for this ignition rig with the conditions studied in this research are not available at this moment. As a result quantitative validation is not presented here. Several features of hot-jet ignition which are captured in this current study are compared with published experimental and numerical results and qualitative validation is presented.

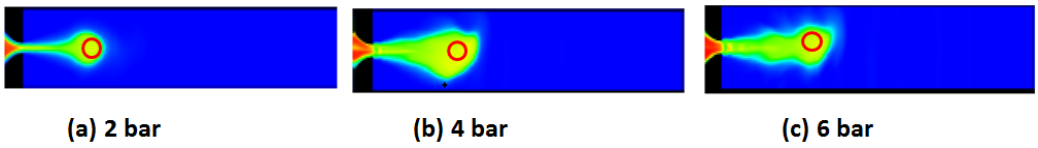

Figure 5.55. Ignition location for Fuel-A, centered stationary jet (a) 2 bar (Case 5.2), (b) 4 bar (Case 5.4) and (c) 6 bar (Case 5.6) pre-chamber pressure (current study).

5.6.1 Ignition Start Location

Sadanandan et al. [3] experimentally studied the ignition of hydrogen/air mixtures by jets of hot exhaust gases. Both pre-chamber (volume 0.226 L) and main chamber (volume 12 L) were filled up with 28:72 hydrogen-air mixture at atmospheric pressure.

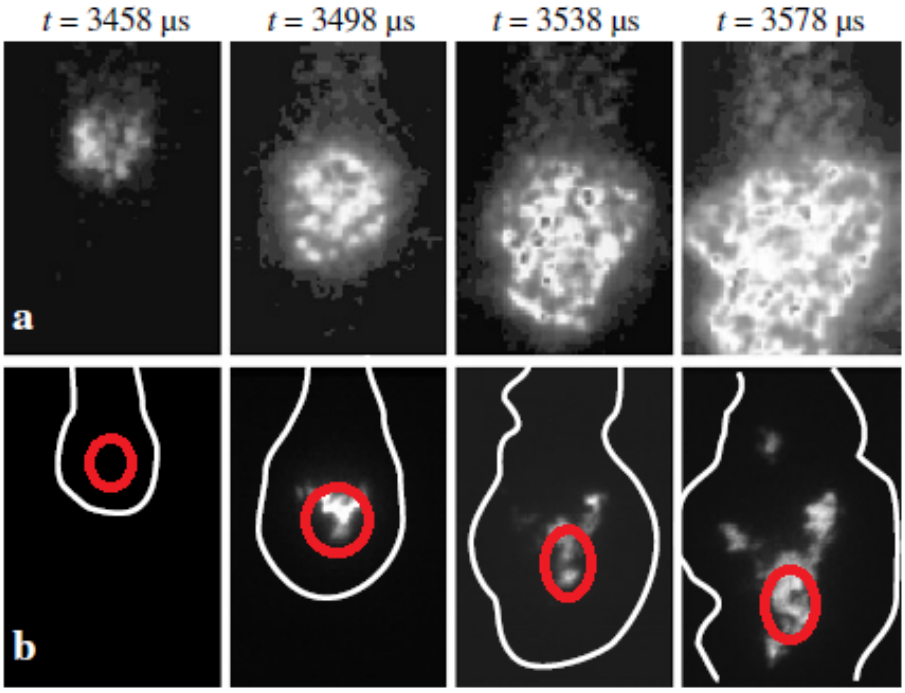

Figure 5.56. (a) Simultaneous laser Schlieren and (b) OHPLIF sequences for pre-chamber pressure/CVC chamber pressure = 4.75 and nozzle diameter = 1.1 mm. [3]

Pre-chamber mixture is ignited with a spark plug and high pressurized combusted gas from pre-chamber goes to main chamber through a nozzle. They observed that ignition starts near the jet tip and not at lateral side of the jet (Figure 56). They stated that, different mixing behavior may be the reason behind this. At the lateral sides high shear stress increase the mixing and at the jet tip mixing is reduced. Therefore, probability of ignition is increased in this area. In the current study for Fuel-A, ignition is also observed near the jet tip (Figure 55). Fuel-A is highly reactive and chemical ignition delay is slightly high but comparable with pure hydrogen. This may be the reason behind this similar type of behavior.

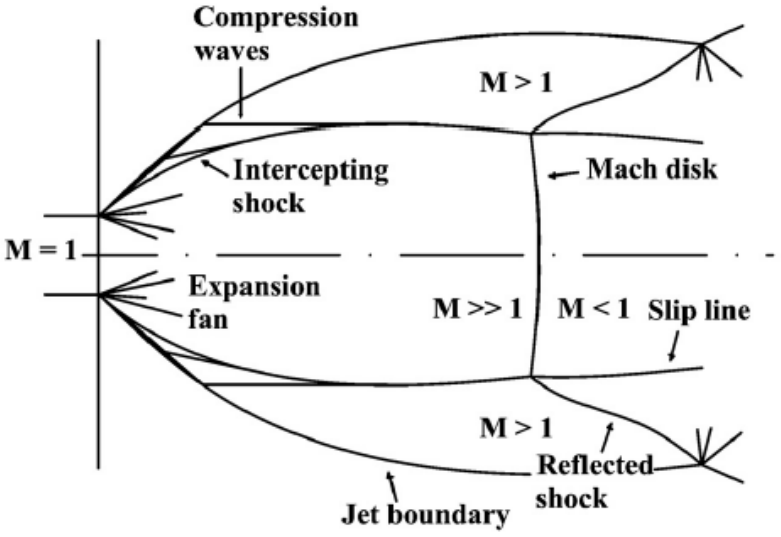

Figure 5.57. Schematic of underexpanded sonic jet [113].

5.6.2 Underexpanded Jet Structure

The complicated flow structures of underexpanded jet are already explained earlier (5.2.2 Effects of jet velocity and mass flow rate). Figure 5.57 is showing a schematic of how an underexpanded sonic jet is developed. Various features of the underexpanded jet (Mach disk, slip line and reflected shock) and different zones (M¡1, M¿¿1 and M¿1) are captured completely in this current study (Figure 5.58 (a)). They also showed reasonably good agreement with the shadowgraph image (Figure 5.58). The exhaust of the LOX/methane test engine developed by NASA is showing the 3D features of the shock diamonds (Figure 5.59). Shock diamond is a 3D phenomenon and hard to capture with 2D simulations. With 3D simulation and reasonable refined mesh these complicated structures are captured in this current study.

5.6.3 Structure of Turbulent Jet Plume

The formation of turbulent jet plume is a purely fluid-mechanical process and does not depend on chemical reactions. Salient features of the turbulent jet plume

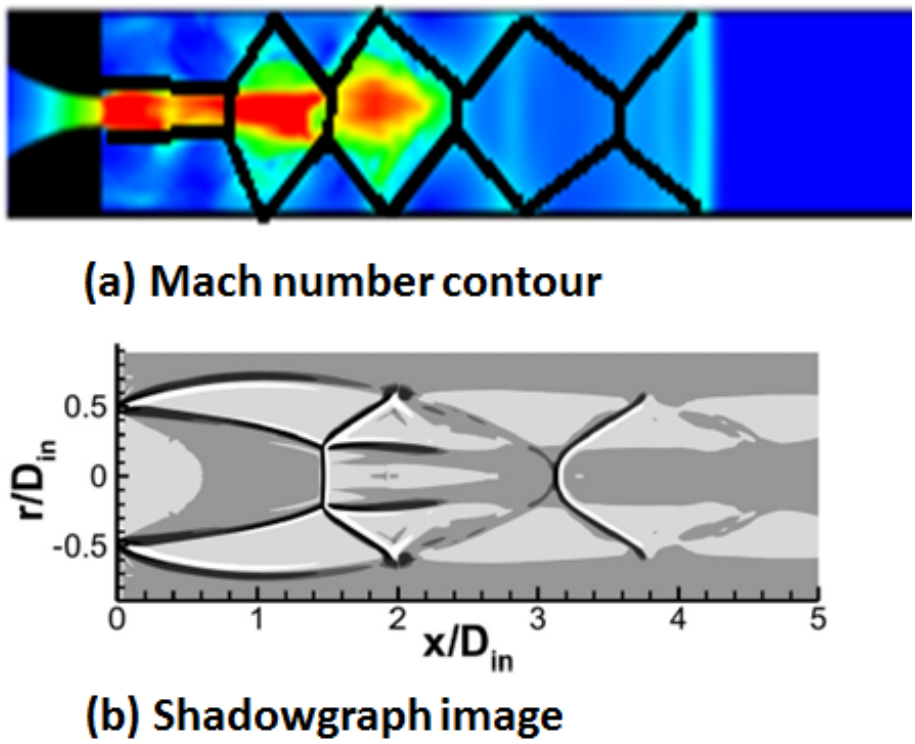

Figure 5.58. (a) Mach number contour of current study (Case 5.9 at 0.4 ms)(b) Schematic of underexpanded sonic jet [113].

is described in Figure 5.60 [107]. The characteristics features of large scale vortex structures and entrainment pathways are presented here. Three distinct features of turbulent jet plume are: 1- zones of intense shear (just outside of nozzle), 2- cores of large scale vortices and 3-pathways of entrainment (pathways of the large scale vortices to entrain unburned air-fuel mixture).

Figure 5.60 is the contour plot of velocity vector for Case 5.9. How velocity vector is plotted is described earlier (5.2.2 Effects of jet velocity and mass flow rate). Three distinct features of the turbulent jet plume which is presented in Figure 5.61 is also captured in the current study. More detail representation can be found in Figures 5.11-5.13.

Figure 5.59. Test firing of a 7,500 pound-thrust LOX/methane engine. Image credit: Mike Massee/XCOR Aerospace. [106].

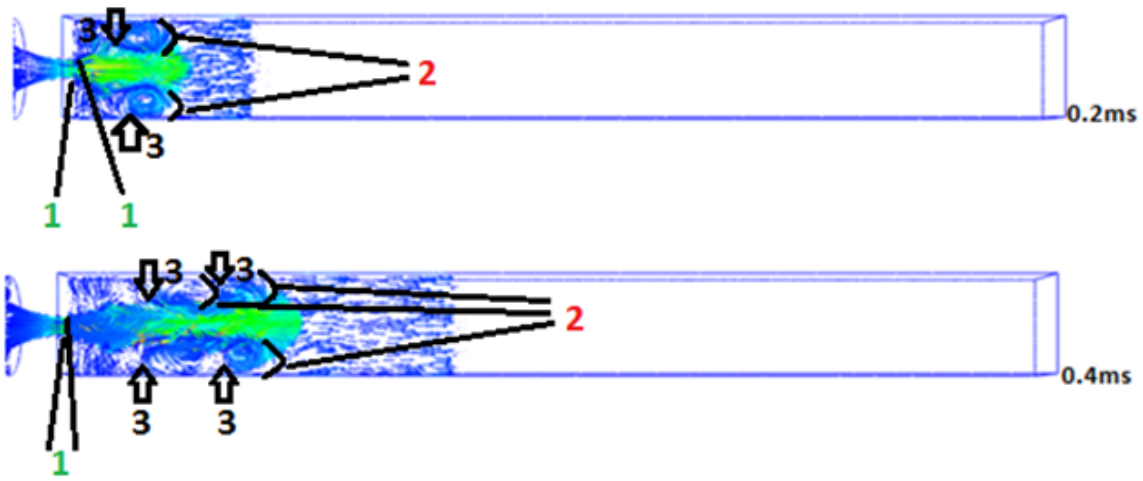

Figure 5.60. Velocity vector contour plot (Case 5.9): formation and Structure of a Turbulent Jet Plume. 1-zones of intense shear with stretch and extinction; 2-cores of large scale vortices, 3-pathways of entrainment (current study).

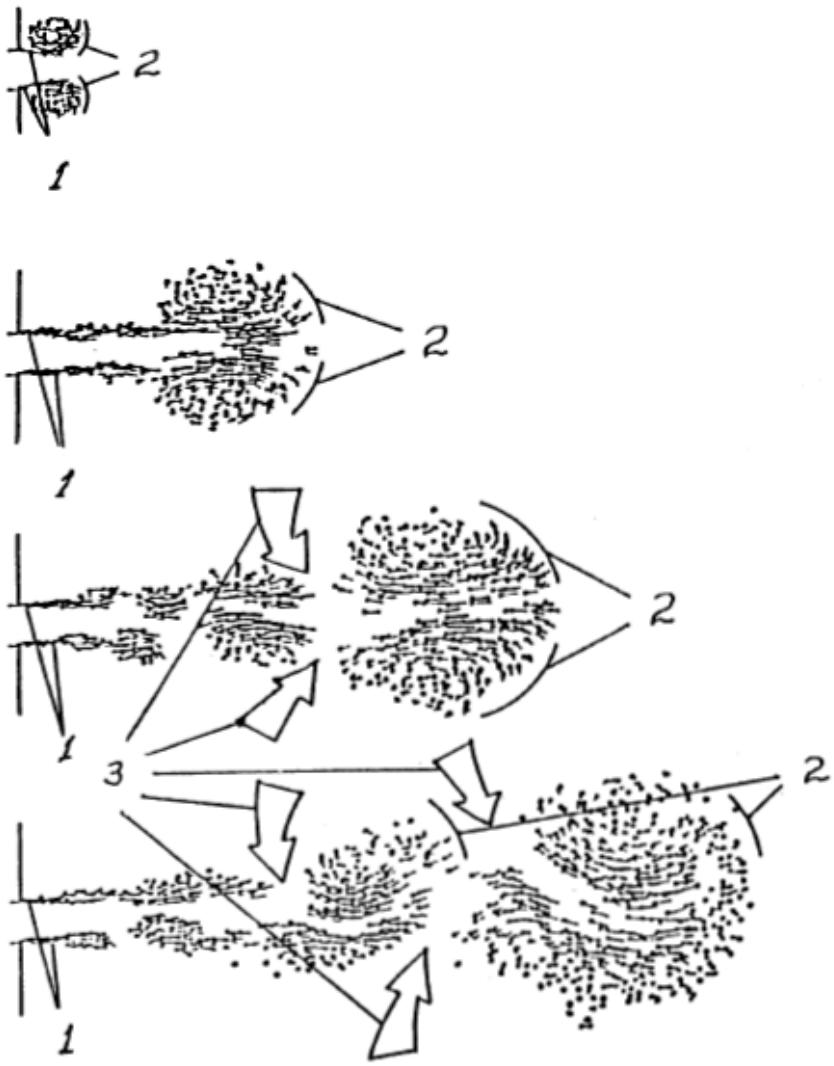

Figure 5.61. Formation and Structure of a Turbulent Jet Plume. 1-zones of intense shear with stretch and extinction; 2-cores of large scale vortices, 3-pathways of entrainment. [107].

6. CONCLUSIONS AND RECOMMENDATIONS

This chapter includes the concluded remarks from this numerical study and recommendations for future work.

6.1 Conclusions

A detailed 3D model of hot-jet ignition constant-volume combustor (CVC) rig established at the Combustion and Propulsion Research Laboratory at the Indiana University-Purdue University Indianapolis (IUPUI) is developed. Numerical investigation of ignition and combustion for the compressible, transient, turbulent, chemically reactive flow for the ignition rig is carried out. Two methane-hydrogen fuel blends are considered for the study, 30:70 (Fuel-A) and 50:50 (Fuel-B). Effects of pre-chamber pressure, CVC chamber initial temperature and jet traverse speed on ignition and combustion is numerically studied. Innovative post-processing techniques are used to study the underlying conditions on ignition. Also to understand the effects of active radicals on chemical kinetics a 2D numerical study is completed.

Active radicals are generated in pre-chamber from the partial or complete combustion of slightly rich pre-chamber fuel. The concentrations of active radicals in the jet is not easily estimated, as the jet issues immediately following combustion when the level of chemical activity is high. For simplicity, the radical species concentrations are estimated but their quantities are included in hot jet from the constant volume equilibrium calculation of the pre-chamber fuel. Inclusion of active radicals in hot jet increase the chemical kinetic rates and decrease ignition delay when compared with only stable species in pre-chamber hot jet. A jet with active radical species is compared with jets with inert species but same thermal energy for all the jets. The active radical jet starts the ignition earlier than the inert hot jets. This indicates

that the active radicals advance the start of chain initiating reactions which in terms create more active radicals. The different jets have same thermal energy but the jet containing active radicals participated in chemical bond breaking reactions to start ignition.

Effects of temperature on chemical ignition delay are studied for six different methane-hydrogen blends from pure methane to pure hydrogen. Chemical ignition delay decreases with temperature for all the fuel blends. Three different equivalence ratios are considered from very lean (0.6) to stoichiometric (1.0). Equivalence ratio shows minimal effect on ignition delay. For a particular fuel blend at a definite temperature chemical ignition delay is almost identical for all the equivalence ratios. Pure hydrogen has the lowest and pure methane has the highest delay. Chemical ignition delay decrease gradually as hydrogen is added with methane. As a result, Fuel-A has lower chemical ignition delay compared to Fuel-B because Fuel-A contains more hydrogen. It should be mentioned that below 800 K all the fuels have practically infinite chemical ignition delay.

For slightly rich pure hydrogen in pre-chamber and 60:40 methane-hydrogen blend in CVC chamber both SAGE and G-equation combustion model show almost identical trends when compared by integrated heat release and flame propagation. Flame propagation in this ignition rig is different than freely propagating flame. Flame propagates with gas motion which is dependent to pressure difference of pre-chamber and CVC chamber.

For slightly rich pure hydrogen in pre-chamber and 50:50 methane-hydrogen blend in CVC chamber both reaction mechanisms (GRI30 and DRM19) for methane show almost identical trend when compared by integrated heat release and several species produced during combustion but DRM19 predicts the ignition around 0.2 ms earlier compared to GRI30. For a case where ignition was very slow to the point that there was no significant combustion, both models have almost matching integrated heat and heat release rate trends and delays with DRM19 slightly over predicting the integrated heat release. This is a good indication that DRM19 is adequate even for situations

where good accuracy is needed to predict even without significant and sustained heat release.

For centered stationary jet, higher pre-chamber pressure has positive effects on ignition delay for Fuel-A. For Fuel-B opposite effect is observed. For 6 bar pre-chamber pressure Fuel-A has the lowest ignition delay at around 0.7 ms. For Fuel-B 6 bar and 4 bar pre-chamber pressure cases do not ignite during the simulation time. Therefore, it can be said that higher turbulent mixing decreases the ignition delay for comparably high reactive fuel blend. For highly reactive fuel, the chemical delay time is short, and the limiting process is the physical mixing time. Thus turbulence reduces the physical mixing time, and thus the overall ignition delay. For less reactive fuel, the chemical delay is long, and small differences in physical delay time are not significant. In terms of Da, it can be said that for more reactive fuel (Fuel-A), jet with higher pressure and speed gives quicker ignition, as Da is large enough to sustain ignition kernel. For Fuel-B, jet with lowest pressure and speed is better to ensure ignition because Da is not too small to cause ignition failure.

Ignition is a three dimensional phenomena. It is possible that, at a certain cell, favorable conditions are available to start a flame kernel but if cells adjacent to the flame kernel are unable to provide favorable conditions that kernel will eventually dissipate. At higher pre-chamber pressure, due to higher mixing Fuel-B may face unfavorable condition to grow flame kernel because of relatively low reactivity than fuel-A. As a result, mixing helps fuel-A to ignite. To support this idea, it is observed that for 2 bar pre-chamber pressure, the variable 'Ignition' sustains a longer amount of time (Figure 5.46) compared to higher pre-chamber pressure cases (Figures 5.45 and 5.44). As a result, Fuel-B gets sufficient time to grow flame kernel with favorable condition.

For centered stationary jet with 6 and 4 bar pre-chamber pressures, the maximum flame surface area is observed about 30 times bigger than the channel cross sectional area. This higher flame surface area is one of the major advantages of very fast deflagration type combustion over detonation type combustion. HRR and vorticity

generated over flame surface is highly influenced by the SFI. For 6 and 4 bar pre-chamber pressures, sudden rise of HRR is observed after second SFI (FAST-SLOW). Sudden rise of deposited vorticity generated on flame surface is observed after both SFI. 2 bar pre-chamber pressure has minimal SFI effect on HRR and vorticity generation.

Higher CVC chamber temperature increase the chemical kinetics which decrease the ignition delay and creates stronger combustion for both fuels.

For Fuel-A and 6 bar pre-chamber pressure, with the increase of nozzle traverse speed ignition delay decrease. 4 bar pre-chamber pressure cases has minimal effects on ignition delay with variable traverse speed. For 2 bar pre-chamber pressure, higher traverse speed cases fail to ignite which implies that lower pre-chamber pressure may not be applicable to practical wave rotor combustor.

Pre-chamber pressure controls the jet penetration and mixing process for a specific nozzle geometry. For a fixed pre-chamber and CVC chamber fuel it is observed that there is an optimum value for penetration and mixing. If the value is too high it could extinct the flame kernel (6 bar pre-chamber pressure). Also if the value is too low it could results to unfavorable conditions for ignition for rotating pre-chamber (2 bar pre-chamber pressure). There is an optimum condition (4 bar pre-chamber pressure) which creates most favorable condition for ignition for both stationary and rotating pre-chamber.

Ignition is found to be strongly related to pre-chamber products mass fraction, CVC chamber products mass fraction and temperature. For a specific fuel a certain range of these variables are found for which ignition occurs for different fluid dynamic conditions. But this is strongly dependent on fuel reactivity and stronger correlation is observed for more reactive fuel.

6.2 Recommendations

The following section discusses the improvements possibilities that can be made to the simulation setup in terms of improving initial conditions and more realistic assumptions that was realized while conducting this current study.

1) Pre-chamber temperature and species are calculated from constant volume equilibrium calculation. In experiments, the combustion in pre-chamber may not reach equilibrium and there is high probability of incomplete combustion. There are two uncertainties related to that from equilibrium calculation. Over-predicting the temperature and under-predicting the active radicals of the hot jet. The ideal solution will be to start the simulation from the pre-chamber spark ignition. But each milliseconds of simulation require almost one day and to reach 6 bar pressure in pre-chamber it would take almost 15 ms. Therefore, at current state this simulation is very expensive. As a result, a simple analytical model for flame propagation which will help to better predict the temperature is recommended.

2) Leak gap between the nozzle and CVC chamber is neglected for this study. But practical wave rotor combustor with hot-jet ignition always maintain a leak gap between the nozzle and combustor. Also leak gap may not have significant effect on ignition but combustion may get affected by the leak gap. Including leak gap in the simulation setup may help to predict more realistic outcomes. But the leak gap distance should be validated from the experiments.

3) RNG k-ε turbulence model is used throughout this study. But it is well known that RNG k-ε model over-predicts the round jet spread. k-ω turbulence models are better suited for round jet study and not available in CFD solver CONVERGE.

4) Small scale vortices play very important role in mixing and entrainment of unburned fuel. RANS simulations are not able to capture the small scale vortices. DNS is still out of reach. LES with 0.0625 mm cut off mesh size may provide valuable information about ignition and still stay within acceptable cpu time.

5) A probability model to predict ignition which will include the statistical variation of input parameters (equivalence ratio, fuel composition etc.) can be developed using the software Cantera with well stirred reactor assumption. But this model should be validated rigorously before further implementation.

LIST OF REFERENCES

LIST OF REFERENCES

[1] William P Attard, Elisa Toulson, Andrew Huisjen, Xuefei Chen, Guoming Zhu, and Harold Schock. Spark ignition and pre-chamber turbulent jet ignition combustion visualization. Technical report, SAE Technical Paper, 2012.

[2] Manikanda Rajagopal, Md Nazmuzzaman Khan, and Razi Nalim. Simulation of hot-jet ignition in a heated constant-volume combustor using adadptive mesh refinement and multi-zone reaction. 50th AIAA/ASME/SAE/ASEE Joint Propulsion Conference, 2014.

[3] R Sadanandan, D Markus, R Schießl, Ulrik Maas, Jimmy Olofsson, Hans Seyfried, Mattias Richter, and Marcus Aldén. Detailed investigation of ignition by hot gas jets. *Proceedings of the Combustion Institute*, 31(1):719–726, 2007.

[4] JW Meyer, PA Urtiew, and AK Oppenheim. On the inadequacy of gasdynamic processes for triggering the transition to detonation. *Combustion and Flame*, 14(1):13–20, 1970.

[5] H Phillips. Ignition in a transient turbulent jet of hot inert gas. *Combustion and Flame*, 19(2):187–195, 1972.

[6] Øystein Larsen and Rolf K Eckhoff. Critical dimensions of holes and slots for transmission of gas explosions: Some preliminary results for propane/air and cylindrical holes. *Journal of Loss Prevention in the Process Industries*, 13(3):341–347, 2000.

[7] Michael Bunce, Hugh Blaxill, Waruna Kulatilaka, and Naibo Jiang. The effects of turbulent jet characteristics on engine performance using a pre-chamber combustor. Technical report, SAE Technical Paper, 2014.

[8] Elisa Toulson, Harold J Schock, and William P Attard. A review of pre-chamber initiated jet ignition combustion systems. Technical report, SAE Technical Paper, 2010.

[9] William P Attard and Hugh Blaxill. A gasoline fueled pre-chamber jet ignition combustion system at unthrottled conditions. Technical report, SAE Technical Paper, 2012.

[10] AA Boretti, MJ Brear, and HC Watson. Experimental and numerical study of a hydrogen fuelled ic engine fitted with the hydrogen assisted jet ignition system. In *16th Australasian Fluid Mechanics Conference (AFMC)*, pages 1142–1147. School of Engineering, The University of Queensland, 2007.

[11] K Kailasanath. Recent developments in the research on pulse detonation engines. *AIAA journal*, 41(2):145–159, 2003.

[12] DH Lieberman, KL Parkin, and JE Shepherd. Detonation initiation by a hot turbulent jet for use in pulse detonation engines. In *38th Joint Propulsion Conference, Indianapolis, IN, July*, pages 7–10, 2002.

[13] Pezhman Akbari and Razi Nalim. Review of recent developments in wave rotor combustion technology. *Journal of Propulsion and Power*, 25(4):833–844, 2009.

[14] S. D. Wijeyakulasuriya. Transient and translating gas jet modeling for pressure gain combustion applications. *Doctor of Philosophy, Purdue University, West Lafayette, Indiana*, 2011.

[15] Kerem Pekkan and M Razi Nalim. Control of fuel and hot-gas leakage in a stratified internal combustion wave rotor. *38th AIAA/ASME/SAE/ASEE Joint Propulsion Conference Exhibit*, 4067, 2002.

[16] Daniel W Paxson. A general numerical model for wave rotor analysis. 1992.

[17] M Razi Nalim and Daniel E Paxson. A numerical investigation of premixed combustion in wave rotors. *Journal of engineering for gas turbines and power*, 119(3):668–675, 1997.

[18] M Razi Nalim and Zuhair A Izzy. Simulation of a wave rotor pulse detonation engine with integrated ejector. In *ISOABE, ISABE- International Symposium on Air Breathing Engines, 15 th, Bangalore, India*, 2001.

[19] Razi Nalim and Kerem Pekkan. Two-dimensional flow and nox emissions in deflagrative internal combustion wave rotor configurations. In *ASME Turbo Expo 2002: Power for Land, Sea, and Air*, pages 501–511. American Society of Mechanical Engineers, 2002.

[20] Pezhman Akbari, Berrak Alparslan, Viktor Kilchyk, and Razi Nalim. Numerical analysis of hydrogen-fueled wave rotors for gas turbine applications. In *First International Hydrogen Energy Congress, Istanbul, Turkey*, 2005.

[21] SA Khalid, A Banerjee, Pezhman Akbari, and MR Nalim. Two-dimensional numerical modeling of mixture inflow in a combustion wave rotor. *4th IECEC, AIAA Paper*, 4125, 2006.

[22] Pezhman Akbari and MR Nalim. Analysis of flow processes in detonative wave rotors and pulse detonation engines. *AIAA Paper*, 1236:2006, 2006.

[23] Pezhman Akbari, MR Nalim, and PH Snyder. Numerical simulation and design of a combustion wave rotor for deflagrative and detonative propagation. In *Proceedings of the 42nd AIAA/ASME/SAE/ASEE Joint Propulsion Conference and Exhibit*, 2006.

[24] Viktor Kilchyk, Charles Merkle, and Razi Nalim. Effect of channel rotation on premixed turbulent combustion in a wave rotor combustor. *combustion*, 3:8, 2007.

[25] Sameera D Wijeyakulasuriya and M Razi Nalim. Transient translating gas jets in confined channels. In *45th AIAA/ASME/SAE/ASEE Joint Propulsion Conference & Exhibit*, 2009.

[26] Sameera D Wijeyakulasuriya, Indika U Perera, and M Razi Nalim. Mixing and ignition potential of a transient confined turbulent jet in a wave rotor constant-volume combustor. In *46 th AIAA/ASME/SAE/ASEE Joint Propulsion Conference and Exhibit*, 2010.

[27] Pezhman Akbari, Razi Nalim, and Norbert Mueller. A review of wave rotor technology and its applications. *Journal of Engineering for Gas Turbines and Power*, 128(4):717–735, 2006.

[28] UI Perera, SD Wijeyakulasuriya, and MR Nalim. Hot jet ignition delay time and localization analysis for ethylene-air. In *49th AIAA Aerospace Sciences Meeting*, 2011.

[29] UI Perera, Sameera D Wijeyakulasuriya, and M Razi Nalim. Hot combustion torch jet ignition delay time for ethylene-air mixtures. In *49th Aerospace Sciences Meeting, Orlando, FL, January*, pages 4–7, 2011.

[30] Sameera D Wijeyakulasuriya, Manikanda Rajagopal, and Razi Nalim. Shock-flame interaction modeling in a constant-volume combustion channel using detailed chemical kinetics and automatic mesh refinement. In *ASME Turbo Expo 2013: Turbine Technical Conference and Exposition*. American Society of Mechanical Engineers, 2013.

[31] M. Bilgin. Stationary and rotating hot jet ignition and flame propagation in a premixed cell. *Ph.D. Dissertation,Aeronautics and Astronautics Dept, University of Washington,Seattle, WA*, 1998.

[32] D. Baronia. Numerical analysis of hot jet injection and premixed flame propagation in a channel. *MS Thesis, Mechanical Engineering, Purdue University,Indianapolis, Indiana*, 2006.

[33] I.U. Perera. Experimental investigation into combustion torch jet ignition of methane-air, ethylene-air, and propane-air mixtures. *MS Thesis, Mechanical Engineering, Purdue University,Indianapolis, Indiana*, 2010.

[34] Abdullah Karimi, Prasanna Chinnathambi, Manikanda Rajagopal, and Razi Nalim. Hot-jet ignition of hydrocarbons and hydrogen in air: Effect of jet chemical activity. 49th AIAA/ASME/SAE/ASEE Joint Propulsion Conference,, 2013.

[35] K. Murphy. Experimental investigation of traversing hot-jet ignition of ethylene, and propane-air mixtures in a constant-volume combustor. *Paper, Mechanical Engineering, IUPUI,Indianapolis, Indiana*, unpublished.

[36] P. Chinnathambi. Experimental investigation on traversing hot jet ignition of lean hydrocarbon-air mixtures in a constant volume combustor. *MS Thesis, Mechanical Engineering, Purdue University,Indianapolis, Indiana*, 2013.

[37] LA Gussak, VP Karpov, and Yu V Tikhonov. The application of lag-process in prechamber engines. Technical report, SAE Technical Paper, 1979.

[38] Tasuku Date, Shizuo Yagi, Akira Ishizuya, and Isao Fujii. Research and development of the honda cvcc engine. Technical report, SAE Technical Paper, 1974.

[39] S Yagi, T Dath, H Ukawa, and I Fujii. Research and development of honda cvcc engine. In *Paper C13/75 presented at IMechE Conference*, 1976.

[40] Tim G Adams. Torch ignition for combustion control of lean mixtures. Technical report, SAE Technical Paper, 1979.

[41] Walter Brandstetter. The volkswagen lean burn pc-engine concept. Technical report, SAE Technical Paper, 1980.

[42] T Ken Garrett. Porsche stratified charge engine. *Environmental Science & Technology*, 9(9):826–830, 1975.

[43] FA Wyczalek, JL Harned, S Maksymiuk, and JR Blevins. Efi prechamber torch ignition of lean mixtures. Technical report, SAE Technical Paper, 1975.

[44] Sy A Ali and William P Parks. Renewable fuels turbine project. In *ASME 1998 International Gas Turbine and Aeroengine Congress and Exhibition*. American Society of Mechanical Engineers, 1998.

[45] Oanh Nguyen and Scott Samuelsen. The effect of discrete pilot hydrogen dopant injection on the lean blowout performance of a model gas turbine combustor. *ASME Paper*, (99-GT):359, 1999.

[46] Robert W Schefer, DM Wicksall, and AK Agrawal. Combustion of hydrogen-enriched methane in a lean premixed swirl-stabilized burner. *Proceedings of the combustion institute*, 29(1):843–851, 2002.

[47] SO Bade Shrestha and GA Karim. Hydrogen as an additive to methane for spark ignition engine applications. *International Journal of Hydrogen Energy*, 24(6):577–586, 1999.

[48] Roger Sierens and Evert Rosseel. Variable composition hydrogen/natural gas mixtures for increased engine efficiency and decreased emissions. *Journal of engineering for gas turbines and power*, 122(1):135–140, 2000.

[49] CG Bauer and TW Forest. Effect of hydrogen addition on the performance of methane-fueled vehicles. part i: effect on si engine performance. *International Journal of Hydrogen Energy*, 26(1):55–70, 2001.

[50] RK Cheng and AK Oppenheim. Autoignition in methane+hydrogen mixtures. *Combustion and Flame*, 58(2):125–139, 1984.

[51] Evatt R Hawkes and Jacqueline H Chen. Direct numerical simulation of hydrogen-enriched lean premixed methane–air flames. *Combustion and Flame*, 138(3):242–258, 2004.

[52] Erjiang Hu, Zuohua Huang, Jiajia He, Chun Jin, and Jianjun Zheng. Experimental and numerical study on laminar burning characteristics of premixed methane–hydrogen–air flames. *international journal of hydrogen energy*, 34(11):4876–4888, 2009.

[53] Ekenechukwu C Okafor, Akihiro Hayakawa, Yukihide Nagano, and Toshiaki Kitagawa. Effects of hydrogen concentration on premixed laminar flames of hydrogen–methane–air. *international journal of hydrogen energy*, 39(5):2409–2417, 2014.

[54] Yiguang Ju and Takashi Niioka. Ignition simulation of methane/hydrogen mixtures in a supersonic mixing layer. *Combustion and flame*, 102(4):462–470, 1995.

[55] Jinhua Wang, Zuohua Huang, Chenglong Tang, Haiyan Miao, and Xibin Wang. Numerical study of the effect of hydrogen addition on methane–air mixtures combustion. *international journal of hydrogen energy*, 34(2):1084–1096, 2009.

[56] S. Biswas and L Qiao. Ignition of premixed ch_4/air and h_2/air mixtures by a hot jet generated by prechamber combustion. In *9th U. S. National Combustion Meeting*. Central States Section of the Combustion Institute, 2015.

[57] PK Senecal, E Pomraning, KJ Richards, TE Briggs, CY Choi, RM McDavid, and MA Patterson. Multi-dimensional modeling of direct-injection diesel spray liquid length and flame lift-off length using cfd and parallel detailed chemistry. Technical report, SAE Technical Paper, 2003.

[58] Robert J Kee, Fran M Rupley, and James A Miller. Chemkin-ii: A fortran chemical kinetics package for the analysis of gas-phase chemical kinetics. Technical report, Sandia National Labs., Livermore, CA (USA), 1989.

[59] Eric Pomraning, Keith Richards, and PK Senecal. Modeling turbulent combustion using a rans model, detailed chemistry, and adaptive mesh refinement. Technical report, SAE Technical Paper, 2014.

[60] Bjørn F Magnussen and Bjørn H Hjertager. On mathematical modeling of turbulent combustion with special emphasis on soot formation and combustion. In *Symposium (International) on Combustion*, volume 16, pages 719–729. Elsevier, 1977.

[61] Rodney O Fox and Herbert L.. Stiles. *Computational models for turbulent reacting flows*, volume 419. Cambridge university press Cambridge, 2003.

[62] J Janicka, W Kolbe, and W Kollmann. Closure of the transport equation for the probability density funcfion of turbulent scalar fields. *Journal of Non-Equilibrium Thermodynamics*, 4(1):47–66, 1979.

[63] SB Pope. Pdf methods for turbulent reactive flows. *Progress in Energy and Combustion Science*, 11(2):119–192, 1985.

[64] ALAN R KERSTEIN. A linear-eddy model of turbulent scalar transport and mixing. *Combustion Science and Technology*, 60(4-6):391–421, 1988.

[65] AT Norris. Algebraic turbulence-chemistry interaction model. In *50th AIAA Aerospace Sciences Meeting including the New Horizons Forum and Aerospace Exposition*, page 183.

[66] A. Karimi. Numerical study of hot jet ignition of hydrocarbon-air mixtures in a constant-volume combustor. *MS Thesis, Mechanical Engineering, Purdue University,Indianapolis, Indiana*, 2014.

[67] Abdullah Karimi, Manikanda Rajagopal, and Razi Nalim. Traversing hot-jet ignition in a constant-volume combustor. ASME Turbo Expo: Turbine Technical Conference and Exposition, Volume 1B: Combustion, Fuels and Emissions,, 2013.

[68] Raad I Issa. Solution of the implicitly discretised fluid flow equations by operator-splitting. *Journal of computational physics*, 62(1):40–65, 1986.

[69] K. J. Richards, P.K. Senecal, and E. Pomraning. Converge^{TM} (version 2.2) manual. *Convergent Science, Inc., Middleton, WI.*, 2014.

[70] Salvador M Aceves, Daniel L Flowers, Charles K Westbrook, J Ray Smith, William Pitz, Robert Dibble, Magnus Christensen, and Bengt Johansson. A multi-zone model for prediction of hcci combustion and emissions. Technical report, SAE Technical paper, 2000.

[71] A Babajimopoulos, DN Assanis, DL Flowers, SM Aceves, and RP Hessel. A fully coupled computational fluid dynamics and multi-zone model with detailed chemical kinetics for the simulation of premixed charge compression ignition engines. *International journal of engine research*, 6(5):497–512, 2005.

[72] D. Goodwin. Cantera: An object-oriented software toolkit for chemical kinetics, thermodynamics, and transport processes, caltech, pasadena. *Available:http://code.google.com/p/cantera*, 2009.

[73] D. M. Smith, G. P.and Golden, M. Frenklach, N.W. Moriarty, B. Eiteneer, M. Goldenberg, T.C. Bowman, R.K. Hanson, S Song, W.C¿ Gardiner Jr., V.V Lissianski, and Zhiwei. Gri mech-3.0. *http://www.me.berkeley.edu/gri_mech/*.

[74] Thierry Poinsot and Denis Veynante. Theoretical and numerical combustion. 2005.

[75] Richard H Pletcher, John C Tannehill, and Dale Anderson. *Computational fluid mechanics and heat transfer*. CRC Press, 2012.

[76] William A Sirignano. Volume averaging for the analysis of turbulent spray flows. *International journal of multiphase flow*, 31(6):675–705, 2005.

[77] P Boudier, S Henriot, T Poinsot, and T Baritaud. A model for turbulent flame ignition and propagation in spark ignition engines. In *Symposium (International) on Combustion*, volume 24, pages 503–510. Elsevier, 1992.

[78] RS Cant and KNC Bray. Strained laminar flamelet calculations of premixed turbulent combustion in a closed vessel. In *Symposium (International) on Combustion*, volume 22, pages 791–799. Elsevier, 1989.

[79] S Som, PK Senecal, and E Pomraning. Comparison of rans and les turbulence models against constant volume diesel experiments. In *24th Annual Conference on Liquid Atomization and Spray Systems, ILASS Americas, San Antonio, TX*, 2012.

[80] S Som and SK Aggarwal. Effects of primary breakup modeling on spray and combustion characteristics of compression ignition engines. *Combustion and Flame*, 157(6):1179–1193, 2010.

[81] Song-Charng Kong, Yong Sun, and Rolf D Rietz. Modeling diesel spray flame liftoff, sooting tendency, and nox emissions using detailed chemistry with phenomenological soot model. *Journal of Engineering for Gas Turbines and Power*, 129(1):245–251, 2007.

[82] T Lucchini, G dErrico, D Ettorre, and G Ferrari. Numerical investigation of non-reacting and reacting diesel sprays in constant-volume vessels. Technical report, SAE Technical Paper, 2009.

[83] Jeffrey Naber and Dennis L Siebers. Effects of gas density and vaporization on penetration and dispersion of diesel sprays. Technical report, SAE technical paper, 1996.

[84] Brian Higgins and Dennis L Siebers. Measurement of the flame lift-off location on di diesel sprays using oh chemiluminescence. Technical report, SAE Technical Paper, 2001.

[85] BE Launder and DB Spalding. Mathematical model of turbulence. *Acadamic, London*, 1972.

[86] VSASTBCG Yakhot, SA Orszag, S Thangam, TB Gatski, and CG Speziale. Development of turbulence models for shear flows by a double expansion technique. *Physics of Fluids A: Fluid Dynamics (1989-1993)*, 4(7):1510–1520, 1992.

[87] Zhiyu Han and Rolf D Reitz. Turbulence modeling of internal combustion engines using rng κ-ε models. *Combustion science and technology*, 106(4-6):267–295, 1995.

[88] SH El Tahry and DC Haworth. Directions in turbulence modeling for in-cylinder flows in reciprocating engines. *Journal of Propulsion and Power*, 8(5):1040–1048, 1992.

[89] Victor Yakhot and Steven A Orszag. Renormalization group analysis of turbulence. i. basic theory. *Journal of scientific computing*, 1(1):3–51, 1986.

[90] Charles G Speziale, Thomas B Gatski, and Nessan Fitzmaurice. An analysis of rng-based turbulence models for homogeneous shear flow. *Physics of Fluids A: Fluid Dynamics (1989-1993)*, 3(9):2278–2281, 1991.

[91] PK Senecal, KJ Richards, E Pomraning, T Yang, MZ Dai, RM McDavid, MA Patterson, S Hou, and T Shethaji. A new parallel cut-cell cartesian cfd code for rapid grid generation applied to in-cylinder diesel engine simulations. Technical report, SAE Technical Paper, 2007.

[92] Sameera D Wijeyakulasuriya and Saurav Mitra. Analyzing three-dimensional multiple shock-flame interactions in a constant-volume combustion channel. *Combustion Science and Technology*, 186(12):1907–1927, 2014.

[93] FA Williams. Turbulent combustion. *The mathematics of combustion*, 2:267–294, 1985.

[94] Norbert Peters. *Turbulent combustion*. Cambridge university press, 2000.

[95] D. M. Smith, G. P.and Golden, M. Frenklach, N.W. Moriarty, B. Eiteneer, M. Goldenberg, T.C. Bowman, R.K. Hanson, S Song, W.C Gardiner Jr., and V.V Lissianski. Reduced reaction sets based on gri-mech 1.2. *http://combustion.berkeley.edu/drm/drm19.dat*.

[96] GP Smith, DM Golden, M Frenklach, NW Moriarty, B Eiteneer, M Goldenberg, CT Bowman, RK Hanson, S Song, WC Gardiner, et al. Gri-mechan optimized detailed chemical reaction mechanism for methane combustion. Technical report, Technical Report http://www. me. berkeley. edu/gri mech, Gas Research Institute, 1999.

[97] A Kazakov and M. Frenklach. Numerical performance of drm19 and drm22. *http://combustion.berkeley.edu/drm/*, Last accessed June 2015.

[98] EL Petersen, DF Davidson, and RK Hanson. Kinetics modeling of shock-induced ignition in low-dilution ch 4/o 2 mixtures at high pressures and intermediate temperatures. *Combustion and Flame*, 117(1):272–290, 1999.

[99] KJ Hughes, T Turanyi, AR Clague, and MJ Pilling. Development and testing of a comprehensive chemical mechanism for the oxidation of methane. *International Journal of Chemical Kinetics*, 33(9):513–538, 2001.

[100] Tianfeng Lu and Chung K Law. Toward accommodating realistic fuel chemistry in large-scale computations. *Progress in Energy and Combustion Science*, 35(2):192–215, 2009.

[101] Yingjia Zhang, Xue Jiang, Liangjie Wei, Jiaxiang Zhang, Chenglong Tang, and Zuohua Huang. Experimental and modeling study on auto-ignition characteristics of methane/hydrogen blends under engine relevant pressure. *international journal of hydrogen energy*, 37(24):19168–19176, 2012.

[102] Stephen R Turns et al. *An introduction to combustion*, volume 287. McGraw-hill New York, 1996.

[103] Sanford Gordon and Bonnie J McBride. *Computer program for calculation of complex chemical equilibrium compositions and applications*. National Aeronautics and Space Administration, Office of Management, Scientific and Technical Information Program, 1996.

[104] Michael L Norman and K-HA Winkler. Supersonic jets. *Los Alamos: Los Alamos National Laboratory*, 1, 1985.

[105] J.A. Scott. Shock diamonds and mach disks. *http://www.aerospaceweb.org/question/propulsion/q0224.shtml*, Last accessed April 2015.

[106] N. w. shock diamonds forming in NASA's methane engine built by XCOR Aerospace. Methane blast. *http://science.nasa.gov/science-news/science-at-nasa/2007/04may_methaneblast/*, Last accessed April 2015.

[107] JA Maxson, DM Hensinger, K Hom, and AK Oppenheim. Performance of multiple stream pulsed jet combustion systems. Technical report, SAE Technical Paper, 1991.

[108] V Kilchyk, R Nalim, and C Merkle. Baroclinic vortex sheet production by shocks and expansion waves. *Shock Waves*, 20(5):367–380, 2010.

[109] CEI Software. Ensight from computational engineering international. *www.ceisoftware.com.*, 2013.

[110] V Kilchyk, R Nalim, and C Merkle. Laminar premixed flame fuel consumption rate modulation by shocks and expansion waves. *Combustion and Flame*, 158(6):1140–1148, 2011.

[111] DF Davidson and RK Hanson. Interpreting shock tube ignition data. *International journal of chemical kinetics*, 36(9):510–523, 2004.

[112] SB Pope. Turbulent premixed flames. *Annual review of fluid mechanics*, 19(1):237–270, 1987.

[113] Francesco Bonelli, Annarita Viggiano, and Vinicio Magi. A numerical analysis of hydrogen underexpanded jets under real gas assumption. *Journal of Fluids Engineering*, 135(12):121101, 2013.

APPENDICES

A. SCRIPT FILE TO RUN CONVERGE ON BIG RED 2

```
#!/bin/bash
#PBS -l nodes=4:ppn=32
#PBS -l walltime=36:00:00
#PBS -N my_job
#PBS -q cpu
#PBS -V
PROJ_LOC=\$PBS_O_WORKDIR
export CMD=/N/soft/rhel6/converge/converge-2.1.0_121214/l_x86_64
/bin/converge
cd \$PROJ_LOC
export RLM_DEBUG=csci
export RLM_LICENSE=2765@134.68.7.130
aprun -n 128 \$CMD super   >logfile.cvglog
```

B. MATLAB CODE TO CALCULATE CHEMICAL IGNITION DELAY

```
function ignite_hp(gas)
help ignite_hp
if nargin == 0 | ~isa(gas,'GasMix')
   gas = IdealGasMix('gri30.xml');
end
mw = molecularWeights(gas);
nsp = nSpecies(gas);
set(gas,'T',900.0,'P',oneatm,'X','H2:4,O2:.833,N2:3.13');
y0 = [temperature(gas)
      massFractions(gas)];
tel = [0 1];
options = odeset('RelTol',1.e-5,'AbsTol',1.e-12,'Stats','on');
t0 = cputime;
out = ode15s(@conhp,tel,y0,options,gas,mw);
disp(['CPU time = ' num2str(cputime - t0)]);
if nargout == 0
   % plot the temperature and OH mole fractions.
   figure(1);
   plot(out.x,out.y(1,:));
   xlabel('time');
   ylabel('Temperature');
   title(['Final T = ' num2str(out.y(1,end)) ' K']);

   figure(2);
   ioh = speciesIndex(gas,'OH');
```

```
    plot(out.x,out.y(1+ioh,:));
    xlabel('time');
    ylabel('Mass Fraction');
    title('OH Mass Fraction');
end
```

C. EQUATIONS USED TO CALCULATE THERMALLY MATCHED INERT HOT-JET

Temperature of reactive species is 2670 K which is calculated from equilibrium calculation for Methane-air combustion. Equation C.1 is mass balance equation. Equation C.2 and C.2.1 is density balance equation. Right hand side of Equation C.2.1 is calculated using the reactive species mass fraction from equilibrium calculation. Equation C., C.3.1 and C.3.2 is enthalpy balance equations. Equation C.3.1 is showing how enthalpy is calculated for each species at higher temperature. Right hand side of Equation C.3.2 is calculated using the reactive species mass fraction from equilibrium calculation. Equation C.4, C.4.1 and C.4.2 is internal energy balance equations. Equation C.4.1 is showing how internal energy is calculated for each species at higher temperature. Right hand side of Equation C.4.2 is calculated using the reactive species mass fraction from equilibrium calculation. By solving Equation C.1, C.2.1 and C.3.2 simultaneously, mass fractions of inert species for Case 4.2 is calculated. By solving Equation C.1, C.2.1 and C.4.2 simultaneously, mass fractions of inert species for Case 4.3 is calculated.

$$Y_{Ar} + Y_{He} + Y_{N_2} = 1 \tag{C.1}$$

$$\sum (Density)_{inertspecies} = \sum (Density)_{reactivespecies} \tag{C.2}$$

$$39.95Y_{Ar} + 4.002Y_{He} + 28Y_{N_2} = 28.514 \tag{C.2.1}$$

$$\sum (Enthalpy)_{inertspecies} = \sum (Enthalpy)_{reactivespecies} \tag{C.3}$$

$$H(2670K) = \int_{300}^{2670} c_p dT + H(300K) \tag{C.3.1}$$

$$1234.05Y_{Ar} + 12326.5Y_{He} + 2875.4Y_{N_2} = 3361.7 \tag{C.3.2}$$

$$\sum (InternalEnergy)_{inertspecies} = \sum (InternalEnergy)_{reactivespecies} \tag{C.4}$$

$$U(2670K) = \int_{300}^{2670} c_v dT + U(300K) \tag{C.4.1}$$

$$746.42Y_{Ar} + 7396.29Y_{He} + 2171.05Y_{N_2} = 2618.84 \tag{C.4.2}$$